Modélisation numérique de la dynamique des fluides du procédé de dégivrage au sol des aéronefs par liquide de dégivrage

par

Sami ERNEZ

THÈSE PAR ARTICLES PRÉSENTÉE À L'ÉCOLE DE TECHNOLOGIE SUPÉRIEURE COMME EXIGENCE PARTIELLEÀ L'OBTENTION DE DU DOCTORAT EN GÉNIE
Ph. D.

MONTRÉAL, LE 7 MARS 2023

ÉCOLE DE TECHNOLOGIE SUPÉRIEURE
UNIVERSITÉ DU QUÉBEC

PRÉSENTATION DU JURY

CETTE THÈSE A ÉTÉ ÉVALUÉE

PAR UN JURY COMPOSÉ DE :

M. François Morency, directeur de thèse
Département de génie mécanique à l'École de technologie supérieure

M. Éric Paquette, président du jury
Département de génie logiciel et des TI à l'École de technologie supérieure

M. Romain Lemaire, membre du jury
Département de génie mécanique à l'École de technologie supérieure

M. Jean-Yves Trépanier, examinateur externe
Département de génie mécanique à Polytechnique Montréal

ELLE A FAIT L'OBJET D'UNE SOUTENANCE DEVANT JURY ET PUBLIC

LE 15 FÉVRIER 2023

À L'ÉCOLE DE TECHNOLOGIE SUPÉRIEURE

REMERCIEMENTS

Je tiens à exprimer ma gratitude au professeur François Morency pour son excellent encadrement tout au long de cette thèse. Il m'a été une grande source d'inspiration à travers son organisation parfaite de notre groupe de recherche, son charisme ainsi que sa méthodologie scientifique. Je lui suis reconnaissant pour toutes ses corrections, commentaires et critiques grâce auxquels j'ai pu acquérir l'expertise dont je suis doté aujourd'hui. J'ai aussi beaucoup apprécié le temps passé ensemble lors des conférences. Cela m'a permis de mieux comprendre l'intérêt de la divulgation scientifique ainsi que sa façon de faire. Enfin, je le remercie pour sa confiance et sa recommandation qui m'ont introduit à l'industrie au Canada.

Je tiens également à remercier le professeur Éric Paquette d'avoir accepté de présider le jury d'évaluation de ma thèse, ainsi que les professeurs Romain Lemaire et Jean-Yves Trépanier d'avoir accepté d'en faire partie.

Je ne saurais finir sans adresser un gros et sincère merci à ma famille et à mon meilleur ami depuis l'enfance M. Rafik Lefi qui sans leur soutien moral et financier ce travail de recherche n'aurait même pas pu commencer. Je dédie ce travail aux trois femmes de ma vie; à ma mère qui a tout sacrifié pour mon éducation, à mon épouse et allié et à ma fille en espérant qu'elle me dépasse un jour.

"We are, after all, the greatest problem solvers to have ever existed on earth."

Sir David Attenborough (2021), COP26 summit: Opening Ceremony

Modélisation numérique de la dynamique des fluides du procédé de dégivrage au sol des aéronefs par liquide de dégivrage

Sami ERNEZ

RÉSUMÉ

Le processus de dégivrage au sol des aéronefs est obligatoire pour le décollage de tout aéronef dans des conditions givrantes. Au début, les avions étaient dégivrés par une opération purement mécanique. Depuis les années 1950, l'industrie s'est tournée vers l'utilisation de solutions de dégivrage. De nos jours, le processus est bien encadré par les normes mondiales internationales d'antigivrage et de dégivrage de la *Society of Automotive Engineers* (SAE). Cependant, plusieurs valeurs de paramètres du processus ne sont pas définies, ce qui rend l'efficacité du processus dépendante du niveau d'expertise de l'opérateur. Cette recherche propose des méthodes numériques permettant l'utilisation de la mécanique des fluides numériques (MFN) pour la simulation du procédé de dégivrage au sol des aéronefs. Ces méthodes numériques ont été implémentées dans un code MFN et ont été vérifiées. Ce travail est présenté sous la forme d'une thèse par article. Les méthodes numériques sont publiées à travers trois articles de journaux et ont servi à concevoir le code MFN. Le premier article présente un modèle eulérien-lagrangien de dégivrage au sol des aéronefs qui évite le problème de dispersion d'échelle causé par la distance considérable entre la buse de pulvérisation et la surface à dégivrer. Les vérifications sont effectuées à l'aide d'un cas test d'un jet de liquide chaud à particules impactant une plaque plane horizontale. La répartition de la chaleur calculée à la paroi est vérifiée. Enfin, une étude de l'angle d'inclinaison du jet est présentée. Le deuxième article se concentre sur la région au voisinage de la glace où il propose une méthode MFN pour simuler l'interaction entre la glace et le liquide de dégivrage chaud. Une approche d'écoulement diphasique particulaire est utilisée pour modéliser l'impact de la pulvérisation sur la glace près de la surface contaminée. La fonte du givre est modélisée à l'aide d'une version étendue de la technique enthalpie-porosité développée durant cette thèse. L'eau résultant du processus de fusion est diffusée dans le liquide de dégivrage formant un film monophasique. Cet article présente un nouveau modèle du processus. Le modèle est vérifié et validé en trois étapes : (i) vérification du transport de l'espèce, (ii) validation du champ de température transitoire d'un mélange, (iii) validation du transfert de chaleur par convection d'un jet incident. Le coefficient de perméabilité de la technique enthalpie-porosité est ensuite calibré. Le modèle proposé s'est avéré être un bon candidat pour une étude paramétrique du processus de dégivrage au sol des aéronefs. Le troisième article est une combinaison des deux premiers. Il présente une méthode MFN pour simuler en trois dimensions le procédé. La méthode comprend un modèle multi-régions où une méthode lagrangienne résout les équations du jet et la technique enthalpie-porosité étendue simule la fonte du givre avec une méthode eulérienne. L'approche multi-région est vérifiée dans cet article par un test de pénétration de la pointe de pulvérisation (STP). La STP prédite par le modèle multi-région concorde à 99 % avec la STP prédit par un modèle lagrangien. Par conséquent, l'approche multi-région transfère correctement la quantité de mouvement des particules entre les deux régions. Les trois articles ont abouti à un code MFN spécialement conçu et vérifié pour simuler le procédé de dégivrage au sol des aéronefs. Des

scénarios de dégivrage optimaux peuvent être définis en étudiant numériquement l'effet des paramètres de pulvérisation sur l'efficacité du dégivrage. Ce code pourrait servir également à concevoir un simulateur pour la formation des agents.

Mots-clés : dégivrage au sol des aéronefs, jet impactant, fusion de givre, MFN, vérification et validation (V&V), modèle eulérien-lagrangien à deux régions, écoulements particulaires diphasiques, technique d'enthalpie-porosité étendue, transfert de chaleur, diffusion des espèces, paramètres de pulvérisation

Computational fluid dynamic modelling of the aircraft ground deicing process with aircraft deicing fluid sprays

Sami ERNEZ

ABSTRACT

The aircraft ground deicing process is mandatory for all types of aircraft to take-off in icing conditions. In the early days aircraft were deiced by a purely mechanical operation. In the 1950s the industry moved toward the use of deicing solutions. Nowadays, the process is well defined by the Society of Automotive Engineers (SAE) international global anti-icing and de-icing standards. However, several process parameter values are not defined which leads the process efficiency to dependent on the operator's level of expertise. This research proposes numerical methods allowing the use of computational fluid dynamics (CFD) for the simulation of the aircraft ground deicing process. These numerical methods have been implemented in a CFD code and have been verified. This work is presented in the form of a thesis by article. The numerical methods are published through three journal articles and served to develop the CFD code. The first paper presents a Eulerian-Lagrangian model of aircraft ground deicing that avoids the scale dispersion problem caused by the considerable distance between the spray nozzle and the surface to be de-iced. Verifications are done using a testcase of a hot particle liquid spray impinging on a horizontal flat plate. The computed wall heat distribution is verified. In the end, an inclination spray angle study is presented. The second paper focuses on the region at the vicinity of the ice where it proposes a CFD method to simulate the interaction between ice and the hot aircraft deicing fluid. A particulate two-phase flow approach is used to model the spray impact on ice near the contaminated surface. Ice melting is modelled using an extended version of the enthalpy-porosity technique. The water resulting from the melting process is diffused into the deicing fluid forming a single-phase film. This paper presents a new model of the process. The model is verified and validated through three steps: (i) verification of the species transport, (ii) validation of the transient temperature field of a mixture, (iii) validation of the convective heat transfer of an impinging spray. The permeability coefficient of the enthalpy-porosity technique is then calibrated. The proposed model proved to be a suitable candidate for a parametric study of the aircraft ground deicing process. The third paper is a combination of the first two where it presents a 3 dimensions CFD method to simulate the process in full scale. The method comprises a multi-region model where a Lagrangian method solves the spray particle equations, and the enthalpy porosity simulates the ice melting with an Eulerian method. The multi-region approach is verified in this paper through a spray-tip penetration (STP) test. The STP predicted by the multi-region model agrees at 99% with the STP predicted by a Lagrangian model. Therefore, the multi-region correctly transfers the particle momentum between the two regions. The three papers led to a CFD code specially designed and verified to simulate the aircraft ground deicing process. Optimal deicing scenarios can be defined by investigating the effect of spray parameters on deicing efficiency. This code could also be used to design a simulator for training agents.

Keywords: aircraft ground deicing, impinging spray, ice melting, CFD, verification and validation (V&V), two-region Eulerian-Lagrangian model, particulate two-phase flows, extended enthalpy-porosity technique, heat transfer, species diffusion, spraying parameters

TABLE DES MATIÈRES

Page

LISTE DES TABLEAUX

Page

LISTE DES FIGURES

LISTE DES ABRÉVIATIONS, SIGLES ET ACRONYMES

ACRP	Airport Cooperative Research Program
ADF	Aircraft Deicing Fluid
AGD	Aircraft Ground Deicing
AGIP	Approved Ground Icing Program
CCME	Canadian Council of Ministers of the Environment
CFD	Computational Fluid Dynamics
CFL	Courant–Friedrichs–Lewy
DIC	Diagonal Incomplete-Cholesky
EDEF	Eulerian-Drop in an Eulerian-Fluid
FAA	Federal Aviation Administration
GAMG	Geometric Algebraic Multi-Grid
ICAO	International Civil Aviation Organization
JANAF	Joint Army-Navy-NASA-Air Force
LDEF	Lagrangian-Drop in an Eulerian-Fluid
LS	Level Set
MFN	Mécanique des Fluides Numériques
RAC	Règlement de l'Aviation Canadien
SAE	Society of Automotive Engineers
SIAGDP	Standardized International Aircraft Ground Deicing Program
STP	Spray Tip Penetration
TC	Transport Canada
OpenFOAM	Open Field Operation and Manipulation
PCM	Phase-Change Material

PDF	Probability Distribution Function
PISO	Pressure Implicit with Splitting of Operator
PR	Particle rate
SIMPLE	Semi-Implicit Method for Pressure-Linked Equations
VOF	Volume-Of-Fluid
V&V	Verification and Validation

LISTE DES SYMBOLES ET UNITÉS DE MESURE

Symboles latins

Symbole	*Description*	*Unités*
A_{wall}	Surface de cellule	m^2
A_s	Paramètre de la loi de Sutherland	$kg/m \cdot s \cdot K$
$a_{0..4}$	Coefficient de la table JANAF	
C_d	Coefficient de traînée d'une sphère	
C_{drag}	Coefficient de traînée pour un écoulement dispersé	
Cp	Capacité calorifique spécifique	$J/kg \cdot K$
Cu	Coefficient de perméabilité	$kg/m^3 s$
D	Diamètre de buse	m
D_k	Coefficient de diffusion de l'espèce k	m^2/s
$\bar{d}$	Diamètre caractéristique de particule	m
d_p	Diamètre de particule	m
$\mathbf{F}_{drag}$	Force de traînée sphérique	N
$\mathbf{g}$	Vecteur d'accélération gravitationnelle	m/s^2
H	Distance entre la surface et la buse	m
h	Enthalpie du champ interne	$W.s/kg$
h_F	Enthalpie du film liquide	$W.s/kg$
htc_p	Coefficient de transfert de chaleur convectif de patch	W/m^2K
K_{ht}	Coefficient de transfert interphases de chaleur	$W/m.K$
K_{drag}	Coefficient de glissement pour un flux d'interface	$kg/m.s$
k	Énergie cinétique	m^2/s
k_t	Énergie cinétique de turbulence	m^2/s
L	Chaleur latente de fusion	J/kg
m	Masse	kg
M	Masse molaire	kg/mol
n	Paramètre de distribution granulométrique	

Symbole	*Description*	*Unités*
n_R	Nombre de cellule dans la direction radiale	
n_θ	Nombre de cellule dans la direction azimutale	
n_Z	Nombre de cellule dans la direction axiale	
Nu	Nombre de Nusselt	
Nu_0	Nombre de Nusselt au point de stagnation	
N_x	Nombre de cellules caractéristiques	
p	Champ de pression	Pa
Pr	Nombre de Prandtl	
$P_{a,n}$	Nombre de particules absorbées au nième pas de temps	
$P_{inj,n}$	Nombre de particules injectées au nième pas de temps	
P_n	Nombre total de particules au nième pas de temps	
Pr_t	Nombre de Prandtl turbulent	
$P_{s,n}$	Nombre de particules éclaboussées au nième pas de temps	
q	Coefficient du modèle d'enthalpie-porosité	
$q_g^{"}$	Flux de chaleur convectif de gaz	W/m^2
$q_w^{"}$	Flux de chaleur convective de la paroi	W/m^2
R	Constante universelle des gaz parfaits	J/K mol
Re_D	Nombre de Reynolds basé sur le diamètre de la buse	
Re_F	Nombre de Reynolds de la région du film mural	
r	Distance par rapport au point de stagnation	m
r_s	Facteur de sous-relaxation	
Sc_k	Nombre de Schmidt de l'espèce k	
$S_{\rho\delta}$	Terme source (flux surfacique de densité)	kg/m^2
$S_{\rho\delta u}$	Terme source (quantité de mouvement tangentielle à la surface)	$kg/m \cdot s$
$S_{i,p}$	Quantité de mouvement échangé avec les particules	$kg/m^2 s$
$\mathbf{S}_{u_i}$	Terme source (quantité de mouvement interphases)	$kg/m^2 s^2$

Symbole	*Description*	*Unités*
$\mathbf{S}_{\mathrm{sms},\mathbf{u_i}}$	Terme source (quantité de mouvement solide/phase i)	$\mathrm{kg/m^2s^2}$
$\mathbf{S}_{\mathrm{drag,i}}$	Quantité de mouvement due à la force de trainé / phase i	$\mathrm{kg/m^2s^2}$
$\mathbf{S}_{\mathrm{vm,i}}$	Terme source (masse virtuelle)	$\mathrm{kg/m^2s^2}$
$\mathbf{S}_{\mathrm{buoy}}$	Terme source (quantité de mouvement due à la flottabilité)	$\mathrm{kg/m^2s^2}$
$\mathbf{S}_{\mathrm{sd}}$	Quantité de mouvement due à la force de trainé / solide	$\mathrm{kg/m^2s^2}$
$\mathrm{S}_{\mathrm{sms,h_i}}$	Terme source (énergie de changement de phase)	$\mathrm{W/m^3}$
t	Temps physique	s
T	Température	K
T^*	Température adimensionnelle	
$\mathrm{T_s}$	Température de la loi de Sutherland	
$\mathbf{u}$	Vecteur vitesse	$\mathrm{m/s}$
$\mathbf{u_F}$	Vecteur vitesse du film mural	$\mathrm{m/s}$
$\mathbf{u_P}$	Vecteur vitesse des particules	m/s
$\mathrm{u_{i(i=1,2,3)}}$	Composantes cartésiennes de vitesse	$\mathrm{m/s}$
V	Volume	$\mathrm{m^3}$
$\mathrm{x_{i(i=1,2,3)}}$	Composantes cartésiennes de position	m
$\mathrm{Y_k}$	Fraction massique de l'espèce k	
$\mathbf{z}$	Direction normale au film mural	

Symboles grec

Symbole	***Description***	***Unités***
α	Fraction volumique	
α_{eff}	Diffusivité thermique efficace	$kg/m \cdot s$
α_t	Diffusivité thermique turbulente	$kg/m \cdot s$
Δz_F	Épaisseur de la région du film mural	m
δ	Fraction volumique solide	
δ_F	Épaisseur du film liquide	m
ε	Taux de dissipation de l'énergie de turbulence	m^2/s^3
θ	Angle d'inclinaison de la pulvérisation	rad
κ	Diffusivité thermique / conductivité	W/mK
μ	Viscosité dynamique du champ interne	$kg/m \cdot s$
μ_F	Viscosité dynamique du film liquide	$kg/m \cdot s$
ν	Viscosité cinématique	m^2/s
ν_t	Viscosité cinématique turbulente	m^2/s
ρ_F	Densité de la région du film mural	kg/m^3
ρ_p	Densité des particules	kg/m^3
σ	Écart-type	
$\boldsymbol{\tau}$	Contrainte de cisaillement interne	N/m^2
$\boldsymbol{\tau_F}$	Contrainte de cisaillement du film liquide	N/m^2
$\boldsymbol{\tau_{eff}}$	Tenseur de cisaillement efficace	N/m^2
$\dot{\omega}_i$	Terme source génération/destruction des espèces	kg/m^3s

INTRODUCTION

0.1 Cadre général

Le givrage peut se produire lorsque les aéronefs sont au sol ou en vol. Au sol, la neige ou la pluie verglaçante tombant sur l'engin peut entraîner de la neige fondante, de la glace transparente ou une combinaison de ces dernières. En outre, le givrage peut se produire sur certaines ailes d'aéronef alors que ce dernier est au sol à des températures ambiantes supérieures au point de congélation en raison de la présence de carburant sous-gelé dans les réservoirs d'ailes (Thomas, Cassoni, & MacArthur, 1996).

Cette accrétion de givre modifie la géométrie des surfaces portantes des aéronefs ce qui perturbe leur décollage. Le givrage au sol est blâmé, en outre, pour le crash du :

• Vol 1363 Air Ontario entre Thunder Bay et Winnipeg via Dryden au Canada qui s'est écrasé le 10 mars 1989 peu après son décollage causant 24 morts et 45 blessés (Moshansky, 1992).

• Vol 405 USAir : un vol entre l'aéroport de La Guardia de New York et Cleveland, aux États-Unis, le 22 mars 1992 peu après son décollage de La Guardia. Les trains d'atterrissage ont quitté la piste, mais l'avion n'a pas réussi à prendre de l'altitude. Il s'est écrasé causant 27 morts et 21 blessés (National Transportation Safety Board, 1993).

Transport Canada a réagi en introduisant une exigence destinée à tous les aéronefs de la catégorie transport exploités au sein de lignes aériennes pour que soit créé un programme approuvé de lutte contre le givrage au sol (AGIP). La Federal Aviation Administration (FAA) des États-Unis et les organismes européens de réglementation ont adopté des exigences similaires (Paquet, Lawrence, & Shelley, 2008). Le paragraphe 602.11 du Règlement de l'aviation canadien (RAC) stipule notamment ceci : « Il est interdit d'effectuer ou de tenter d'effectuer le décollage d'un aéronef si du givre, de la glace ou de la neige adhère à toutes surfaces critiques ». Le dégivrage est donc obligatoire et il est défini d'après transport Canada (Transport Canada, 2005) comme une procédure par laquelle le givre, la

glace, la neige ou la neige fondante (c.-à-d. la contamination solide) est enlevé d'un aéronef en utilisant un liquide de dégivrage d'aéronef « Aircraft Deicing Fluid » (ADF), réchauffé pour permettre de nettoyer les surfaces. Les ADFs sont généralement des liquides à concentration en éthylène glycol, en diéthylène glycol ou en propylène glycol contenant de l'eau, des inhibiteurs de corrosion, des agents mouillants et des colorants. Ces liquides sont composés dans le but d'aider à l'enlèvement de la glace, de la neige et du givre sur les surfaces extérieures de l'aéronef. Ils assurent également une courte durée de protection antigivre.

Une partie du liquide de dégivrage appliqué aux surfaces des aéronefs durant les opérations de dégivrage s'écoule sur l'aire de trafic et finit par contaminer les effluents ou par s'infiltrer dans les sols souterrains. Pour assurer une gestion responsable et écologique des produits chimiques à concentration de glycol utilisés dans les opérations de dégivrage, l'exploitant aérien de concert avec le fournisseur de services et l'administration aéroportuaire doivent préparer des plans et des procédures détaillées visant la gestion du glycol. Le conseil canadien des ministres de l'environnement (CCME) a préparé des lignes directrices sur la qualité de l'eau qui sont pertinentes aux conditions qui prévalent au Canada. Les lignes directrices actuelles sur la qualité de l'eau pour les trois types de glycol sont 3 mg/L éthylène glycol, 31 mg/L diéthylène glycol, et 74 mg/L propylène glycol. Ces valeurs sont sujettes à modifications et les lignes directrices du CCME doivent être vérifiées régulièrement (au moins une fois par année) afin de s'assurer que les données actuelles sont utilisées.

0.2 Motivation

Les exigences de Transport Canada et du conseil canadien des ministres de l'environnement ont généré un prix supplémentaire non négligeable au niveau des coûts du transport aérien en saison hivernale. Il est difficile de trouver les tarifs exacts des services de dégivrage offerts aux compagnies aériennes, mais Marquis (2007) indique qu'il s'agit de quelques milliers de dollars par avion. Cependant, Privatefly (2017), une compagnie de location de jets privées indique qu'il s'agit d'une quinzaine de milliers de dollars canadiens pour dégivrer un avion de ligne, un prix qui peut varier en fonction de l'épaisseur du givre et de l'appareil. En effet,

ce prix est directement proportionnel à la quantité de liquide nécessaire (7,50 CAD/Litre en 2017). Cela constitue un chiffre d'affaires considérable si le coût est multiplié par le nombre de dégivrages à faire en saison hivernale. L'utilisation annuelle moyenne des ADFs aux États-Unis est estimée à environ 95 000 m^3 (United states Environmental protection Agency, 2012). Multiplier ce volume par le prix de Privatefly (2017) génère plus de 712 millions de dollars pour le marché des États-Unis seulement.

Inscrit dans ce cadre, diminuer les volumes de glycols utilisés par avion dégivré, par une optimisation des paramètres du jet, produira une baisse de coût intéressante au niveau des charges des compagnies aériennes en saison hivernale. Peu de références sont présentes dans la littérature qui visent à optimiser ce procédé. Chen, Wang, Gong, & Wang (2016) étudient expérimentalement l'influence de la température, du débit et de la durée de diffusion du jet liquide sur l'évolution temporelle de l'épaisseur de givre sur une plaque plane. Cette étude a contribué à l'élaboration d'une corrélation entre ces différents paramètres, mais en aucun cas elle n'étudie l'influence de l'angle d'inclinaison du jet ou de la distance entre la buse et la surface à dégivrer. Yakhya & Morency (2017) présentent la première étude dans la littérature qui vise à modéliser numériquement ce procédé.

0.3 Problématique de recherche

La mécanique des fluides numériques (MFN) est un excellent candidat pour modéliser le procédé de dégivrage au sol des aéronefs. Elle permet d'analyser différents problèmes pour lesquels les expériences sont difficiles à mettre à point et sont très coûteuses. De plus, avoir un modèle numérique du procédé permettra de déterminer les valeurs optimales des paramètres du jet d'ADF à appliquer en fonction de la forme de givre à décontaminer, qui n'est pas nécessairement la même d'un cas à un autre. Aussi, la conception d'un banc d'essais numérique du procédé permettra de faciliter la conception d'un banc d'essai expérimental, qui est certes plus coûteux.

Le procédé de dégivrage au sol des aéronefs par un jet liquide inclut plusieurs échelles, allant de la distance qui sépare la buse de la surface à dégivrer jusqu'à la plus petite gouttelette de

liquide, ainsi que du grand débit du liquide au niveau de la buse à la vitesse de dégivrage relativement lente. Modéliser ce procédé, avec tous ses détails, génèrerait des coûts de calculs prohibitifs. Une autre difficulté réside dans le fait que le procédé est multiphasique, contenant de l'air ambiant, du liquide de dégivrage, du givre et de l'eau issue de la fusion du givre qui est miscible avec le liquide de dégivrage. Par conséquent, le problème devient très complexe, ce qui se traduit par une multitude de modèles multiphasiques présents dans la littérature. Se fixer sur un modèle multiphasique adéquat constitue un atout dans cette recherche.

Pour fixer nos objectifs, nous allons commencer par énumérer quelques questions qui doivent être abordées afin de développer le modèle de dégivrage au sol :

- Quel est le modèle multiphasique le plus adéquat pour modéliser la propagation du jet liquide de dégivrage?
- Comment modéliser, adéquatement dans le même volume de contrôle, la fusion du givre en eau qui est soluble dans la solution d'ADF ?
- Comment coupler les différents aspects du procédé (injection d'ADF, impact d'un jet sur une surface, fusion de givre, mélange homogène ADF-eau) dans une seule simulation MFN ?

0.4 Objectifs

Le cadre général de cette recherche est l'application du dégivrage aéronautique. Nous nous intéressons particulièrement à la modélisation et la simulation du procédé de dégivrage au sol des aéronefs par un jet liquide chaud. Notre intérêt porte sur le développement de méthodes numériques qui permettent l'utilisation de la MFN pour l'investigation des effets des paramètres du jet sur les volumes d'ADF nécessaires à décontaminer une surface. Cet intérêt a pour objectif de réduire la consommation actuelle en liquide de dégivrage dans les aéroports diminuant ainsi les coûts financiers et environnementaux de ce procédé. Nous modélisons l'interaction entre un jet liquide chaud et du givre accrété a une surface. Ce modèle combine des phénomènes physiques différents qui ne sont pas encore couplés dans

les codes MFN commerciaux. Nous avons donc opté pour l'utilisation du code OpenFOAM-V6 comme cadre de développement open-source afin de ne pas être dépendant des librairies offertes par les codes commerciaux et de pouvoir ajouter librement des extensions au besoin. Ce choix, qui est due principalement à l'originalité de la problématique de recherche, est reflété par des contributions scientifiques au niveau des modèles mathématiques, des méthodes numériques et des résultats numériques.

Pour mieux illustrer la problématique proposée, la Figure 0.1 propose un volume de contrôle du procédé de dégivrage au sol des aéronefs. En rouge est présenté un jet liquide dispersé de liquide de dégivrage (ADF). Le jet impacte une surface contaminée par du givre (en bleu) formant un film liquide (en orange) composé par l'ADF issue du jet liquide et de l'eau issue de la fonte de givre.

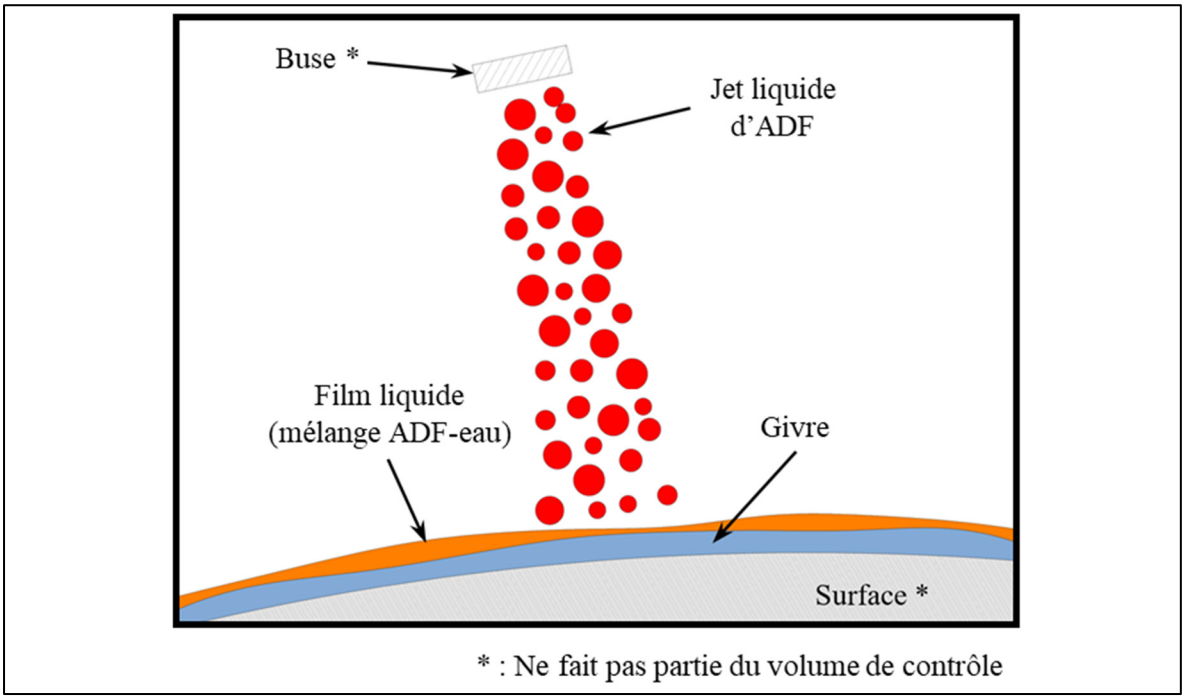

Figure 0.1 Schéma du volume de contrôle du procédé de dégivrage au sol des aéronefs

Les objectifs spécifiques de cette thèse sont définis comme suit :

1- Définir un modèle mathématique et une méthode numérique adéquats pour la modélisation du jet liquide.

2- Développer un modèle mathématique et une méthode numérique pour la modélisation et la simulation de la fonte de givre sous l'effet du jet liquide.
3- Développer et vérifier une méthode numérique couplant les deux modèles issus des deux objectifs précédents.

Chacun de ces objectifs cités ci-dessus constitue l'objectif principal d'un article publié durant cette thèse.

0.5 Méthodologie

Le jet liquide du procédé de dégivrage au sol des aéronefs est caractérisé par une grande dispersion des échelles géométriques. Cette dispersion est présentée dans le CHAPITRE 2. Cette caractéristique restreint le choix des modèles multiphasiques pour la modélisation du jet, favorisant une méthode lagrangienne qui a été justifié au sein de l'article présenté au CHAPITRE 2. Le choix du modèle du jet liquide résulte d'une revue de littérature et a été confirmé par (i) une étude de dépendance du maillage, (ii) une étude des effets des paramètres du jet, (iii) un test de validation de la pénétration de la pointe de pulvérisation et (iv) un test de validation du transfert de chaleur.

Le changement de phase du givre en eau se déroule dans un volume de contrôle assez particulier : (i) Ce dernier contient trois phases : givre (solide), ADF et eau (liquide) et air (gaz), (ii) le dégivrage est dû au contact avec un jet liquide dispersé dans l'air et (iii) l'eau résultante est miscible avec le liquide de dégivrage. Aucun modèle répondant à ces trois caractéristiques en même temps n'a été trouvé dans la littérature. Un nouveau modèle a été développé dans l'article présenté au CHAPITRE 3 pour modéliser le dégivrage. Le nouveau modèle consiste en une extension de la technique enthalpie-porosité pour qu'elle soit capable de modéliser la fusion dans un domaine contenant une troisième phase gazeuse. Ce modèle a ensuite été imbriqué au sein d'une approche d'écoulement diphasique particulaire modélisante l'impact du jet sur la surface contaminée. La phase liquide est enfin modélisée comme étant un mélange homogène (ADF + eau) avec des coefficients stœchiométriques se mettant à jour à chaque pas de temps, modélisant ainsi la miscibilité. Le nouveau modèle développé est vérifié par un test de diffusion, validé par (i) un test couplant la miscibilité et le

transfert de chaleur et (ii) un test de transfert de chaleur d'un jet avec une plaque plane. Enfin, la technique enthalpie-porosité étendue est calibrée pour un volume de contrôle caractéristique du procédé de dégivrage sol des aéronefs.

Le dernier aspect traité dans cette thèse est le couplage des deux modèles présentés au CHAPITRE 2 et au CHAPITRE 3. Une méthode multi-région a été développée définissant deux volumes de contrôle contigus. La première région dédiée au développement du jet liquide est résolue par les équations présentées au CHAPITRE 2. La deuxième région, quant à elle, est définie au voisinage de la surface contaminée et est résolue par les équations présentées au CHAPITRE 3. Des équations de transfert de masse, quantité de mouvement et d'énergie sont développées afin d'assurer la continuité de ces grandeurs au niveau de la frontière entre les deux régions. L'approche multi-région est vérifiée dans cet article par un test de pénétration de la pointe de pulvérisation. Cet article présente également une recalibration du coefficient de perméabilité de la technique d'enthalpie-porosité étendue en 3 dimensions.

0.6 Contributions

Les principales contributions de cette thèse peuvent être résumées comme suit:

- Une nouvelle méthodologie de validation des jets liquides dispersés (Ernez & Morency, 2019c).
- Une méthode MFN qui permet de simuler l'impact et le transfert de chaleur d'un jet liquide à grande échelle à un coût de calcul raisonnable (Ernez & Morency, 2019c).
- Un nouveau modèle de changement de phase (solidification/fusion) dans un domaine contenant une troisième phase (gaz) (Ernez & Morency, 2021a).
- Une méthode MFN qui permet de simuler l'évolution temporelle de la forme du givre dans un volume de contrôle caractéristique du procédé de dégivrage (Ernez & Morency, 2021a).
- Une méthode MFN qui permet la simulation du procédé de dégivrage au sol des aéronefs en 3D (Ernez & Morency, 2022).

Ces contributions ont été divulguées sous la forme de conférences et articles scientifiques. Au début de la thèse, une collaboration avec un finissant à la maitrise a permis d'étudier les effets transitoires du jet de dégivrage à l'aide du code commercial CCM+. Le travail a été publié dans le *Journal of Thermophysics and Heat Transfer* (Yakhya, Ernez, & Morency, 2019).

Cette collaboration a permis de faire une passation des travaux de recherche, ce qui a mis en relief rapidement la problématique de dispersion des échelles géométriques qui n'a pas été abordé dans la première étude. Ce point a été discuté la première fois lors de la *Conference of the Computational Fluid Dynamics Society of Canada (CFDSC)* par la proposition d'un modèle particulaire lagrangien pour la simulation du jet liquide (Ernez & Morency, 2018).

La conférence de la CFDSC est un environnement propice à l'échange d'idées concernant le développement de codes MFN, les études d'écoulements multiphasiques et transferts d'énergie. Cette conférence fournit, également, l'opportunité d'être invité par des journaux qui prévoient de publier des éditions spéciales dont le thème est connexe à celui de la conférence. Tous ces points ajoutés au fait de soutenir la communauté MFN au Canada rend la CFDSC le meilleur environnement, dans le cadre de cette thèse, pour divulguer des résultats de recherche préliminaires avant d'être publiés dans des revus scientifiques. Effectivement, la première conférence a permis d'être invité par *Emerald Publishing* pour la publication d'un article de journal dans l'*International Journal of Numerical Methods for Heat & Fluid Flow* (Ernez & Morency, 2019c).

La fonte de givre n'a pas encore été modélisée à ce stade. Aucun modèle n'était présent dans la littérature, également, qui permettait de modéliser la fusion dans un volume de contrôle contanant trois phases (solide, liquide et gaz). Cette problématique a fait l'objet de deux conférences : (i) l'algorithme et les méthode numérique ont été présentés à la CFDSC (Ernez & Morency, 2019a) et (ii) le modèle mathématique et les résulats ont été présentés à la conférence de l'institut aéronautique et spatial du Canada (Ernez & Morency, 2019b).

Le modèle présenté était une extension du modèle particulaire présenté précédement; une deuxième région a été ajouté où le givre interagissait avec le jet liquide. Les deux travaux

présentés aux deux conférences concernaient le même modèle avec une différence aux niveau des résulats présentés. Le travail présenté à la conférence de la *Canadian Aeronautics and Space Institute (CASI)* s'est d'avantage concentré sur la partie vérification et résultats. En revanche, le travail présenté à la CFDSC s'est concentré sur la partie algorithmique et code. Lors de ces deux conférences, la difficulté à valider un modèle aussi complexe a été soulignée. L'effort de recherche, à ce stade, s'est focalisé sur la deuxième région où la fonte de givre est modélisé. Le modèle de cette région devait être étudié à part avant d'être couplé à la premiere région. Le modèle a été amélioré en incluant un modèle particulaire eulérien ainsi qu'une équation de diffusion pour modéliser la miscibilité de l'eau issue de la fonte du givre avec le liquide de dégivrage. Le modèle ainsi qu'une série de vérifications, validations et calibrations ont été publiés dans le journal *Fluids* dans un l'édition spéciale « Complex Fluids and Flows: Algorithms and Applications » (Ernez & Morency, 2021a).

Une fois que le modèle de la deuxième région est validé, il reste à coupler les deux modèles et vérifier le couplage. Le modèle couplé et une série de vérification ont fait l'objet d'une conférence à la *CFDSC* (Ernez & Morency, 2021b).

L'article de conférence a été amélioré et d'autre tests de vérification et validation et calibration ont été ajoutés et publiés dans *Energies* dans l'édition spéciale « Advances in Thermophysics of Multiphase Flow » Ernez et Morency (2022).

0.7 Structure du document

Ce travail est présenté sous formes de thèse par article. Le premier chapitre présente une revue de littérature suivie par les chapitres qui reprennent chacun des trois articles. Une conclusion générale est présentée à la fin de la thèse.

CHAPITRE 1

REVUE DE LITTÉRATURE

1.1 Introduction

Ce chapitre présente une revue de littérature ayant pour objectif d'introduire au lecteur des études MFN des jets liquides et les modèles de changement de phase. Toutefois, une analyse détaillée des travaux de recherches est effectuée dans chacun des chapitres présentant les articles de journaux. La Figure 1.1 présente un schéma simplifié du procédé soulignant les deux principales thématiques auxquels doit répondre cette thèse : (i) les études des jets liquides en se concentrant sur le transfert de chaleur avec une plaque plane et les jets dispersés et (ii) les méthodes MFN de simulation de changement de phase (solidification / fusion).

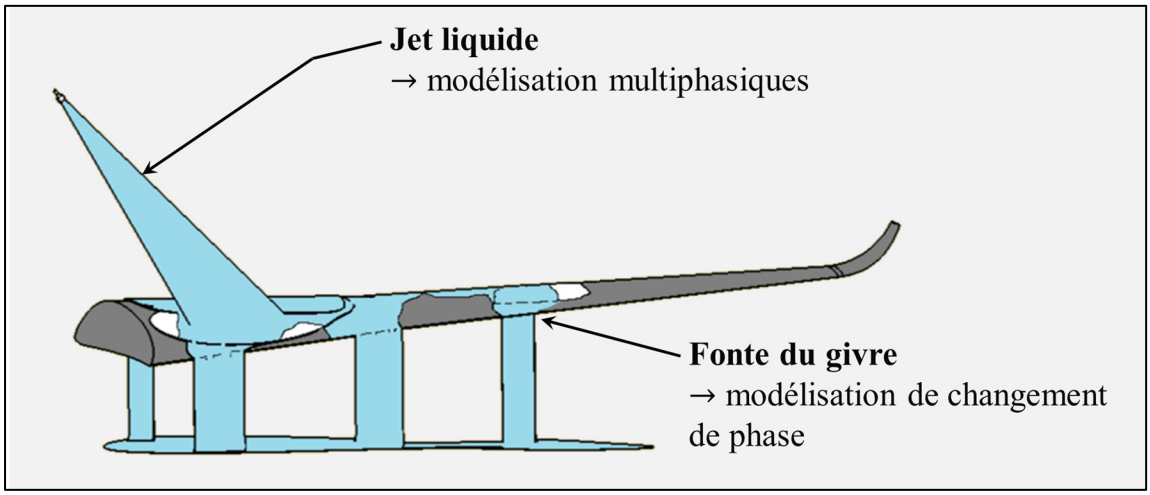

Figure 1.1 Schéma simplifié du procédé de dégivrage au sol des aéronefs

Cette revue de littérature permettra de positionner ce travail de recherche tout en étant complémentaire avec les revues de littérature présentées dans les articles issues de cette thèse. L'établissement de cette revue de littérature s'est déroulé en quatre étapes :

1- Une recherche dans la base de données de l'ÉTS des méthodes de modélisation multiphasique et les modèles de changement de phase. La recherche préliminaire couvrait les publications entre les années 2010 et 2017 (l'année de début de la thèse). Cette recherche a permis de diviser les méthodes de modélisation en plusieurs types.
2- Une recherche plus approfondie a ensuite été conduite jusqu'à atteindre l'origine des différentes méthodes, par exemple, le schéma discontinu Galerkin conservatif de la méthode level set publiée dans (Owkes & Desjardins, 2013) renvoie à la méthode level set conservative précise (ACLS) de (Desjardins, Moureau, & Pitsch, 2008) qui a amené à la recherche de l'origine de la méthode level set (Osher & Sethian, 1988).
3- L'étape 2 a entraîné des recherches concernant des aspects physiques comme la rupture des jets ou la fusion des solides ainsi que des résultats expérimentaux pour la validation des modèles développés.
4- Le code OpenFOAM-V6 a ensuite été exploré pour déterminer les modèles déjà implémentés. Cette exploration a permis à la fois de renforcer la revue de littérature et à adopter le style de programmation d'OpenFOAM. Un exemple de revue de littérature à propos des modèles de coefficient de traînée peut être consulté à l'annexe de l'article 2 présenté au chapitre 3.

Ce chapitre est divisé en deux sections. La première section traite des études MFN des jets liquides où les modèles multiphasiques sont classés selon leurs efficacités à simuler des jets liquide dispersés. La deuxième section présente, quant à elle, l'état de l'art concernant la simulation de la fusion/solidification. Les contributions apportées dans ce travail de recherche sont énumérées en conclusion.

1.2 Études MFN des jets liquide

De nombreux problèmes pratiques impliquent des écoulements de fluide contenant des particules ou des gouttelettes. Ces problèmes peuvent être rencontrés dans plusieurs domaines : de l'épandage d'un jet d'ADF sur une surface d'aéronef givré ou l'injection de carburants liquides dans les moteurs à combustion jusqu'au transport de polluants

particulaires dans l'atmosphère. À des fins d'analyse et de modélisation, ces problèmes peuvent être divisés en deux classes :

- La première classe regroupe les problèmes dans lesquels on peut supposer que les particules ne perturbent pas le champ d'écoulement comme les polluants atmosphériques ou les petits débris de glace issues d'un avion en vol. La solution se réduit alors à traquer des trajectoires de particules dans un champ de vitesses connu (Cantin, Morency, & Garnier, 2018 ; Ignatowicz & Morency, 2017).

- La deuxième classe regroupe les problèmes dans lesquels on ne peut pas négliger l'effet du mouvement des particules sur le champ d'écoulement. Nous citons à titre d'exemple l'injection de carburant à haute pression dans un moteur à combustion interne. La pulvérisation du carburant porte une quantité de mouvement suffisante pour entraîner et mettre en mouvement le gaz environnant. À son tour, le mouvement du gaz au voisinage des particules réduit la résistance à leur mouvement et permet à la pulvérisation de pénétrer beaucoup plus loin que ce ne serait autrement le cas. Il est donc important de tenir compte de l'interaction entre les particules et le gaz. Cette interaction est bien sûr toujours présente, mais elle est particulièrement significative lorsque la masse totale et l'impulsion des particules sont comparables à celles du gaz, et lorsque la taille des particules est suffisamment faible pour que le couplage d'une particule au gaz soit fort (Dukowicz, 1980).

Le procédé de dégivrage au sol des aéronefs s'inscrit plus dans la seconde catégorie, avec une grande pression de jet à l'alentour de 650 kPa (Yakhya & Morency, 2017) et une grande concentration de particules injectées dans l'air ambiant. L'interaction entre les particules et le gaz doit donc être prise en compte.

Du point de vue modélisation, les jets liquides s'inscrivent dans le domaine des écoulements multiphasiques de la mécanique de fluides. Il existe deux familles de modèles, les modèles multiphasiques à surface libre et les modèles multiphasiques particulaires.

1.2.1 Modèles multiphasiques à surface libre

Les modèles multiphasiques à surface libre sont des modèles eulériens qui visent à prédire l'évolution de la surface libre. La Figure 1.2 présente un volume de contrôle typique contenant trois phases. La surface libre est l'interface séparant deux phases.

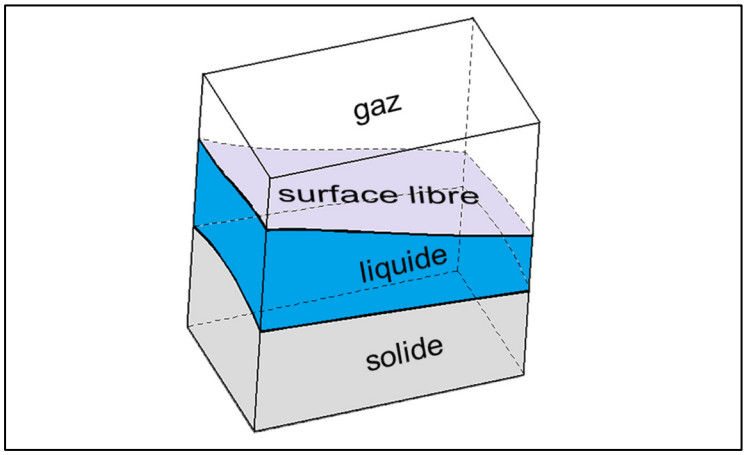

Figure 1.2 Volume de contrôle typique à trois phases

Les modèles multiphasiques à surface libre sont résolus par deux grandes familles de méthodes. Les méthodes volumiques qui se basent tous sur l'approche VOF (*volume of fluid)* proposée par Hirt & Nichols (1981) et les méthodes surfaciques basées sur l'approche LS *(level-set)* développé par Osher & Sethian (1988). Les méthodes volumiques consistent à assigner un champ de fraction volumique d'un des deux fluides à tout le domaine de calcul. Une cellule qui est complètement remplie de ce fluide aura une valeur du champ VOF égale à 1 et 0 dans le cas inverse. Les cellules se trouvant au niveau de la surface libre auront donc une valeur entre 0 et 1. Le champ VOF est advecté (ou transporté) via le flux et la surface libre est localisée par les cellules ayant une valeur de VOF entre 0 et 1.

L'avantage de cette méthode est qu'elle est conservatrice vu qu'une quantité physique (un volume) est transporté. Son désavantage est que pour avoir un profil net il faut réduire énormément la taille des cellules. La limite de la méthode VOF est mieux schématisée par la Figure 1.3 qui présente une gouttelette de liquide dans un environnement gazeux en 2D. Une

simple discrétisation d'un disque sans advection fait que la surface libre est représentée sur plusieurs cellules, cette diffusion sera ensuite amplifiée avec l'advection. Cette amplification dépendra du schéma de discrétisation de l'équation d'advection du champ VOF. Cette méthode est dite conservatrice avec une surface libre évasive (Dianat, Skarysz, & Garmory, 2017 ; Ling, Li, Sun, He, & Tao, 2015).

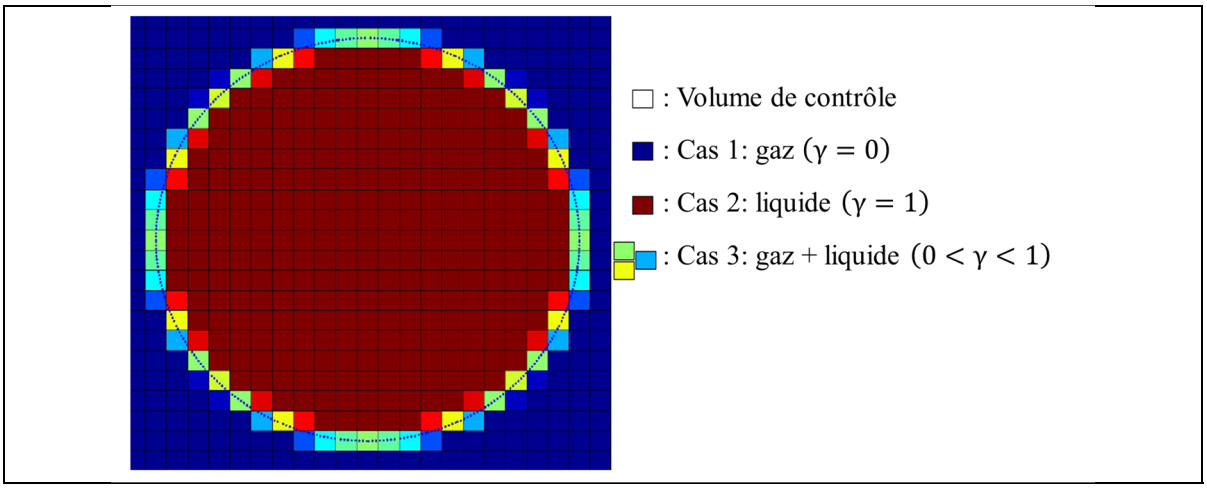

Figure 1.3 Modélisation VOF d'une gouttelette liquide dans un environnement gazeux

Dans l'autre méthode, les approches surfaciques consistent à advecter le champ des distances qui séparent les nœuds de la surface libre, appelé Level Set (LS). La surface libre est déterminée par la distance 0. Au contraire de la méthode VOF, ici on advecte une quantité non physique qui est la distance par rapport à une interface. Ces méthodes sont donc non conservatives mais offrent en revanche un profil net (Dianat et al., 2017 ; Gibou, Fedkiw, & Osher, 2018). Il existe aussi des méthodes hybrides comme la CLSVOF *(Conservatif Level Set Volume of Fluid)* de Sussman & Puckett (2000). Cette méthode consiste en une correction de la non-conservation de la méthode LS avec un champ VOF. Cependant elle dépend comme la VOF et la level-set du schéma d'advection utilisé. Gopala & van Wachem (2008) ont étudié différents schémas d'advection dans un cadre de simulation VOF. Leurs résultats sont résumés dans le Tableau 1.1 qui illustre que chaque méthode a ses inconvénients. Ces résultats démontrent encore que les modèles multiphasiques à surface libre sont extrêmement coûteux en temps de calcul pour la modélisation 3D de jet liquide dispersés.

Tableau 1.1 Résultats de comparaison de Gopala & van Wachem (2008)

Schéma d'advection	+	-
FCT	Simple	Perte de masse lors d'un écoulement turbulent
Lagrangian-PLIC	Précis et conservatif en 2D	Non précis en 3D
CICSAM	Précis et conservatif à 90%	Coûteux
Inter-gamma compressive scheme	Précis et conservatif à 100%	Extrêmement coûteux

1.2.2 Modèles multiphasiques particulaires

Les modèles multiphasiques particulaires sont conçus pour éviter les contraintes de coût de calculs des modèles multiphasiques à surface libre pour les écoulements dispersés. La Figure 1.4 reprend un schéma d'un jet liquide dispersé. Contrairement aux modèles à surface libre, les modèles particulaires ne visent pas à traquer les surfaces libres.

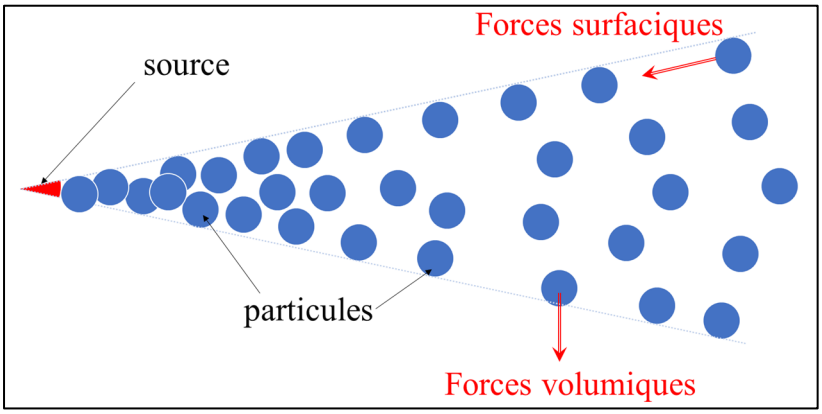

Figure 1.4 Schéma d'un jet liquide dispersé

En revanche, le modèle part de l'hypothèse qu'une phase est dispersée dans l'autre. Les gouttelettes sont assimilées à des particules qui sont sujettes à un ensemble de forces volumiques (gravité, masse virtuelle), surfaciques (portée, trainée) et de contacts inter-particules (collisions, ruptures).

Le premier enjeu dans ce domaine de recherche est la détermination de ces forces selon la forme géométrique des particules. Pour le coefficient de trainée par exemple, on cite les travaux de Haider & Levenspiel (1989) pour les particules non sphériques et Liu, Mather, & Reitz (1993) pour les particules sphériques déformées. Le second enjeu est la détermination des modes de ruptures ainsi que leur modélisation. La Figure 1.5 (Chigier & Reitz, 1996) présente les quatre régimes de rupture les plus étudiés. De gauche à droite ; (a) Rupture de Rayleigh qui est définit par la formation de gouttelettes de diamètre plus grand que le diamètre de buse. (b) Rupture primaire où des gouttelettes de même diamètre que la buse se forme en ligne. (c) Rupture secondaire où des gouttelettes de diamètre plus petit que le diamètre de buse et la rupture commence à une certaine longueur après la buse. (d) L'atomisation caractérisée par des gouttelettes beaucoup plus petite que le diamètre de buse et la rupture commence dès la sortie de buse.

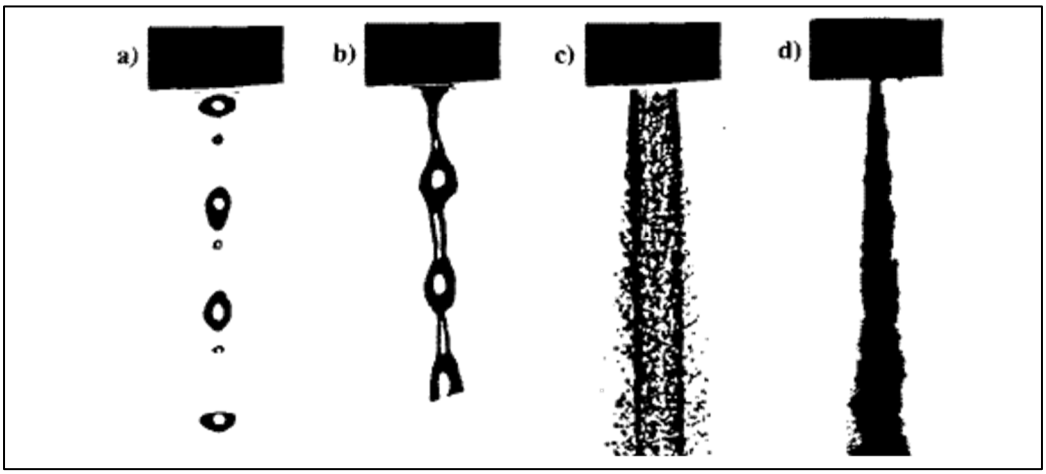

Figure 1.5 Quatre régimes de rupture des jets liquides
Tirée de Chigier & Reitz (1996, p. 112)

Chigier & Reitz (1996) présentent des relations entre le régime de rupture et le nombre de Reynolds et le nombre d'Ohnesorge. Lin & Reitz (1998) présentent quant à eux une autre relation des régimes de rupture avec les nombres de Weber de la phase gazeuse We_g et la phase liquide We_l. Ces deux relations sont schématisées par la Figure 1.6.

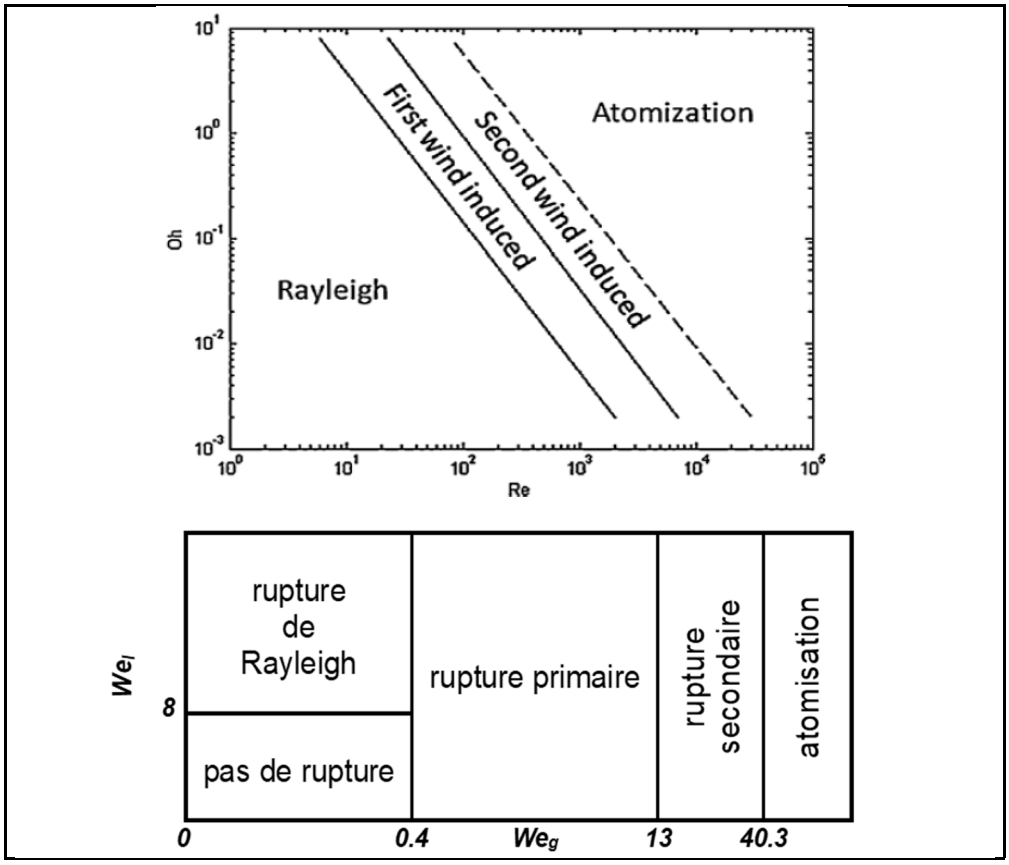

Figure 1.6 Classification des régimes de rupture selon : en haut tirée de Reitz (1978 p. 167) et en bas selon Lin & Reitz (1998)

On commence à parler de dispersion des échelles géométriques à partir de la rupture secondaire vue le nombre et la tailles des gouttelettes et c'est ici que les modèles particulaires deviennent moins couteux que les modèles multiphasiques à surface libre. L'article présenté au CHAPITRE 2 justifie l'efficacité des modèles particulaires dans le cadre du dégivrage au sol des aéronefs.

1.3 Modèles de changement de phase appliqué à la MFN (solidification / fusion)

La simulation MFN de changements de phase est traitée dans la littérature dans des études qui concernent le stockage d'énergie, plus spécifiquement les matériaux à changement de phase (MCP). La majorité des développements sont issus de ce domaine d'application. Du

point de vue physique, le phénomène de fusion d'un solide peut être divisé en deux catégories selon le mode de transfert thermique :

- Fusion à convection : La fusion à convection (naturelle ou forcée) se produit si un solide est placé dans un domaine fluide où règnent certains champs de pression et de température. En convection naturelle, aucun flux n'est imposé, le gradient de pression ou/et de température généré à l'interface solide-fluide induit le mouvement de tout le fluide. Ce mouvement empêche le solide d'avoir une couche froide de fluide à ses alentours. Ce mouvement persiste jusqu'à l'atteinte d'un point d'équilibre en faisant fondre le solide (Bertrand et al., 1999). En convection forcée, un flux de masse règne dans le domaine. Ce flux baisse la pression et/ou augmente la température à l'interface du solide-fluide provoquant sa fusion (Ma, Zhang, Wang, Furui, & Xi, 2010).
- Fusion à contact étroit : la fusion à contact étroit se produit si une source de chaleur et un solide sont mis en contact l'un contre l'autre pendant la fusion du solide. La situation physique implique le mouvement de la source de chaleur ou du solide ce qui empêche l'accumulation de la masse fondue entre la source et le solide (Groulx & Lacroix, 2006).

La fusion du givre dans le procédé de dégivrage au sol des aéronefs se produit par suite de l'épandage d'un film d'ADFs. Le flux continu du jet fait que ce film est toujours en mouvement. On parle dans ce procédé donc plus de convection forcée. Du point de vue énergétique, en négligeant la convection, les phases liquide et solide sont régies par les équations de chaleur (1.1) et (1.2).

$$\rho c_l \frac{\partial T_l}{\partial t} = \vec{\nabla}.\left(k_l \vec{\nabla} T_l\right) \tag{1.1}$$

$$\rho c_s \frac{\partial T_s}{\partial t} = \vec{\nabla}.\left(k_s \vec{\nabla} T_s\right) \tag{1.2}$$

où ρ et T représentent la densité et la température, c et k la capacité et la conductivité thermique avec l et s dénommant les phases liquide et solide.

Il faut prévoir l'évolution de l'interface liquide solide. Donc, ici encore, le problème se résume à traquer une surface libre. Mais dans la partie précédente la surface libre gaz-liquide évoluait sous l'effet de l'énergie cinétique. Dans le cas de changement de phase, la vitesse de la surface libre liquide-solide, d'après la condition de Stefan, est contrôlé par la quantité de chaleur latente absorbée L_F (ou perdue) à la frontière (équation 1.3).

$$\rho L_F \frac{d\xi(t)}{dt} = k_s \vec{\nabla} T_s - k_{sl} \vec{\nabla} T_l \tag{1.3}$$

avec ξ le profil de l'interface liquide-solide.

Ces trois équations constituent le problème de Stefan (1891). Initialement l'effet de la convection était négligé jusqu'à ce que Sparrow, Patankar, & Ramadhyani, (1977) aient démontré que la convection thermique avait un rôle à jouer dans des problèmes de changement de phase. Velraj, Seeniraj, Hafner, Faber, & Schwarzer, (1999) quant à eux, vont plus loin en expliquant que la convection thermique naturelle était le mode de transfert dominant dans le processus de fusion.

En MFN, deux types de méthodes existent pour résoudre ces problèmes : (i) les méthodes à domaines multiples et (ii) les méthodes à domaine unique. Les méthodes à domaines multiples sont basées sur la formulation complète de Stefan c'est-à-dire un domaine va être régi par l'équation de chaleur de la phase liquide et le deuxième va être régi par l'équation de chaleur de la phase solide puis la condition de Stefan, est implémentée comme condition limite entre les deux domaines. On utilise ici un modèle eulérien de modélisation multiphasique que ce soit la méthode VOF ou level-set. Tan, Lim, & Khoo, (2007) présentent un excellent exemple de cette méthode. Ils utilisent une méthode VOF couplée à une méthode de raffinement de maillage au voisinage du front de fusion afin d'avoir une surface libre nette. Un système d'équations différent est résolu dans chaque domaine : les équations de Navier-Stokes modélisent la partie liquide et seulement l'équation de chaleur est résolue pour la partie solide. Bien que la méthode de raffinement de maillage réduit l'épaisseur de la surface libre, cette méthode dépend toujours du schéma d'advection de la fraction volumique du liquide. Les méthodes à domaine unique, quant à elles, se résument à la résolution d'un

seul système d'équations aux dérivées partielles. La méthode la plus populaire est l'enthalpie-porosité de Voller & Prakash (1987). Cette méthode introduit une zone dite trouble. La zone trouble est caractérisée par une fraction volumique du solide strictement entre 0 et 1. Cette région est en fait le voisinage de l'interface liquide-solide. Dans cette région l'enthalpie du mélange liquide-solide est exprimée comme étant l'enthalpie sensible à laquelle on additionne la chaleur latente de la phase liquide. Zeneli, Nikolopoulos, Karellas, & Nikolopoulos (2021) comparent les deux méthodes et trouvent les même avantages et inconvenants pour la méthode VOF et level-set pour les méthodes à domaines multiples. Quant à la technique enthalpie-porosité, ils stipulent qu'elle est caractérisée par une convergence rapide et une grande précision. Cependant, une attention particulière doit être portée concernant la variation de densité ainsi que la manipulation de la vitesse des solides. Dans le cas de la modélisation du procédé de dégivrage au sol des aéronefs, le choix de la méthode de changement de phase adéquate dépendra de l'architecture du code traitant le jet liquide. Il convient également de mentionner que les modèles proposés en littérature n'incluent pas une troisième phase gazeuse dans le domaine de calcul. Un développement d'un modèle répondant à cette nécessité est présenté au CHAPITRE 3.

Au CHAPITRE 4, l'article présente une méthode MFN combinant les deux modèles issus des deux premiers articles via une approche multi-région. La méthode résultante simule l'interaction entre un jet liquide de dégivrage et une surface contaminée par du givre. C'est la première méthode MFN documentée dans la littérature qui est capable de simuler un scénario de dégivrage. Pareillement, aucune étude expérimentale dans la littérature n'a investigué les effets des paramètres du jet liquide sur la décontamination d'une surface. Ce manque visible de littérature engendre une complexité à la phase de vérification des méthodes et validation des modèles. La contribution majeure de cet article est l'approche multi-région permettant le couplage des deux modèles multiphasiques particulaires (lagrangien et eulérien). L'approche multi-région a été validée versus le modèle lagrangien proposé dans l'article présenté au CHAPITRE 2. Il a été démontré dans cet article que l'approche multi-région n'influe pas sur la quantité de mouvement du fluide traversant la frontière limitant les deux régions. Une revue technique sur les paramètres d'injection est aussi présentée dans cet article.

1.4 Conclusion

Ce chapitre a consisté en une revue de littérature complémentaire à celles présentées au sein des trois articles publiés durant cette thèse. Le phénomène de dispersion des jets liquide ainsi que ses caractéristiques ont été introduits. Les modèles multiphasiques ont été discutés et répartis en modèles multiphasiques à surface libre et modèles particulaires. Un avantage préliminaire des méthodes particulaires a été expliqué et sera renforcé par l'article présenté au CHAPITRE 2. La problématique de changement de phase est aussi discutée dans cette revue de littérature. Les méthodes MFN les plus utilisées dans la littérature ont été présentées et réparties en deux catégories. L'article présenté au CHAPITRE 3 explique le choix de méthode à la suite des résultats issus de l'article qui le précède. Le procédé de dégivrage au sol des aéronefs combine différents aspects physiques complexes. L'enjeu technique de ce travail de recherche est de combiner un modèle de jet liquide et un modèle de fusion de givre qui répondent aux caractéristiques du procédé étudié. Le CHAPITRE 4 présente une méthode MFN capable de simuler l'interaction entre le jet d'ADF et la surface contaminée dans le même volume de contrôle permettant ainsi des études paramétriques du procédé.

CHAPITRE 2

EULERIAN - LAGRANGIAN CFD MODEL FOR PREDICTION OF HEAT TRANSFER BETWEEN AIRCRAFT DEICING LIQUID SPRAYS AND A SURFACE

Sami Ernez [a], François Morency [b]

[a,b] Department of mechanical engineering, École de Technologie Supérieure,
1100 Notre-Dame Ouest, Montréal, Québec, Canada H3C 1K3

Article published in « International Journal of Numerical Methods for Heat & Fluid Flow »,
August 2019

2.1 Abstract

Purpose – This paper presents a Eulerian-Lagrangian model of aircraft ground deicing that avoids the scale dispersion problem caused by the considerable distance between the spray nozzle and the surface to be de-iced. Verification is done using the case of a hot particle liquid spray impinging on a horizontal flat plate. The impinged particles flow outwards radially from the impingement zone and form a hot film wall. The computed wall heat distribution is verified. In the end, an inclination spray angle study is presented.

Design/methodology/approach – The problem is divided into two regions. First, a 3D region is created for the evolution of the Lagrangian particle spray. A second 2D region is provided for the formation of a liquid film. The two regions exchange mass, momentum, and energy through an interface. Heat losses are modelled through particles and liquid film cooling and evaporation, particle splash, and heat transfer to a fixed temperature plate.

Findings – spray penetrations agree within 90% of experimental results when injected into a chamber of a pressure of 1 bar. For this case study, the heat transfer is maximized when the inclination angle is close to 30° of the spray.

Originality/value – The model presented makes it possible to simulate the impingement and heat transfer of a large-scale liquid spray at reasonable computational cost. This model is a first attempt at the CFD simulation of ground deicing.

Keywords: Liquid spray impingement, two-region Eulerian-Lagrangian model, heat transfer.

Paper type Research paper.

2.2 Introduction

In Northern countries, aircraft icing can occur on the ground due to climatic conditions. Ice affects the aerodynamic properties of aircraft and makes the take-off difficult or even impossible. Following several crashes during take-off (Moshansky, 1992 ; National Transportation Safety Board, 1993), Canada instituted regulations forbidding any plane with frosted surfaces from taking off, and requiring that such aircraft be immediately deiced. North American standards require that deicing operations be carried out using a hot impinging spray of aircraft deicing fluid (ADF). Transport Canada acknowledges only the most up-to-date SAE specifications, and all fluids applied to aircraft must meet these high standards (Transport Canada, 2005). ADFs are highly miscible with water, and consequently, deicing fluid that flows onto the tarmac contaminates effluents and seeps into underground soils. In 2005, to limit the polluting effects of aircraft deicing, the Canadian Council of Ministers of the Environment prepared water quality guidelines for airports meeting Canada-specific conditions (Transport Canada, 2005). Pursuant to those guidelines, de-icers must either recover or recycle ADFs. However, this additional operation increases ground deicing costs for aircraft. It is therefore evident that reducing the volume of ADF needed to de-ice an aircraft carried both environmental and economic benefits.

The preheated ADF is sprayed directly onto the contaminated surface. Transport Canada also recommends that the fluid be dispensed as close to the surface as possible to prevent it from cooling down. Further, it should be applied at a particular angle to avoid damaging the aircraft surface (Transport Canada, 2005). To date, no parametric studies on aircraft ground deicing have investigated the impingement distance and the liquid spray angle effects on melting an iced surface.

Today, CFD codes are commonly used to predict in-flight aircraft icing accretion (Beaugendre, Morency, & Habashi, 2006). CFD has proved useful in the prediction of the super-cooled droplet impingement area (Bilodeau, Habashi, Baruzzi, & Fossati, 2016) and in

the design of de-icing and anti-icing systems (Pourbagian & Habashi, 2015 ; Wong, Papadakis, & Wong, 2013). An in-flight icing model can use a Eulerian or a Lagrangian model for the droplet motion, loosely coupled with airflow and a 2D water film region on the aircraft surface. For deicing liquid spray, however, the airflow is driven by the warm droplet, and must be tightly coupled to the droplet motion. For aircraft in-flight icing, the droplet concentration is relatively low (Bourgault, Habashi, Dompierre, & Baruzzi, 1999), and droplets come from a large area in front of the aircraft. On the ground, the droplets come from a known small area and are highly concentrated. On the aircraft surface, instead of accreting ice, the film flow melts the existing ice. In-flight thermal deicing involves heat transfer from the surface toward the external flow (Reid, Baruzzi, Aliaga, Aubé, & Habashi, 2010), while ground deicing involves heat transfer from the external flow toward the surface. Similar for in-flight icing, CFD models could provide useful information to help improve ground de-icing activities. Yakhya, Ernez and Morency (2019) proposed the first study in literature that aims to model the aircraft ground deicing by CFD. It presents an impinging spray model coupled to a film model using volume of fluid method. However, the proposed problem is characterised by a large dispersion of the geometric length scales: a distance of 5D between the spray injection and the wall (sufficient at this verification step), a particle diameter of around D/100 and an average film thickness of D/25.

The simulation of the liquid spray break-up into particles with a Eulerian method like volume of fluid or level set requires a very high number of cells. These approaches focus on tracking the free boundary evolution. In this context, the free boundary should be drawn on several cells (Desjardins et al., 2008 ; Shinjo & Umemura, 2010). Cell sizes should be smaller than droplets, which will lead to a very fine mesh. Given this constraint, a CFD bench test of aircraft ground deicing should not model the spray primary break-up. Rather, it should start with a droplet distribution modelling the spray behaviour just at the exit of the nozzle and model it as a particulate two-phase flow.

Here, two approaches are possible: a Eulerian approach and a Lagrangian approach. Durst, Milojevic and Schönung (1984) discussed the basic equations of the two approaches and their numerical treatment for a 2D vertical pipe case. They found that the Lagrangian

approach is more appropriate for polydispersed particle size distributions. The Eulerian approach is more appropriate for flows with high particle concentrations. Zhang & Chen (2007) compared the modeling performance of the two approaches. They studied steady-state particle dispersion in a clean room and unsteady particle dispersion in a section of an aircraft cabin with a coughing passenger. They concsluded that the Eulerian approach is efficient for steady-state calculations while the Lagrangian approach performed better in unsteady-state conditions. Fotovat, Bi and Grace (2017) reviewed the characterization methods of electrostatics and the mechanisms of charge generation and distribution in fluidized beds. Similar to Durst, Milojevic and Schönung (1984), they concluded that the Lagrangian approach is more appropriate for polydispersed particle size distributions.

This paper proposes a 3D CFD model for predicting convective heat transfer in aircraft ground deicing process. The liquid spray is composed of polydispersed particle size. The process is modeled under unsteady-state conditions and given the large dimensions of the computation domain compared to the impinging jet sizes, low void fractions will be obtained. The Lagrangian approach is therefore favored in this work.

Combustion is surely the area that most solicits research to study liquid sprays and their interaction with a solid surface. The Lagrangian approach was used in many works. The interaction of the spray with a wall produces a wall film. In (Habchi, Foucart, & Baritaud, 1999) , the liquid film mass is tracked in a Volume of Fluid (VOF) framework. A Lagrangian method to track the liquid film also exists (Zhao et al., 2017, 2018). The Lagrangian method is more effective in combustion since the liquid film is considered as a dispersed phase. Another research field where impinging sprays were investigated is the spray quenching process. A Eulerian spray model interacting with a film model was used in (Edelbauer, Zhang, Kopun, & Stauder, 2016) to investigate the heat transfer with a preheated solid. The liquid film does evaporate because of the high temperature of the solid. In the quenching process, the film mass does not decrease as much as in combustion and a spray deposited film is created. The Eulerian representation of the film model is more adequate here since the liquid is considered as a continuous phase. In aircraft ground deicing the liquid film formed gain mass at each time step while it’s fed by the spray and also the ice melting. Similar to

(Yakhya, Ernez and Morency, 2019) the VOF method for the film modeling is then more interesting in the proposed case study. Given the proposed model constrains, the impinging spray model with Lagrangian particles and Eulerian film is superior to other impinging spray models.

The present paper aims to identify critical parameters of the liquid spray and evaluate its optimum value in order to reduce the volume of ADF used to de-ice aircrafts. The main objectives of this research are to:

• Design a CFD bench test of aircraft ground deicing process on OpenFOAM.

• Correlate the ice mass removed by volume of ADF with spray parameters.

Velraj et al. (1999) demonstrated that convection is the dominant heat transfer mode in ice melting. ADF sprays remove ice by weakening and melting it under the effect of pressure and heat transfer. The specific objective of this paper is to propose a model that enables the CFD investigation of the convective heat transfer in deicing operations. Convective heat transfer predictions provide a basis for comparison between different deicing scenarios. The spray is modeled as a cloud of Lagrangian particles that impact an iced wall. The particles feed a Eulerian fluid film with momentum and heat.

No experimental data are available in literature to evaluate if breakup occurs or not during the aircraft ground deicing process. Chigier and Reitz (1996) reported that nozzle design effects are important for spray breakup. Varying the injection pressure with a constant mass flow rate will influence the Weber number which according to Chigier and Reitz (1996) determine if breakup occurs or not. One direct effect of spray breakup is to have smaller droplets that increase heat and mass transfer surface. For aircraft de-icing, the cool down of the spray with distance is an important feature and break-up should be included in the model.

OpenFOAM provides a transient solver “reactingParcelFoam” for compressible, turbulent flows with a reacting, multiphase particle clouds, and surface film modeling (Holzmann, 2017). The original solver was developed to model the particle deposition on a surface. It also handles chemical reactions and combustion. Kampili (2017) implemented a decay heat model and simulated nuclear aerosol transport. This solver models Lagrangian particles

interaction with a Eulerian film model. However, it does not handle particles breakup. We propose to add aircraft ground deicing to open a new application field for this solver. In this paper, we present the particles breakup model implementation in this solver. To do so, the ReactingCloud class was replaced by the SprayCloud class that enables breakup. The combustion module was also deleted for calculation efficiency. The model implementation is validated against spray tip penetration. For the verification of the new solver capabilities for ground aircraft de-icing simulations, the effect of droplet size on the wall heat transfer is investigated in this work.

The next section defines the impinging particle spray problem presented in the context of aircraft ground deicing. Section 3 demonstrates the mathematical model of the Lagrangian spray and the liquid film. Section 4 explains all the numerical schemes and describes the solver structure. Section 5 is dedicated to the model verification and a first validation step. Finally, a study on spray's inclination is shown at the end of the paper.

2.3 Problem definition

In the aircraft ground deicing process, an operator equipped with a special deicing vehicle directs the deicing nozzle toward the surface to be decontaminated. The ADF, heated to a specific temperature, is sprayed on the contaminated parts of the aircraft surface. The spray forms, in contact with ice, a liquid film flowing along the surface. Figure 2.1 shows a simplified scheme of the problem versus the real system.

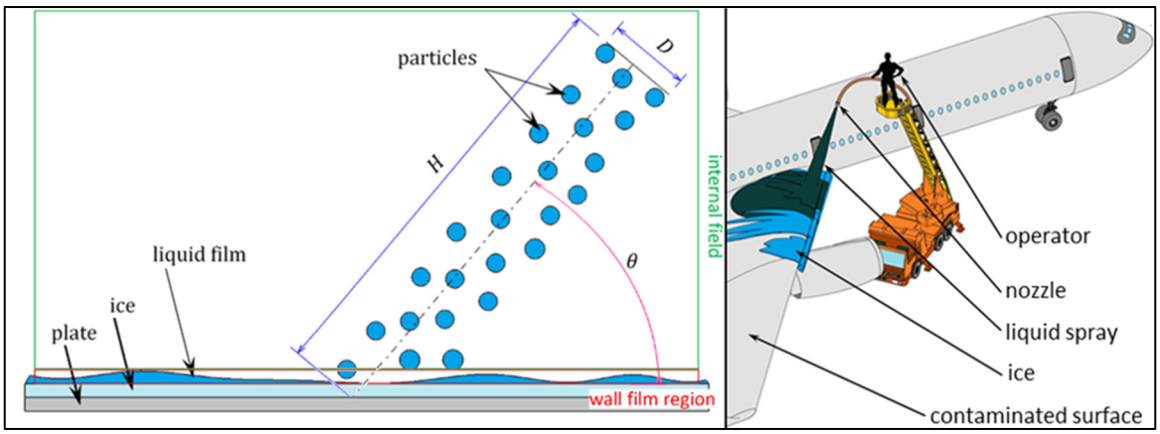

Figure 2.1 Simplified versus real scheme of aircraft ground de-icing process

In this study, the flow from the nozzle exit to the contaminated surface is modeled. The ice melting is not modeled. The nozzle exit position is fixed in time, contrary to the reality where the nozzle position changes in time. The proposed work aims to model the spray propagation from the nozzle exit until his impact on the surface using a Euler-Lagrange approach and a two-way coupling. A discoid particle source is placed inside the domain to model the spray at the nozzle's exit level. Particles may break up in the air and splash upon impinging the contaminated surface. The air is initially at rest, and the surface is at the air temperature. As the latent energy of the surface is high, the plate temperature is constant.

For this paper, the plate and the ice volume are excluded from the computation domain, but the water film is included. The spray impinges a flat plate representative of a contaminated surface. The spray particle impacts a surface contaminated by frost. Upon impact, the particles enter the wall film region and create a liquid film. The liquid film flows over the surface, exchanges heat with ice and falls to the ground. In this article, the ability of a model to predict the heat transfer between a hot Lagrangian particle spray and a cold surface is investigated. The ice is not yet included; verification and validation of the Eulerian-Lagrangian model should be done first.

2.4 Mathematical model

This section describes the mathematical model of the problem. It is divided into three paragraphs. The first presents the gas phase equations that will be solved in a 3D mesh called here the internal field. The second paragraph briefly describes the Lagrangian particle model. The last paragraph describes the liquid film model for the surface flow. These equations will be resolved in a 2D domain called the “wall film region”.

In terms of object-oriented programming, three classes are created in OpenFOAM: “internalField”, “sprayCloud” and “wallFilmRegion”. Those classes exchange mass, momentum, and energy. Figure 2.2 summarises the physical phenomena that are responsible for these exchanges. Particle and film evaporation generate a source term in the internal field continuity equation. The drag force exerted by particles disturbs the internal field velocity. For the energy balance, convective heat fluxes are modelled at the particle and film surfaces. The particles impacting and splashing on the film generate three source terms in the wall film region’s governing equations.

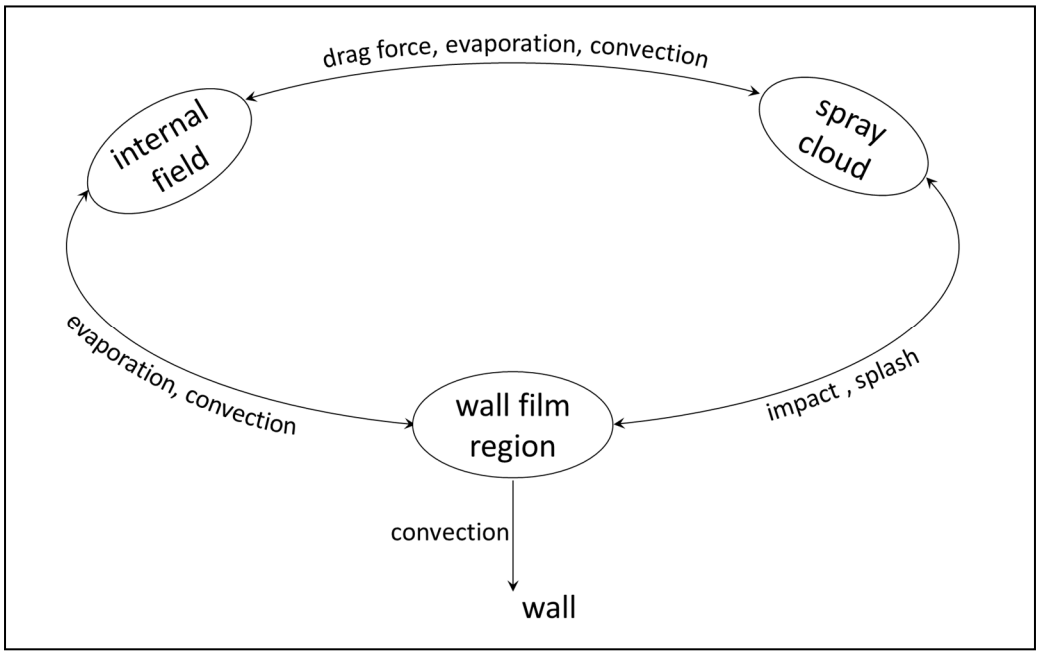

Figure 2.2 Physical phenomena linking particles, liquid film and gaseous phase

2.4.1 Internal Field

The mass conservation (continuity) equation of sprayFilmFoam is given by the following equation:

$$\frac{\partial \rho}{\partial t} + \nabla.(\rho \mathbf{u}) = \dot{S}_{\rho,I\leftrightarrow P} + \dot{S}_{\rho,I\leftrightarrow F} \tag{2.1}$$

where $\dot{S}_{\rho,I\leftrightarrow P}$ and $\dot{S}_{\rho,I\leftrightarrow F}$ are mass source terms due to the evaporation of spray particles and liquid film, respectively.

$$\dot{S}_{\rho,I\leftrightarrow P} + \dot{S}_{\rho,I\leftrightarrow F} = \frac{\dot{m}_{F,evap} + \dot{m}_{P,evap}}{V_{Cell}} \tag{2.2}$$

The momentum conservation is given by the following equation:

$$\frac{\partial \rho \mathbf{u}}{\partial t} + \boldsymbol{\nabla}.(\rho \mathbf{u}\mathbf{u}) = -\boldsymbol{\nabla} p + \rho \mathbf{g} + \boldsymbol{\nabla}.\left(2\mu_{eff} D(\mathbf{u})\right) - \boldsymbol{\nabla}\left(\frac{2}{3}\mu_{eff}\nabla(u)\right) + \dot{S}_{u,I\leftrightarrow P} \tag{2.3}$$

where the effective viscosity μ_{eff} is the sum of the molecular and turbulent viscosity and the rate of strain (deformation) tensor $D(\mathbf{u})$ is defined as $D(\mathbf{u}) = \frac{1}{2}(\nabla \mathbf{u} + (\nabla \mathbf{u})^T)$. The pressure gradient and gravity force terms are rearranged numerically in the following form: $-\nabla p + \rho \mathbf{g} = -\nabla p_{rgh} - (\mathbf{g}.\mathbf{r})\boldsymbol{\nabla}\rho$, where $p_{rgh} = p - \rho \mathbf{g} \cdot \mathbf{r}$ and $\mathbf{r}$ is the position vector from the wall. $\dot{S}_{u,p}$ is a momentum source term due to the drag force exerted by the fluid (ambient air) on liquid particles. The effect of the liquid film flow on the internal field is neglected. The internal field is designed to initially have a chemical composition similar to the atmosphere. The evaporation of spray particles and fluid film introduces a third gaseous species. Aircraft deicing is carried out with an ADF spray. To be aligned with the literature, verifications are carried out using a water spray instead of ADF, so the third species will be noted here by the symbol X. These three gaseous entities are modelled by their mass fraction Y_k (gaseous) and are calculated from the equation of species in the internal field.

$$\frac{\partial \rho Y_k}{\partial t} + \nabla.(\rho Y_k \mathbf{u}) = \nabla.(\rho D_k \boldsymbol{\nabla} Y_k) + \dot{\omega}_k \tag{2.4}$$

with D_k being a diffusion coefficient of the k species and $\dot{\omega}_k$ is a source term describing the generation of a species. The spray and the liquid film contain only the X species, so $\dot{\omega}_{N_2} = \dot{\omega}_{O_2} = 0$ and $\dot{\omega}_{H_2O} = V_{evap}/V_{cell}$.

Energy conservation is ensured by solving the following enthalpy equation:

$$\frac{\partial \rho h}{\partial t} + \nabla.(\rho h \mathbf{u}) + \frac{\partial \rho K}{\partial t} + \nabla.(\rho K \mathbf{u}) - \frac{\partial p}{\partial t} = \nabla.(\alpha_{eff} \boldsymbol{\nabla} h) + \rho \mathbf{u} \cdot \mathbf{g} + \dot{S}_{h,I\leftrightarrow P} + \dot{S}_{h,I\leftrightarrow F} \tag{2.5}$$

where $K \equiv \|\mathbf{u}\|^2/2$ is the kinetic energy per unit mass, h the enthalpy per unit mass, and α_{eff} is the effective thermal diffusivity, which is the sum of laminar and turbulent thermal diffusivities:

$$h = h_s + \sum_i c_i \Delta h_f^k \tag{2.6}$$

$$\alpha_{eff} = \frac{\mu}{Pr} + \frac{\rho \nu_t}{Pr_t} = \frac{\kappa}{\rho c_p} + \frac{\rho \nu_t}{Pr_t} \tag{2.7}$$

where $h_s = c_p T$ is the sensible enthalpy, c_k and Δh_f^k are respectively the molar fraction and the standard enthalpy of formation of the k species. κ is the thermal conductivity, c_p is the specific heat at constant pressure, μ is the dynamic viscosity, ν_t is the turbulent (kinematic) viscosity, Pr is the Prandtl number and Pr_t is the turbulent Prandtl number. $\dot{S}_{h,I\leftrightarrow P}$ models the particle evaporation and heat convection, and $\dot{S}_{h,I\leftrightarrow F}$ models the same phenomena at the liquid film level.

2.4.2 Spray cloud

The cylindric Lagrangian spray injector is specified by diameter, direction, velocity, mass flow, number of parcels per second and the droplet properties, namely, the temperature, the droplet diameter distribution, and the mixture composition. The droplet size distribution

injected is polydispersed. Polydispersed distributions are generally closer to the experimentally observed distribution of the sprays than their mono-dispersed counterparts. They are often specified using a normal, log-normal, or Rosin-Rammler distribution (Nasr, Yule, & Bendig, 2002). In OpenFOAM, the distribution can also be specified as a user-defined probability density function or as a cumulative density function table for mass, volume or number of droplets. In this paper, the Rosin-Rammler mass distribution is used to describe the mass distribution of particles as a function of diameter. The description of this distribution can be found in Yoon et al. (2004).

The particle locations and speeds are obtained from Newton's second law. Particles are subjected to the gravity and drag $\mathbf{F}_{\mathrm{drag}}$ forces. Different models of drag coefficients are available in the literature depending on particle sphericity. For example, Liu, Mather and Reitz (1993) developed a diesel engine spray model in which the particle drag coefficient changes dynamically with flow conditions during the particle's lifetime. This model gave better results than the commonly used rigid sphere drag coefficient model. However, the dynamic drag coefficient involves a particle distortion as another additional parameter. Liu, Mather and Reitz (2010) found that changing the drag coefficient from a rigid sphere model to a dynamic model has relatively little effect on spray penetration and does influence the distribution of particle sizes within the spray. So, given the difference between the two applications and for the sake of simplicity, the common rigid sphere drag coefficient (Stiesch, 2003) is used in this work:

$$\mathbf{F}_{\mathrm{drag}} = \frac{3}{4}\frac{\rho \mathrm{m_P}}{\rho_P \mathrm{d_p}} \mathrm{C_D}(\mathbf{u} - \mathbf{u_P})|\mathbf{u} - \mathbf{u_P}| \tag{2.8}$$

$$\mathrm{C_D} = \begin{cases} \dfrac{24}{\mathrm{Re_p}}\left(1 + \dfrac{1}{6}\mathrm{Re_p^{\frac{2}{3}}}\right) & \mathrm{Re_p} \le 1000 \\ 0.424 & \mathrm{Re_p} > 1000 \end{cases} \quad ; \quad \mathrm{Re_p} = \frac{\rho}{\mu}.\mathrm{d_p}.\left\|\mathbf{u} - \mathbf{u_p}\right\| \tag{2.9}$$

The momentum transfer between particles and the wall film region is modelled by adding the impacting particles' linear momentum to the thin film momentum equation (Meredith, 2010 ; Stanton & Rutland, 1998). Finally, the particle evaporation is modelled. The main

assumptions are: (i) negligible effects of internal particle circulation and (ii) infinitely high diffusivity. For the sake of brevity, equations can be found in Nobile (2015).

2.4.3 Wall film region

The thin liquid film adheres to the contaminated plate. The thin liquid film model is based on two approximations: i) the film velocity in the normal direction of the adherence surface is assumed to be zero, and ii) the gradient of a variable in a collinear direction to the adherence surface is negligible compared to the gradient of the same variable in the direction normal to the surface. This means that thermal conduction and shear stress are dominant in the normal direction of the adherence surface. The liquid film is characterised by a thickness δ. Initially, the contaminated surface is supposed to be dry, i.e., it has a zero-film thickness. This thickness varies due to the mass transfer with the liquid spray. The particle mass, moment and thermal energy that leave the internal field and head towards the wall film region are added as source terms in the liquid film conservation equations. As they enter the wall film region, the particles become a continuous mass uniformly distributed in the mesh cells. Any surface tension effects are neglected in the film model. The film thickness δ is calculated by solving the continuity equation at the film level (Meredith, 2010 ; Stanton & Rutland, 1998):

$$\frac{\partial \rho_F \delta_F}{\partial t} + \nabla_s . (\rho_F \delta_F \mathbf{u_F}) = \dot{S}_{\rho,P\leftrightarrow F} + \dot{S}_{\rho,F\leftrightarrow I} \tag{2.10}$$

$$\dot{S}_{\rho,F\leftrightarrow P} + \dot{S}_{\rho,F\leftrightarrow I} = \frac{\dot{m}_{F,evap} + \dot{m}_{imp} + \dot{m}_{spl}}{S_{Cell}} \tag{2.11}$$

where ∇_s is the 2D differential operator in the two directions tangential to the wall film region and $\mathbf{u}_F$ is the average film velocity in the normal direction of the film. $\dot{S}_{\rho,P\leftrightarrow F}$ is a source term that models the variation of the film mass flow rate due to the impact and splashing particles and film evaporation. The mass flow rate of the impacting particles $\dot{m}_{imp}$ is provided by the resolution of the Lagrangian particle's equation of motion in the internal flow region.

The momentum conservation in the wall film region is given by the following equation:

$$\frac{\partial \rho_F \delta_F \mathbf{u_F}}{\partial t} + \nabla_s . (\rho_F \delta_F \mathbf{u_F} \mathbf{u_F}) = -\delta_F \boldsymbol{\nabla_s}(p) + \rho_F \mathbf{g} \delta_F + \frac{\boldsymbol{\tau_F}}{A_{wall}} - \dot{\mathbf{S}}_{u,P\leftrightarrow F} \tag{2.12}$$

with

$$\dot{\mathbf{S}}_{u,F\leftrightarrow P} = \frac{\dot{\mathbf{M}}_{tang}}{A_{wall}} = \frac{\dot{m}_{P_{impact}} \mathbf{u_{imp}} - \dot{m}_{splash} \mathbf{u_{spl}}}{A_{wall}} \tag{2.13}$$

$$\boldsymbol{\tau_F} = \boldsymbol{\tau_{wall}} + \bar{\boldsymbol{\tau}} = \mu \left(\frac{\partial \mathbf{u}_F}{\partial z}\right)_{z=0} + \mu \left(\frac{\partial \mathbf{u}_F}{\partial z}\right)_{z=\delta} \tag{2.14}$$

The film enthalpy is calculated from the energy equation neglecting the radiation term (Meredith, 2010 ; Stanton & Rutland, 1998):

$$\frac{\partial \rho \delta_F h_F}{\partial t} + \nabla_s . (\rho \delta_F \mathbf{u_F}) h_F = q_w(h_{F,s}) + \dot{S}_{h,F\leftrightarrow P} + \dot{S}_{h,F\leftrightarrow I} \tag{2.15}$$

where h_F is the enthalpy averaged in the film normal direction. $h_{F,S}$ is the film sensible enthalpy, $q(h_{F,s})$ is the film heat flux. $\dot{S}_{h,F\leftrightarrow P}$ is the heat flux due to impacting and splashing particles. $\dot{S}_{h,F\leftrightarrow I}$ is the heat flux loss to evaporation. $q(h_{F,s})$ is computed using two predefined heat transfer coefficients, the first between the film and the contaminated surface, and the other, between the film and the internal field. In OpenFOAM (V2 to V6), two models are implemented for the heat flux coefficient, htc. The first allows setting a constant heat transfer coefficient between the liquid film and the contaminated surface. The second allows setting a convective heat transfer coefficient condition between the wall film region and the internal field given by the following equation (NEXTfoam, 2017):

If $Re_F < 5.10^5$

$$htc_p = \frac{0.664 Re_F^{0.5} Pr^{0.333} \kappa}{L} \tag{2.16}$$

else

$$htc_p = \frac{0.037 Re_F^{0.8} Pr^{0.333} \kappa}{L} \tag{2.17}$$

with $Re_F = L\,\rho_F|\mathbf{u_F} - \mathbf{u_B}|/\mu_F$, $\mathbf{u_B}$ is the tangential velocity vector at the boundary and L a constant length scale that, according to Incropera et al. (2007), models the flat plate length.

2.5 Numerical method

In this CFD study, the heat transfer between a flat plate and a liquid film formed by a spray impingement is investigated. This section presents the general structure of the solver, the numerical schemes discretizing the fields, as well as the boundary conditions.

2.5.1 General solver structure

Most of the computational domain is designed to model the gaseous part of the problem where particles evolve, namely, the internal field. The rest of the domain is defined as a wall film region. This multi-region approach offered by OpenFOAM allows solving different equations in different sets of cells in the same computational domain. The pressure field is corrected twice. The transient calculations are made with a maximum allowed Courant number CFL_{max} set in the pre-processing phase using an adjusted time step strategy. At each time step, the particle number is computed using the particle number update equation:

$$P_n = P_{n-1} + P_{s,n-1} - P_{a,n-1} + P_{inj,n} \tag{2.18}$$

The current particle mass is then computed, resolving the particle evaporation equations. Finally, the particle momentum is calculated solving Newton's second law equation. After resolving all the spray cloud equations (Nobile, 2015), the solver calculates the intersections between the particle trajectories and the thin film. It evaluates $P_{s,n}$ and $P_{a,n}$ for the next time step and resolves the thin film equations. Next, the internal field's density, momentum, species and energy are computed in a PISO loop (Holzmann, 2017) with a stability criterion of 10^{-5} for $\mathbf{U}$ and h in this study. The pressure is then solved using the geometric algebraic multigrid (GAMG) solver (Greenshields, 2017). The turbulent kinetic energy and dissipation are computed at the end of each time step.

2.5.2 Numerical schemes

Standard numerical schemes OpenFOAM are used to solve the mathematical model. Time derivative terms are computed using an implicit, bounded first-order transient discretization scheme (Greenshields, 2017). Gradient terms are computed using the second-order Gauss linear scheme. This scheme is based on the Gaussian divergence theorem for the volume integral of a gradient field (Greenshields, 2015). It actually specifies a standard finite volume discretization of the Gaussian integration that requires the interpolation of values from the cell centres to the cell face centres. This interpolation scheme is then given by the linear input, which means a linear interpolation or a central differentiation.

The divergence of the velocity $\mathbf{U}$ and the effective shear tensor $\boldsymbol{\tau}_{\mathbf{eff}}$ are both calculated with the same Gauss linear scheme used for the discretization of the gradients, while the rest of divergence terms are computed using a first-order upwind scheme which determines the value of a scalar from the direction of the flow. In this paper, the results (Nusselt distribution) are similar to that which would be obtained with a second-order scheme. In fact, the airflow is not critical for the Nusselt distribution, but rather, the droplet flow is the main actor. The numerical scheme for the Laplacian calculation is similar to that presented for the gradient. Finally, linear interpolations are used for all calculations.

2.5.3 Boundary and initial conditions

This study examines the radial evolution of the Nusselt number between the liquid film and a contaminated surface. Therefore, the computational domain used in this study is cylindrical. Figure 2.3 presents the case configuration and the domain mesh. The computational domain dimensions are based on the spray source diameter $\mathrm{D} = 1\mathrm{cm}$, with a radius of $7\mathrm{D}$ and a height of $5.5\mathrm{D}$.

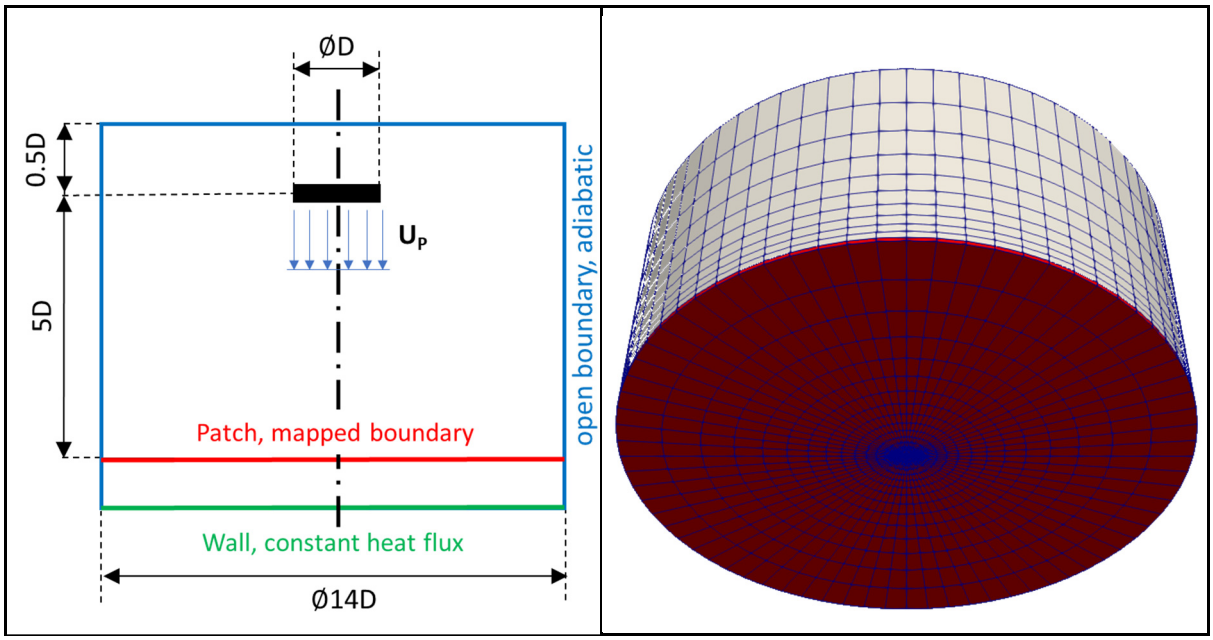

Figure 2.3 Water spray impingement case configuration (left) and numerical mesh (right)

The spray source is placed at $H = 5D$ from the flat plate. The upper and radial boundaries of the entire domain (blue boundary on the figure) constitute a wave transmissive patch (NEXTfoam, 2017). This boundary condition avoids wave reflections, which allows species to flow in and out of the computation domain freely, depending on flow conditions. A zero-gradient boundary condition is set for temperature. The open boundary corresponds to the real case. The lower boundary is a wall with a constant heat flux of $q_w = 15.10^3 W/m^2$. This boundary does not reflect the real case, and was only set to compute the Nusselt number and make comparison with (Stevens & Webb, 1991) experimental results. A mapped boundary is set between the wall film region and the internal field to allow the transfer of all source terms presented in the mathematical model. Initially, the domain is set at a cold temperature of $T_0 = 273.15K$ and the spray is injected at a hot temperature of $T_{P0} = 333.15K$. 1 million particles per second, with a diameter between 1mm and 8mm, are injected normally into the surface with a velocity magnitude of 1m/s. The spray mass flow rate is 0.04 kg/s.

2.5.4 Thermophysical properties

The internal field is composed of three species. The density ρ, the specific heat capacity c_p and the dynamic viscosity μ are weighted by species mass fraction Y_{specie}. They also vary as a function of the temperature. The density is computed using the perfect gas law (eq. 10.a). The specific heat capacity of each species is computed as a function of the temperature from a set of coefficients taken from JANAF tables of thermodynamics (eq. 10.b). Finally, the dynamic viscosity follows the Sutherland law. The parameter values used in equations (2.19), (2.20), and (2.21) are presented in Table 2.1.

$$\rho = \sum_{specie} Y_{specie} \times \frac{M_{specie}}{RT} p \tag{2.19}$$

$$cp = \sum_{specie} Y_{specie} \times \left(\left((a_{4,specie}T + a_{3,specie})T + a_{2,specie}\right)T + a_{1,specie}\right)T + a_{0,specie} \tag{2.20}$$

$$\mu = \frac{As\sqrt{T}}{1 + T_s/T} \tag{2.21}$$

Table 2.1 Thermophysical parameters

	$M[kg/m^3]$	$A_s[kg/msK^{-1}]$	$T_s[K]$	a_0	a_1	a_2	a_3	a_4
N_2	28.01	1.67×10^{-6}	171	3.3	1.41×10^{-3}	-3.96×10^{-6}	5.64×10^{-9}	-2.44×10^{-12}
O_2	32	1.67×10^{-6}	171	3.21	1.13×10^{-3}	-5.76×10^{-7}	1.31×10^{-9}	-8.77×10^{-13}
H_2O	18.02	1.67×10^{-6}	171	3.39	3.74×10^{-3}	-6.35×10^{-6}	6.97×10^{-9}	-2.51×10^{-12}

For the particles and the liquid film, the density is set to $10^3 kg/m^3$, $cp = 4.18 \times 10^3 J/kg.K$, and the Prandtl number is set to 0.7**.**

2.6 Model verification

In this study, the spray is defined as a particle stream. Throughout the simulation, the liquid film is fed by a non-stationary distribution of particles. Therefore, steady state conditions will not be reached. However, the film temperature will reach a certain value and will continue to

fluctuate in a narrow range around this value. Here, a "pseudo-steady state" regime is defined when the film temperature reaches this range. In this section, a mesh convergence study is elaborated and the influence of the jet parameter (spray's Reynold Number Re_D , number of particles and mass flow rate) on the Nusselt number Nu_D, film thickness δ_F and film Reynolds number Re_F is presented. To evaluate the influence of the parameters, a temporal average of different quantities (film thickness, velocity, temperature, etc.) in the pseudo-steady state regime is computed.

2.6.1 Mesh dependency study

A grid study is conducted to analyse the effect of the spatial discretization on the solution. The meshes used in this study have a cylindric shape, as presented in Figure 2.3. The meshes are characterised by the number of cells n_r, n_φ and n_z in the radial, angular and axial directions, respectively. Figure 2.4 presents a top view ($z = 5.5D$) and an axial section ($y = 0$) of a coarse mesh. The location of the spray source is also presented.

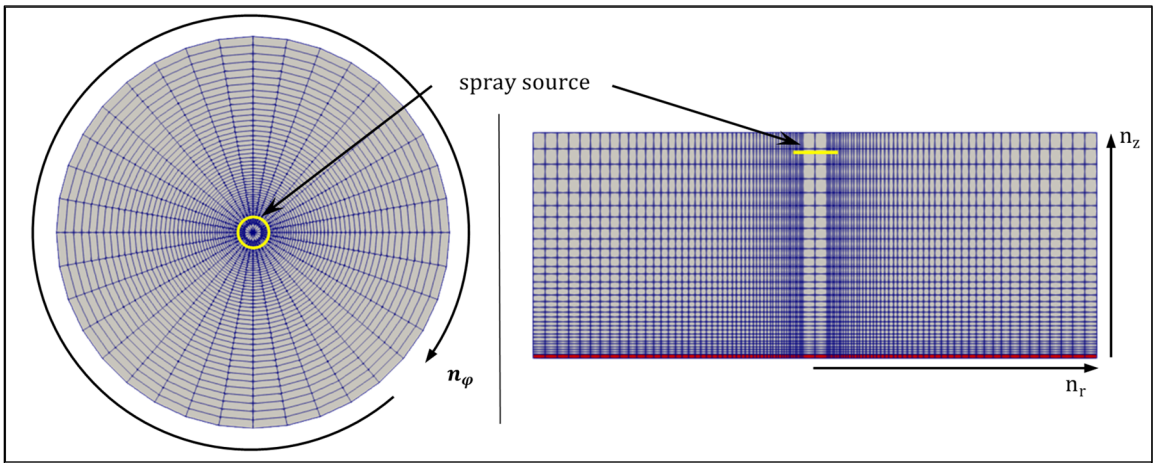

Figure 2.4 Top view (left) and axial section (right) of the mesh

As presented in Figure 2.4, refinements are made in the radial and axial directions, and thus, the meshes are finer near the stagnation zone (the area where the jet impacts the wall). Four meshes were tested: a coarse, a normal, a fine, and an extra-fine mesh. Table 2.2 presents the characteristics of different meshes, and n_{tot} is the total number of cells.

Table 2.2 Characteristics of different meshes

	Coarse	Normal	Fine	Extra-fine
n_r	42	84	140	210
n_φ	36	72	120	180
n_z	30	60	100	150
n_{tot}	4.54×10^4	3.63×10^5	1.68×10^6	5.67×10^6

Figure 2.5 shows an axial section of the internal field superimposed on the wall film region (coarse mesh). The difference between the two sides of the figure is that, on the right part, the spray cloud is hidden to display the cells adjacent to particles. For the wall film region and the spray cloud, temperatures are presented (T_P and T_F), and for the internal field, the mass fraction Y_{H_2O} is presented. The temperatures show that the spray and the film are cooled in the direction of the flow. For the internal field, we notice that the water vapour is concentrated near the stagnation zone, likely due to the gas stagnation in this zone.

Several studies have focused on the film flow created by the interaction of a continuous jet with a wall (X. Liu, Gabour, & Lienhard, 1993 ; Stevens & Webb, 1991). In those studies, the local Nusselt number Nu_D is expressed as a function of the radial distance from the centre of the stagnation zone. There are many structural differences between a continuous jet and a spray, and as a result, there may also be differences when comparing the heat transfer of both with a wall. However, far from the impingement zone, the heat transfer should depend more on the local thin film properties than on the jet properties. Thus, the injection parameters, such as the Reynolds number Re_D and the inclination angle θ, should have similar effects on the heat transfer. For this reason, the Nusselt number is defined as in those experimental studies. At each time step, the film temperature is not necessarily axisymmetric because particle distribution is poly-dispersed, and so heat transfer could vary instantly as a function of the azimuthal angle φ. A mapped Nusselt number $\widetilde{Nu}_D$ is defined here as a function of the radial distance and the azimuthal angle. Equations (2.22), (2.23), and (2.24) present respectively the mapped, local and global Nusselt number.

$$\widetilde{\mathrm{Nu}}_{\mathrm{D}}(r,\varphi,t) = \frac{h(r,\varphi,t)D}{\kappa} = \frac{D}{\kappa} \times \frac{q_w}{T_{spray} - T_{Film}(r,\varphi,t)} \tag{2.22}$$

$$\mathrm{Nu}_{\mathrm{D}}(r,t) = \frac{1}{2\pi} \int_{\varphi=0}^{2\pi} \widetilde{\mathrm{Nu}}_{\mathrm{D}}(r,\varphi,t)\, d\varphi \tag{2.23}$$

$$\overline{\mathrm{Nu}}_{\mathrm{D}}(t) = \frac{1}{7D} \int_{r=0}^{7D} \mathrm{Nu}_{\mathrm{D}}(r,t)\, dr \tag{2.24}$$

Figure 2.6 presents the temporal evolution of the global Nusselt number and of the global film thickness. The vertical discontinuous lines mark the time when the film thickness and the Nusselt number reach their average stable values. The film thickness reaches its maximum range before the Nusselt number does. This appears to be logical, as the Nusselt number cannot reach a steady state if the film thickness is still evolving.

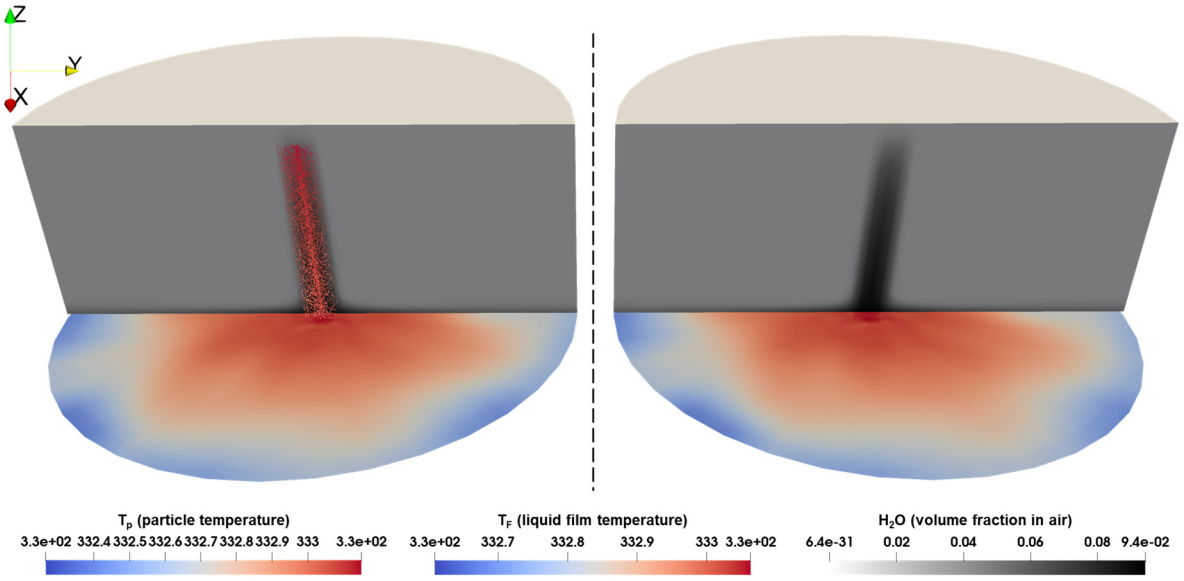

Figure 2.5 Particle and film temperature and spatial distribution of H_2O species

The first liquid quantity formed in the wall film region is cooled by convection from the internal field. At the second discontinuous line, a hot gas layer in the internal field is fully developed above the wall film region (see Figure 2.7). Therefore, the pseudo-steady state

regime starts when the Nusselt number reaches its average stable value (the second discontinuous line).

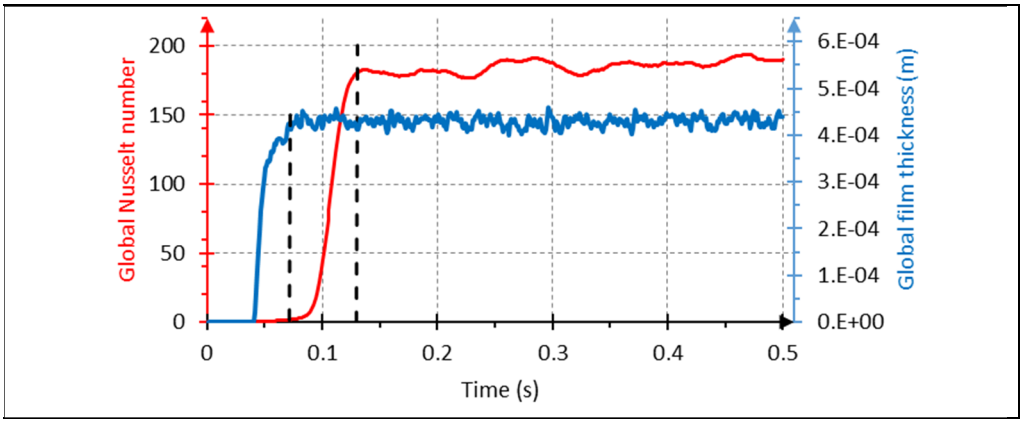

Figure 2.6 Film thickness (blue) and global Nusselt number (red) evolution

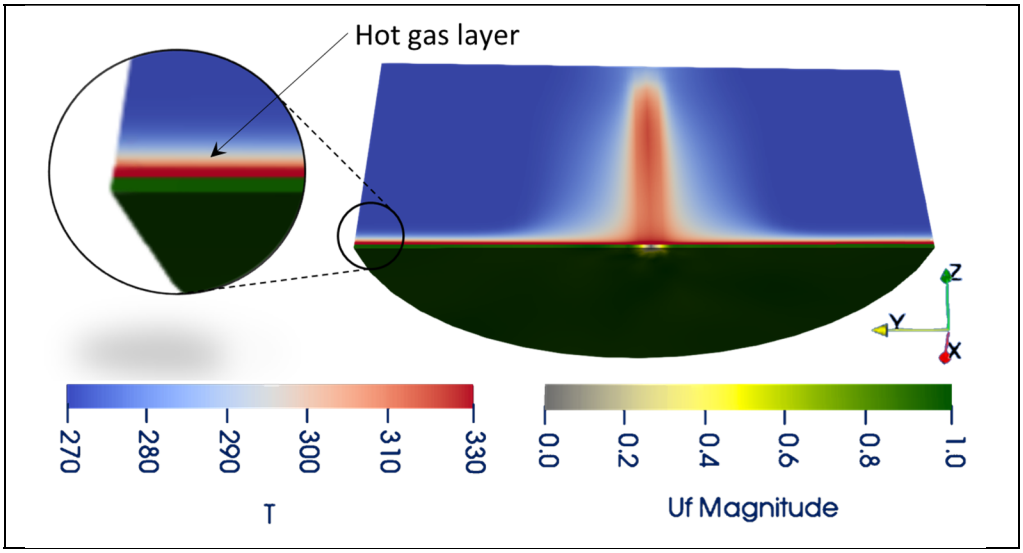

Figure 2.7 Hot gas layer above the film surface

The local Nusselt number of the pseudo-steady state regime, $Nu_{D,S}$, is defined as a time-averaged function of the local Nusselt number presented in equation (2.24) from the start point of the pseudo-steady state regime to the simulation end time (0.5 s). The mesh dependency study is based on $Nu_{D,S}$. Figure 2.8 presents the radial distribution and variation

(based on the extra fine mesh) of the local Nusselt number. The Nusselt number variation is defined in equation (2.25).

$$\text{variation}_{\%}(r) = 100 \times \frac{\left|\text{Nu}_D(r) - \text{Nu}_{D,Xfine}(r)\right|}{\text{Nu}_{D,Xfine}(r)} \tag{2.25}$$

For the coarse, normal and fine meshes, the variation increases with radial distance. In the stagnation zone, all the meshes give almost the same Nusselt number value (a variation of less than 1%). The normal mesh has a maximum variation of 1% at $r = 7D$, which makes it acceptable in an engineering context. From this point on, the normal mesh (3.63×10^5cells) will be used in all simulations.

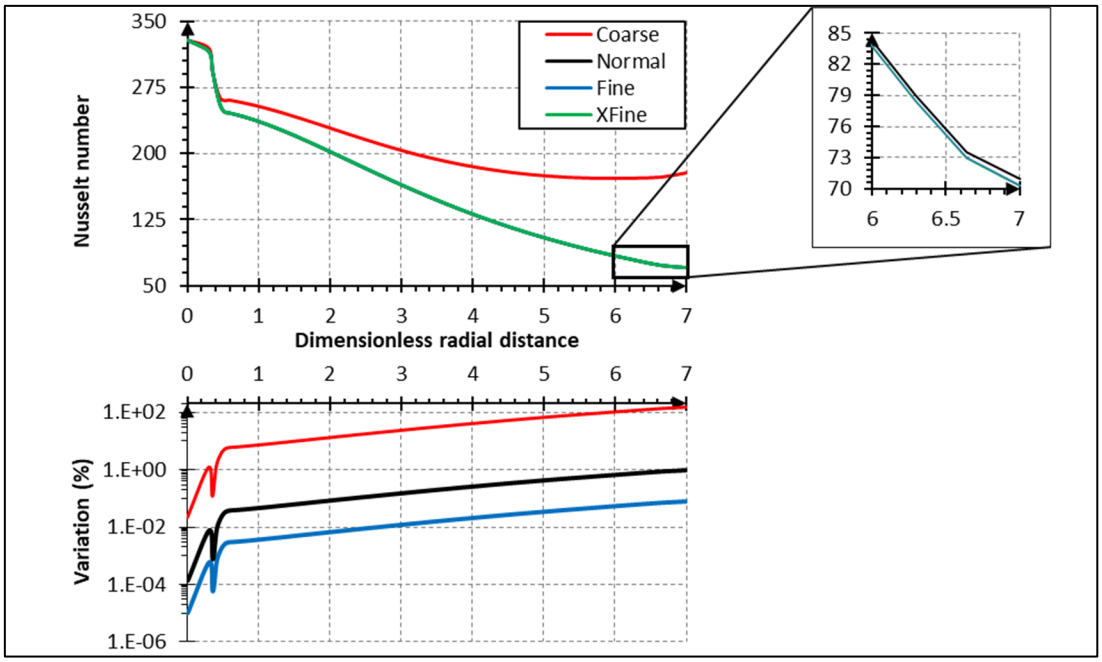

Figure 2.8 Local Nusselt number of the pseudo-steady state regime distributions and variation for different meshes

Figure 2.9 shows the local Nusselt number coefficient of variation in the pseudo-steady state regime. The largest variation is around $(r < D/2)$, where the spray penetrates the film region, then it decreases while departing from the stagnation zone. This could be explained by a homogenization of the film outside of the stagnation zone; film liquid droplets accumulate to form a less turbulent flow. The coefficient of variation for the non-coarse

meshes at r = 7D ($\simeq 0.84\%$) shows that the temporal evolution of the heat transfer is almost stabilised. For the coarse mesh, the derivative of the coefficient of variation with respect to the radial position becomes positive at r = 6, which could be due to a discretization error, given the large cell size.

This mesh size is considered as a very coarse mesh for numerical models using the volume of fluid approach. Edin and Šefko (2015) used $2.1e^5$ cells for a two-dimensional control volume (3.7D×12D) with the same software. Having a large cell size (compared to Eulerian methods) that limits the discretization error to less than 1% makes computations on a large computation domain (characteristic of the aircraft ground deicing process) possible, with a reasonable computing cost.

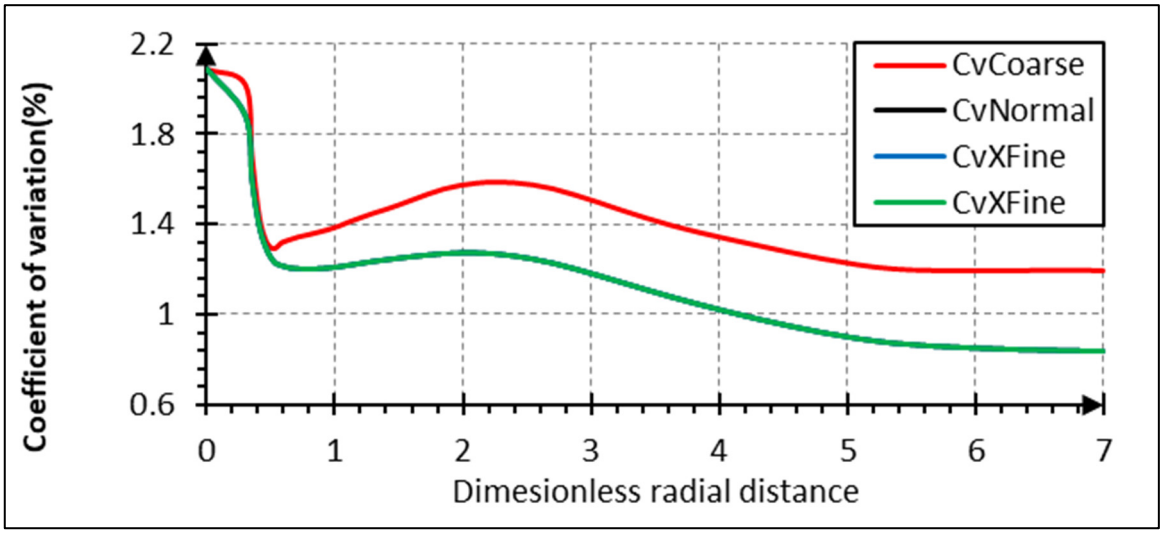

Figure 2.9 Coefficient of variation of the local Nusselt number for different meshes (at pseudo-steady state regime)

2.6.2 Effect of spray parameter

The spray cloud class implemented in OpenFOAM allows the user to set the mass flow rate $\dot{M}$, the particle's diameter distribution, the particle rate (the number of injected particles per second) $\dot{N}_p$, the particle inlet velocity U_p, and the break-up and atomization models. In the pre-processing phase, a constraint is added to ensure a physical inlet condition.

In this subsection, the effects of the particle inlet velocity (Reynolds number $\mathrm{Re_D} = \mathrm{U_p D}/\nu$), the mass flow rate and the particle rate are investigated. The Rosin-Rammler distribution implemented in OpenFOAM enables setting the particle diameter range. The particle diameter $\mathrm{d_P}$ is calculated with equation (2.26) using 4 parameters: $\mathrm{d_{min}}, \mathrm{d_{max}}$ and $\mathrm{d_{mean}}$, respectively the minimum, the maximum and the mean particle diameter to be injected, and n, a distribution parameter.

$$\mathrm{d_P} = \mathrm{d_{min}} + \mathrm{d_{mean}} \times \left[-\ln\left(1 - \Gamma(0,1) \times \left(1 - \mathrm{e}^{-\left(\frac{\mathrm{d_{max}} - \mathrm{d_{min}}}{\mathrm{d_{mean}}}\right)^{\mathrm{n}}} \right) \right) \right]^{1/\mathrm{n}} \tag{2.26}$$

where $\Gamma(0,1)$ is the uniform distribution.

The inlet constraint used in this study is presented in equations (2.27) and (2.28). First, based on the particle sizes, the particle mean mass is computed using a primary number of particles noted here $\mathrm{n_{Data}}$. $\mathrm{n_{Data}}$ should be big enough to let $\mathrm{m_{P.mean}}$ converge. In this study, $\mathrm{n_{Data}} = 2 \times 10^4$ was used after testing several values.

$$\mathrm{m_{P.mean}} = \frac{1}{\mathrm{n_{Data}}} \times \rho_\mathrm{P} \frac{\pi}{6} \sum_{\mathrm{i}=1}^{\mathrm{n_{Data}}} \mathrm{d_p^3} \tag{2.27}$$

$$\mathrm{N_p} = \frac{\mathrm{M}}{\mathrm{m_{P.mean}}} \tag{2.28}$$

With this constraint, it is impossible to vary $\dot{\mathrm{M}}, \dot{\mathrm{N}}_\mathrm{P}$ and equation (2.23) parameters freely. Another constraint (equation (2.26)) on the equation's (2.23) parameters is added for this study. With this constraint, a change in $\mathrm{d_{min}}$ value will modify the whole particle distribution.

$$\mathrm{d_{max}} = 8 \cdot \mathrm{d_{min}} = \frac{9}{2} \cdot \mathrm{d_{mean}} \quad ; \quad n = 3 \tag{2.29}$$

Figure 2.10 shows a histogram of the injected particle diameter distribution using a minimum particle diameter of 1mm. A discretization of 0.5mm was performed on the abscissa axis, making the figure readable.

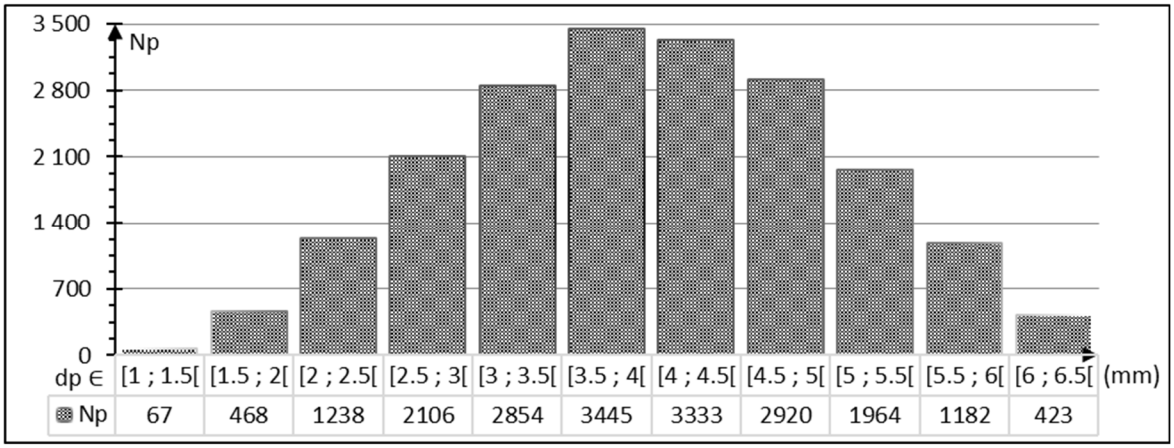

Figure 2.10 Histogram of particle diameter distribution ($n_{Data} = 2 \times 10^4$)

The spray inlet conditions for different configuration are summarised in Table 2.3: 4 Reynolds number values $\left(Re_{i(i\in[\![1,4]\!])}\right)$, 4 particle number rate values $\left(\dot{N}p_{i(i\in[\![1,4]\!])}\right)$ and 4 mass flow rate values $\left(\dot{M}_{i(i\in[\![1,4]\!])}\right)$.

Figure 2.11 presents the local Nusselt number and its coefficient of variation in the pseudo-steady-state regime for the different configurations above. The top line graphs study the Reynolds number effect. The middle line graphs study the particle number rate effect, and the bottom-line graphs study the mass flow rate effect. For a spray, contrary to the continuous jet, the Reynolds number can be increased while keeping the same mass flow rate. The Nusselt number distributions corresponding to a Reynolds number between 10,557 and 63,342 are almost identical (a maximum 4.5% difference at the stagnation zone level). The Nusselt number distribution corresponding to a Reynolds Number of 105,570 is higher.

Table 2.3 Spray inlet conditions for different cases

Configuration	$\mathbf{Re_D}$	$\mathbf{d_{min}(m)}$	$\dot{\mathbf{M}}\mathbf{(kg/s)}$	$\dot{\mathbf{N}}\mathbf{p\ (particles/s)}$
Re_1	10.5e3	1.00e-3	4.00e-2	1.00e6
Re_2	21.1e3	1.00e-3	4.00e-2	1.00e6
Re_3	63.3e3	1.00e-3	4.00e-2	1.00e6
Re_4	105e3	1.00e-3	4.00e-2	1.00e6
$\dot{N}p_1$	21.1e3	2.00e-3	4.00e-2	0.13e6
$\dot{N}p_2$	21.1e3	1.00e-3	4.00e-2	1.00e6
$\dot{N}p_3$	21.1e3	0.50e-3	4.00e-2	8.00e6
$\dot{N}p_4$	21.1e3	0.25e-3	4.00e-2	64.0e6
$\dot{M}_1$	21.1e3	9.11e-4	3.00e-2	1.00e6
$\dot{M}_2$	21.1e3	1.00e-3	4.00e-2	1.00e6
$\dot{M}_3$	21.1e3	1.08e-3	5.00e-2	1.00e6
$\dot{M}_4$	21.1e3	1.15e-3	6.00e-2	1.00e6

This can be explained by the fact that the high velocity of the injected spray has brought more momentum to the wall film, thus increasing the film velocity. The turbulent heat transfer correlation, equation 2.17, is therefore used instead of equation 2.16 at the interface between the internal field and the wall film region.

The coefficient of variation increases because the same number of particles is injected while increasing the inlet velocity; this increases the time interval that separates two particles

impacting the wall successively. Conversely, increasing the particle number rate will reduce this separating time interval. This hypothesis is confirmed by the coefficient of variation reduction with the reduced particle number rate $\left(\dot{N}p_{i(i\in[\![1,4]\!])}\right)$.

Experimentally, increasing the Reynolds number has the effect of increasing the heat transfer (Stevens & Webb, 1991). The same effect can be observed by increasing the mass flow rate and the particle number rate. Having the same particle number and increasing the mass confined in each particle leads to a greater heat transfer variation between time steps of the pseudo-steady state regime. This is shown by the coefficient of variation evolution with the mass flow rate $\left(\dot{M}_{i(i\in[\![1,4]\!])}\right)$. Increasing the spray mass flow rate increases the momentum transferred to the film. However, spraying the same mass with the same inlet velocity while decreasing the droplet size will increase the film momentum, and then, the heat transfer. This observation should be further investigated in order to optimize the aircraft's de-icing process because with the same amount of energy (temperature, mass, inlet velocity), ice can be removed faster.

In all the presented results, the Nusselt number distributions show maximum values in the stagnation zone, followed by an inflection point at $r \simeq D/2$. The same morphology can be observed in many experimental studies (Webb & Ma, 1995), but the inflection point occurs farther downstream on the wall film ($r \simeq 2D$). This difference could be due to the convective heat transfer coefficient models situated between the wall film region and the internal field.

The model implemented in OpenFOAM is more adapted to the prediction of an average global Nusselt number because the characteristic length L is independent of the radial distance from the stagnation point. This motivates the development of new correlations of the local heat transfer coefficient that take into account the radial distance. For the verification of the two-region model, the equations already implemented in OpenFOAM are deemed sufficient.

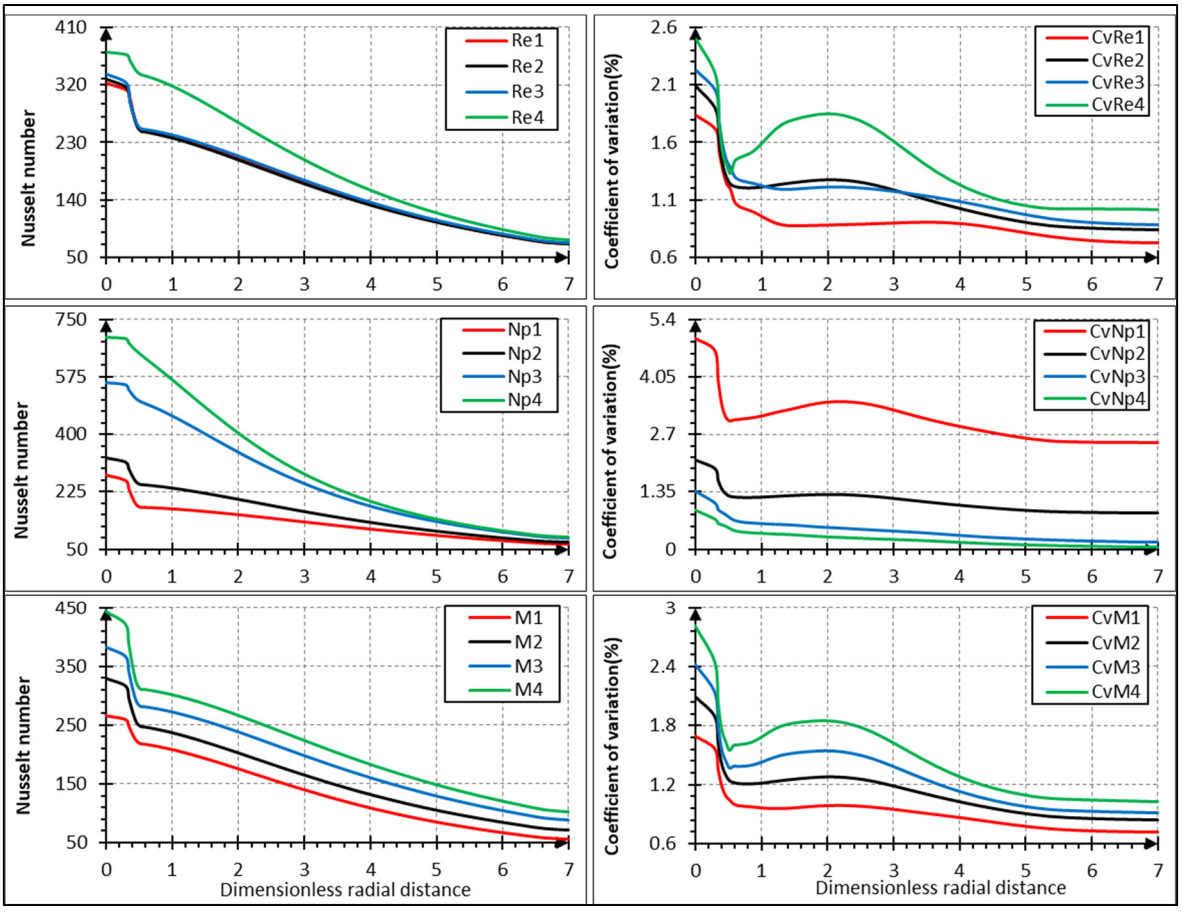

Figure 2.11 Time-averaged local Nusselt number distribution and coefficient of variation for different spray's inlet condition

2.6.3 Spray penetration

To validate the spray model prior to impact, the spray penetration is studied under non-evaporating chamber conditions. Experimental validation data were taken from Mitroglou et al. (2006). In their experiments, the spray characteristics of a 6-hole injector for a direct-injection gasoline engine were investigated with iso-octane fuel. The methodology used here is inspired from Wang, Ge and Reitz (2010). It consists of a mesh-dependency study of spray tip penetration for 4 injection pressure cases. Details of the case setup are summarised in the table below.

Table 2.4 Case setup

Fuel type	Iso-octane
Nozzle diameter	140 μm
Injection pressure (Pin)	120 bar, 200 bar
Injection duration	1.5 ms
Injection fuel amount	8.08mg for 120 bar injection, 10mg for 200 bar (Wang, Ge and Reitz, 2010)
Chamber gas	Not mentioned, supposed to be N_2 (Wang, Ge and Reitz, 2010)
Chamber pressure (Pb)	1 bar and 12 bar
Bore × stroke	139.7 × 152.4 mm

Three mesh sizes were tested, and details are presented in Table 2.5. Figure 2.12 shows the spray penetration for the three meshes and the experimental results for the four injection cases. Results show a relatively good agreement with experimental results. Numerical results for spray penetration are almost linear in the four cases. For the two cases where the chamber pressure (Pb) is 12 bar, experimental results are parabolic, with a discrepancy error of 20% (Pin=200 bar) and 17% (Pin=120 bar). The numerical model behaves better in the case where the chamber pressure is 1 bar and presents an error around 10%. In the ground deicing process, the spray is injected in a domain with open boundaries and the equivalent chamber pressure is around 1 bar. Consequently, these results are quite satisfactory at this stage.

Table 2.5 Characteristics of different meshes

	Mesh 1	Mesh 2	Mesh 3
n_r	10	20	40
n_φ	20	40	80
n_z	20	40	80
n_{tot}	4.00×10^3	3.20×10^4	2.56×10^5

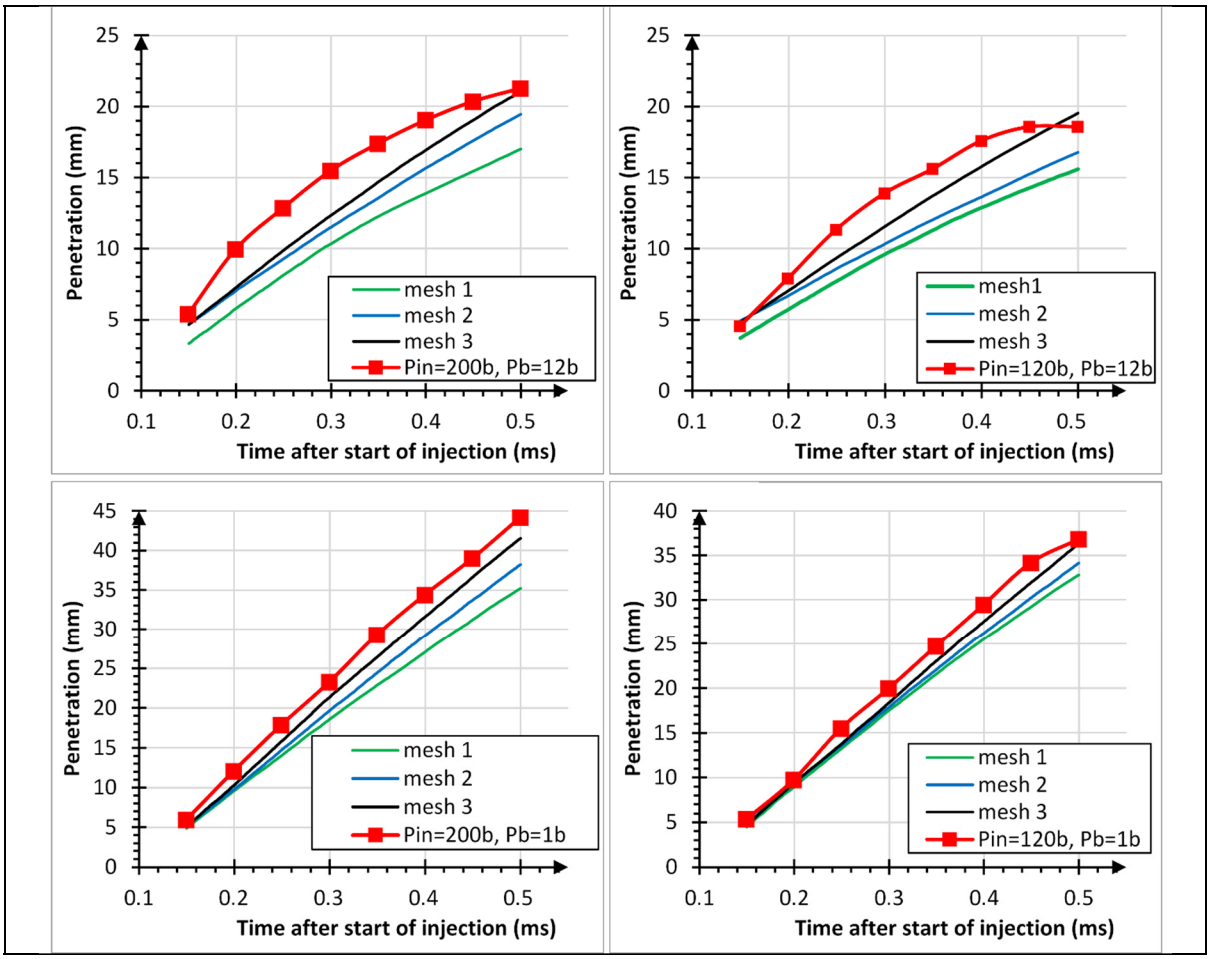

Figure 2.12 Mesh dependency of liquid penetration compared to experimental results; Left: Pin=200 bar, right: Pin=120 bar, top: Pb=12 bar, bottom: Pb=1 bar

2.6.4 Heat transfer on flat plate validation

The lack of experimental data relating to heat transfer of an impinging spray on a wall increases the difficulty carrying out a validation. The variation of the heat transfer in this model is sensitive to the momentum transferred to the wall film region. However, keeping the inlet velocity and the mass flow rate constant and modifying the particle number rate while respecting the inlet constraint presented in equations 15 and 16 allows changing the shape of the Nusselt number distribution. On the other hand, Stevens and Webb (1991) investigate the heat transfer caused by the impingement of a continuous jet on a flat plate. In this study, a Reynolds number based on the volume flow rate $\dot{V}$ is suggested $\left(Re_{\dot{V}} =\right.$

$4\dot{V}/\pi Dv\big)$. This definition of the Reynolds number is adapted to the present model as the heat transfer distribution is more sensitive to the volume flow rate than is the inlet velocity. It has been demonstrated in this experimental study that the variation of $Re_{\dot{V}}$ only affects the magnitude of the Nusselt number, i.e., the Nusselt number at the stagnation point (equation (2.28):

$$\mathrm{Nu_D(r=0)} = \mathrm{A}\cdot \mathrm{Re}_{\dot{\mathrm{V}}}^{\mathrm{q}} \cdot (\mathrm{H/D})^{\mathrm{s}} \cdot (\mathrm{Pr})^{0.4} \tag{2.30}$$

where A, q and s are correlation parameters depending on the nozzle diameter.

The Reynolds number $Re_{\dot{V}}$ has no effect on the normalised Nusselt number distribution $\mathrm{Nu_D(r)/Nu_D}(r=0)$. Figure 2.13 presents the experimental results for a nozzle of diameter D=8.9mm against the numerical results presenting the effect of particle number already presented in Figure 2.11. The discrepancies between the experimental and the numerical results decrease with the particle number rate. The inflection point $(\mathrm{r = D/2})$ in the numerical results disappears for a particle number rate of $3\mathrm{E}^6$. A maximum error of 22% was noted for $\dot{\mathrm{N}}\mathrm{p} = 64\mathrm{e}^6 \mathrm{particles/s}$. The experimental setup being characterized by an 8% acquisition error, leaves only 14% of error attributable to the difference between the diameter of the nozzles, the distance between the nozzle, and the wall and the particle number rate.

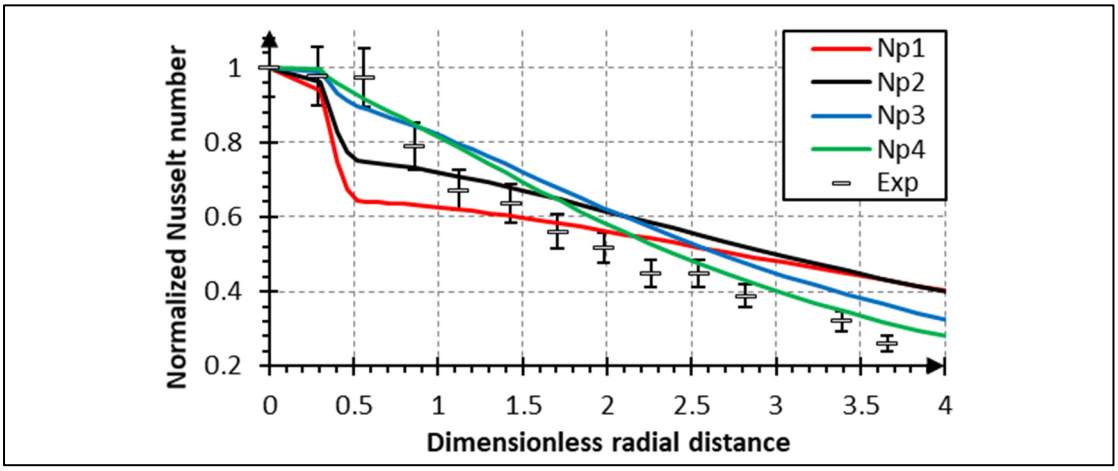

Figure 2.13 Normalised local Nusselt number distribution (simulation vs experiments)

This comparison indicates that raising the particle number rate approximates the normalised Nusselt number to that of a continuous jet. This result is important, considering the present state of art, where there is a lack of experimental investigations of the heat transfer of a spray versus many experimental investigations of the heat transfer of a continuous jet. It then provides a method for the validation of numerical models of the same nature as the presented model.

2.7 Results and discussion

Inclination angles were studied considering three different angles ($30°, 45°,$ and $60°$,) with the initial and boundary conditions stated in the previous section. The results were compared with the vertical spray. Figure 2.14 shows the streamlines formed due to the drag force exerted by the gas in the internal field on particles. These streamlines are coloured with particles. The left part of the figure shows that the wall film is warmer in the direction to which the spray is oriented.

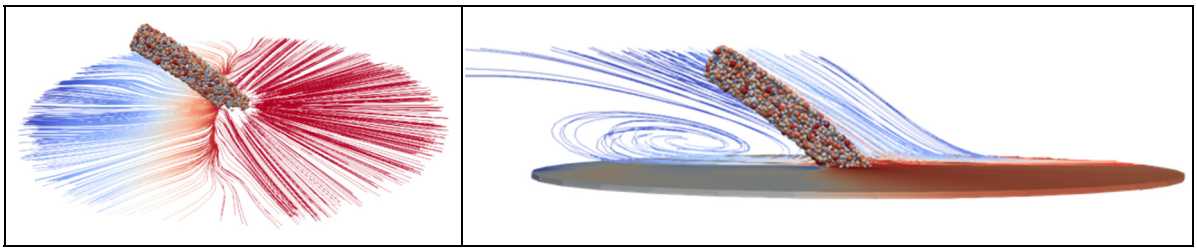

Figure 2.14 Streamlines of the internal field (θ=30°)

Figure 2.15 presents the mapped Nusselt number of the pseudo-steady state regime. The mapped Nusselt number characterises the convective heat transfer locally between the liquid film and the wall. The curve set on the left shows the radial distribution of the convective heat transfer in the direction to which the spray is inclined. The curve set on the right shows the angular variation of the mapped Nusselt number at a fixed distance from the stagnation zone (r = 3D). The function $\widetilde{\mathrm{Nu}}_{\mathrm{D}}(r=3,\varphi,t)\times\sin(\varphi)=f\left(\widetilde{\mathrm{Nu}}_{\mathrm{D}}(r=3,\varphi,t)\times\cos(\varphi)\right)$ is drawn for different inclination angles, i.e. the axes of the second graph are $\widetilde{\mathrm{Nu}}_{\mathrm{D}}(r=$

$3, \varphi, t) \times \cos(\varphi)$ for the horizontal axis and $\widetilde{\mathrm{Nu}}_{\mathrm{D}}(r = 3, \varphi, t) \times \sin(\varphi)$ for the vertical axis. The legend presented is valid for both graphs.

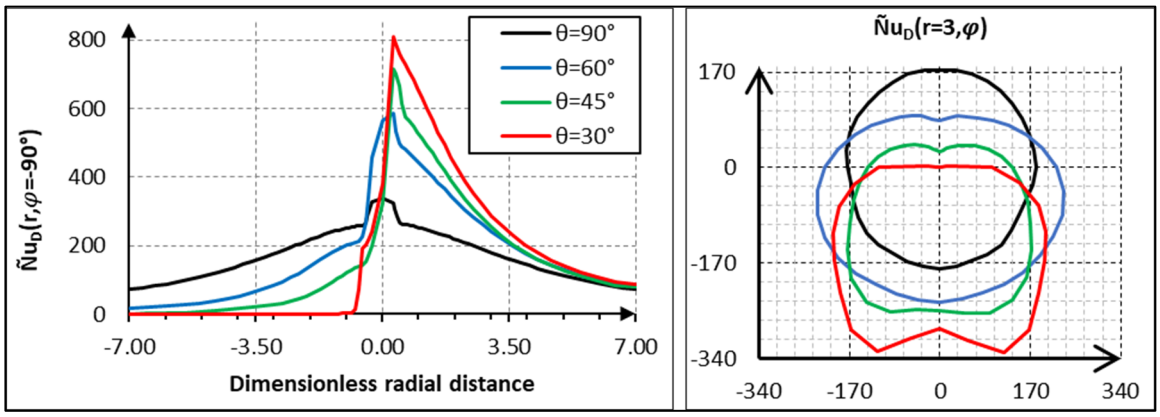

Figure 2.15 Mapped Nusselt number of the pseudo-steady state regime for different sprays' inclination angles

For the vertical jet, the heat distribution is axisymmetric, as shown by the symmetric curve $(\theta = 90°)$ for the radial distribution and by a circle for the angular distribution. The more the spray is tilted, the more this symmetry is lost. The $30°$ inclined spray gives a Nusselt number near zero at a distance $r = D$ and in the direction of $\varphi = 90°$, and presents the higher Nusselt number at $\varphi = -90°$. Globally, for the same inlet conditions, the inclination angle increases the maximum Nusselt number by increasing the momentum transferred to the film (locally), and so, it may be more effective to use an inclined spray for a deicing process.

Good ground deicing practice requires avoiding spraying jets perpendicular to a surface to avoid damage to the latter. The CFD model shows that decreasing the inclination angle increases heat transfer, thus potentially accelerating ice melting. The results show that the proposed CFD model can predict the convective heat transfer in the deicing process. Such predictions can help better understand the effect of spray parameters and eventually help reduce ADF volumes used in airports. These results encourage more research effort to develop CFD models dedicated to the aircraft ground deicing simulation. No definitive conclusion can be drawn before the ice region and ice melting are taken into account in the CFD model. Nonetheless, ice is also fragilized by the effect of pressure, but normal pressure decreases with the inclination angle. Parametric studies of the spray, in the context of

deicing, should be based on the heat transfer, as well as on the stress tensor transmitted to the ice. The model must then be improved to consider this interaction. To conclude, the table below summarises the characteristic parameters of the process, the parameters investigated with the proposed model, and indicates whether or not they are critical.

Table 2.6 Investigated parameters

Parameter	Investigated values	Critical
Nozzle diameter	Not investigated	-
Nozzle-surface distance	Not investigated	-
Inclination angle	30°, 45°, 60° and 90°	Yes
Reynolds number	10.5e3, 21.1e3, 63.3e3 and 105e3	No significant effect in the range 10e3 to 63e3
Mass rate	3e-2, 4e-2, 5e-2 and 6e-2	Yes

2.8 Conclusion

This paper proposes a Eulerian-Lagrangian model that limits the computing costs of scale dispersion problems and enables the investigation by CFD of the influence of an impinging particle spray's parameters on the surface heat transfer. A first region, called the internal field, where particles evolve, cool and evaporate, and a wall film region, where a thin film is formed, both make up the multi-region model. The model is solved within standards libraries of OpenFOAM V6. The domain grid choice is verified. Qualitatively, the model makes good predictions of the effect of the Reynolds number, the particle number rate and the mass flow rate. The spray can be approximated to a continuous liquid jet by increasing the particle number rate, allowing the validation of the model compared to the experimental studies available. For a spray injection at a pressure of 1 bar, the discrepancies between CFD and experimental results for spray penetrations are below 10%.

Future works will focus on editing the boundary conditions between the internal field and the wall field regions, on validations, and then on adding a third region where ice melt will be

modelled. An objective function should also be designed to link heat transfer and surface pressure. A high value for this function must mean good ice decontamination. Such an objective function could serve as a more appropriate basis for comparing deicing scenarios than the Nusselt number. Ice modelling is also mandatory to confirm the present results obtained without ice melting models. The ice shape evolution while melting can indeed affect the liquid film spreading. From a thermal point of view, ice melting cool down the water film. From a geometric point of view, the angle between the spray axis and the ice surface varies with the ice melting, therefore changing the film thickness distribution.

CHAPITRE 3

CFD MODEL FOR AIRCRAFT GROUND DEICING: VERIFICATION AND VALIDATION OF AN EXTENDED ENTHALPY-POROSITY TECHNIQUE IN PARTICULATE TWO PHASE FLOWS

Sami Ernez [a], François Morency [b]

[a,b] Department of mechanical engineering, École de Technologie Supérieure,
1100 Notre-Dame Ouest, Montréal, Québec, Canada H3C 1K3

Article published in « Fluids »,
June 2021

3.1 Abstract

Researchers have focused in the last five years on modelling the aircraft ground deicing process using CFD (computational fluid dynamics) in order to reduce its costs and pollution. As preliminary efforts, those studies did not model the ice melting nor the diffusion between deicing fluids and water resulting from the melting process. This paper proposes a CFD method to simulate this process filling these gaps. A particulate two-phase flow approach is used to model the spray impact on ice near the contaminated surface. Ice melting is modelled using an extended version of the enthalpy-porosity technique. The water resulting from the melting process is diffused into the deicing fluid forming a single-phase film. This paper presents a new model of the process. The model is verified and validated through three steps. (i) verification of the species transport. (ii) validation of the transient temperature field of a mixture. (iii) validation of the convective heat transfer of an impinging spray. The permeability coefficient of the enthalpy-porosity technique is then calibrated. The proposed model proved to be a suitable candidate for a parametric study of the aircraft ground deicing process. On the validation test cases, the precision of heat transfer pre-diction exceeds 88%. The model has the ability of predicting the deicing time and the deicing fluid quantities needed to decontaminate a surface.

Keywords: aircraft ground deicing; particulate two-phase flows; impinging jet; ice melting; convective heat transfer; species diffusion; extended enthalpy-porosity technique; CFD V&V

3.2 Introduction

Several researches have focused on the development of CFD models for deicing aircraft in flight to help in the design of ice protection system (Al-Khalil & Potapczuk, 1993 ; H.-T. Liu & Hua, 2004 ; Morency, Tezok, & Parashivoiu, 2000). On the ground, aircrafts also undergo icing phenomenon. This phenomenon caused several accidents (Moshansky, 1992 ; National Transportation Safety Board, 1993), because of which the aircraft ground deicing was designed and imposed. The aircraft ground deicing process used at most airports is carried out using an impinging spray. Process guidelines are suggested in (ACRP Fact Sheets, 2016 ; ICAO, 2018b, 2018a ; Transport Canada, 2005) based on technical and manufacturer reports, guidance materials and standards and technology patents and procedures. Considering the criticality of the process, the safety is prioritized over economic aspects. Therefore, the guidelines focus more on the results than on how to achieve them. SAE AS 6285 (SAE, 2021) provides industry standards for the methods and procedures used in performing the treatments necessary for the proper deicing and anti-icing of aircraft on the ground. AS6285 forms with AS6286 and AS6332 the “global aircraft deicing standards”. The revised version AS6285D includes references to the Federal Aviation Administration (FAA) and Transport Canada (TC) deicing program guidance. The suggested procedures give general guidance such as to start the deicing at the top for the vertical surfaces or the direction of the spray shall be from the wings leading edge to the trailing edge. The inclination angle between the spray direction and the surface normal is not mentioned. However, numerous experimental studies (Chen et al., 2016 ; Visaria & Mudawar, 2008 ; Yaqing Wang, Liu, Liu, Xu, & Chen, 2010 ; Yan et al., 2013) have shown that variation in spray parameters, such as the inclination angle and the distance, influences the heat transfer between the spray and a wall. Thus, the investigation of those parameters could lead to a more effective procedure.

The lack of an optimal deicing scenario causes financial and environmental losses (Transport Canada, 2005). Some research efforts have recently focused on the numerical simulation of the process. (Chen et al., 2016) validated an analytical correlation between the ice thickness and ADF (Aircraft Deicing Fluids) temperature. It shows the significant effect of the flow

rate, the initial temperature and the injection time of the deicing fluids on the deicing process. Yakhya et al. (2019) were the first to be intesrested in CFD for the simulation of the process. They investigate transient effects of ADF jets using a VOF model (Volume Of Fluid) coupled to a fluid film model implemented in Star-CCM+. Reference (Ernez & Morency, 2019c) replaced the VOF model by a Lagrangian model, more appropriate to flow dispersion using OpenFOAM. Previous CFD studies did not model ice melting nor diffusion between ADF and water resulting from the melting process. This paper proposes a CFD method to simulate the AGD (Aircraft Ground Deicing) that fills these gaps.

Melting phenomenon can be divided into two categories according to the heat transfer mode:

Convection fusion (natural or forced): It occurs if a solid is placed in a fluid domain with certain pressure and temperature fields. In natural convection, no flow is imposed, the pressure or / and temperature gradients generated at the solid-fluid interface induces the movement. This movement prevents the solid from having a cold layer of fluid around it. This movement persists until a point of equilibrium is reached by melting the solid (Bertrand et al., 1999). In forced convection, the flow lowers the pressure and / or increases the temperature at the solid-fluid interface, causing it to melt (Ma et al., 2010).

Close Contact Fusion: It occurs if a heat source and a solid are brought into contact with each other during the solid fusion. The physical situation involves the movement of the heat source or the solid, which prevents the accumulation of the melt between the source and the solid (Groulx & Lacroix, 2006).

The ice melting in AGD process occurs because of the spreading of an ADFs film. The film is induced by the spray flow; therefore, this process involves forced convection. From a numerical point of view, numerical methods modelling convection fusion can be divided into two families: (i) The multi-region methods (Tan et al., 2007) consists in defining two regions in which two systems of different equations are solved. A dynamic mesh is used to track the melting front, (ii) The single region methods (Voller & Prakash, 1987) consist of using a single region and defining a scalar field, modelling the liquid/solid volume fraction in each cell. Source terms are added to the conservation equations to model the ice presence effect on

the flow. The liquid/solid volume fraction is updated at each time-step, according to the energy transfer and a threshold temperature. In this method, a single region is sufficient, hence a static mesh is used, which makes it more interesting in the AGD process.

Indeed, the AGD process is characterized by a large dispersion of the geometric length scales. (Ernez & Morency, 2019c) opted for a particulate two-phase flow to lower the computations needs in term of mesh refinement. They validated the convective heat transfer of an impinging spray on a flat plate. This paper suggests coupling a solidification/melting model to a particulate two phase flow. The single region method is selected for this task due to its simplicity of implementation. It consists of adding (i) a solid fraction field that is updated at each iteration based on the temperature field and (ii) the adequate source terms to the governing equations. The enthalpy-porosity technique (Voller & Prakash, 1987) is used in this paper in a Eulerian particulate two-phase flow based on (Rusche, 2002) already implemented in OpenFOAM, more precisely in its native solver $twoPhaseEulerFoam$. The Eulerian approach is favored over the Lagrangian for the fact that the liquid/solid phase fraction used by the melting method is a Eulerian field. Using the Lagrangian method will lead again to the use of a dynamic mesh. Instead, a multi-region approach would be adopted.

Figure 3.1 presents a typical computational domain of the problem. A first region is defined for the liquid spray, where the multiphase flow is treated with a Eulerian-Lagrangian model. The second region relatively thin, is defined for the spray impingement on the ice. The multiphase flow in this region is carried out with a Eulerian-Eulerian model based on (Rusche, 2002) works coupled to the enthalpy-porosity technique to model ice melting. The Lagrangian-Eulerian region is fully described in (Ernez & Morency, 2019c). The present paper focuses on the verification and validation of the Eulerian-Eulerian model where an extended version of the enthalpy-porosity technique is proposed and implemented. The original version of the enthalpy-porosity technique is designed for a liquid-solid system. It is widely used in internal flow simulations, particularly in the context of Phase-Change Material (PCM) for heat storage. In this paper, it is extended to a gas-liquid-solid system. It is also calibrated for a computational domain characteristic of the AGD process. Previous works (Ernez & Morency, 2019c ; Yakhya et al., 2019) presented an impinging spray model

and analyze the convective heat transfer on a clean surface. This paper is a complementary effort to simulate the ice decontamination in the context of a numerical test bench. To the knowledge of the authors, this is the first effort in literature that implements the enthalpy-porosity technique to a gas-liquid-solid system. The extended enthalpy-porosity technique is a new candidate for simulating a variety of problems involving solidification and melting phenomena in external flow.

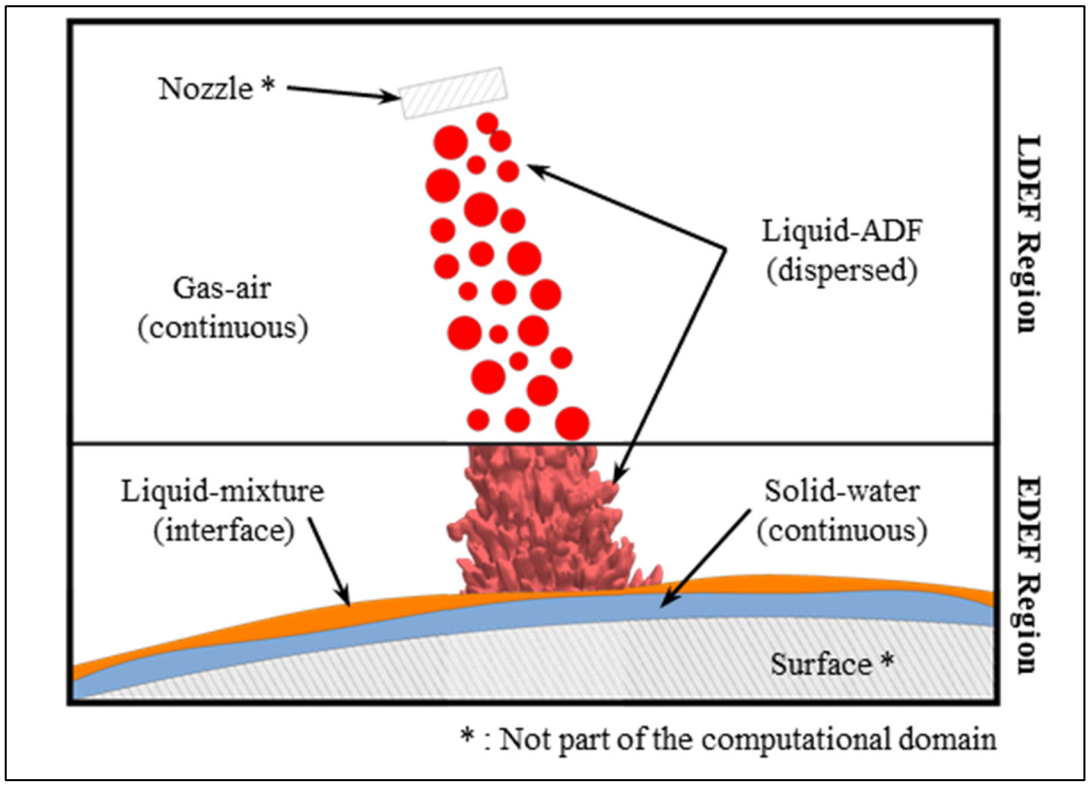

Figure 3.1 Typical computational domain of the proposed methodology

The following section describes the mathematical model and the numerical method of the Eulerian-Eulerian region. The third section presents a sequence of three test cases for the V&V assessment which followed by a calibration of the solidification/melting model.

3.3 Conceptual model

The problem could be seen as the interaction of two phases (gas and liquid). The solid phase is implicitly treated as a liquid phase with a velocity field reduced to zero. The Eulerian-Eulerian region of Figure 3.1 presents a typical computational domain of the problem. Initially, the water is at solid state at an ambient temperature below the melting point. The hotly injected ADF heats the ice and melts it. The liquid water coming out from the melting process dissolves in ADF, forming a mixture. First, the conservation equations are presented. It is followed by the numerical method describing the solver algorithm and the numerical schemes.

3.3.1 Mathematical model

The model consists of continuity, species, momentum, and energy equations. Those equations are designed for a gaseous phase and a liquid phase. To model ADF and water mixing, the liquid phase is considered as a mixture of two liquid species. A specie transport equation is solved just after the continuity equation. The enthalpy-porosity technique is used to model the ice presence in the momentum and energy equations. In the following equations, indices “g” and “l” refer, respectively, to the gas and liquid phases; “s1” and “s2” refer, respectively, to the liquid 1 and liquid 2 species. Below, liquid 1 is set as ADF and liquid 2 is set as water.

3.3.1.1 Mass conservation

The mass conservation (continuity) equation is analogue to the VOF method (Rusche, 2002):

$$\frac{\partial \alpha_i \rho_\mathrm{i}}{\partial \mathrm{t}} + \nabla \cdot (\mathbf{u_i}\, \alpha_i \rho_\mathrm{i}) = 0 \tag{3.1}$$

with α_i, ρ_i, $\mathbf{u_i}$ are, respectively, the volume fraction, density, and velocity of entity i.

Then, the specie transport (Ferziger, Perić, & Street, 2020) equation is solved to update concentrations and the liquid thermophysical properties.

$$\frac{\partial \alpha_l \, \rho_l \, Y_{s1}}{\partial t} + \nabla \cdot (\alpha_l \, \rho_l \, u_l \, Y_{s1}) - \nabla \cdot (\alpha_l \, \rho_l D_l \cdot \nabla \, Y_{s1}) = 0 \tag{3.2}$$

with D_l is the mutual diffusion coefficients of specie 1 and specie 2 defined as: $D_l = \nu_l / Sc_l$ with ν_l and Sc_l the kinematic viscosity and the Schmidt number of the liquid phase. Right after solving Equation (3.2) the liquid phase thermophysical properties are updated using the mixture rules presented in Table 3.1.

Table 3.1 Mixture Rules

Thermophysical Properties	**Expression**
Density	$\rho_l = \sum Y_{si} \cdot \rho_{si}$
Dynamic viscosity	$\mu_l = \sum Y_{si} \cdot \mu_{si}$
Heat capacity	$Cp_l = \frac{\sum Y_{si} \cdot \rho_{si} \cdot Cp_{si}}{\rho_l}$
Thermal diffusivity (for temperature)	$\kappa_l = \sum Y_{si} \cdot \kappa_{si}$

3.3.1.2 Momentum Conservation

After resolving the mass conservation equations, the phases are considered (in each cell) as continuous and dispersed following two threshold values: (i) A_F the minimum volume fraction of a phase to be considered fully continuous and by default the other phase will become a dispersed phase. The dispersed phase is modelled as a set of droplets characterized by a diameter and a shape. For sake of simplicity, the shape of the droplets is considered as a perfect sphere. (ii) A_P the minimum volume fraction of a phase, for which it can be treated as partly continuous phase, i.e., the cell is part of an interface ($A_F > A_p$).

Two momentum equations of the same form are solved for each phase (gaseous and liquid) (Rusche, 2002):

$$\frac{\partial \alpha_i \, \rho_i \, \mathbf{u_i}}{\partial t} + \nabla . (\alpha_i \, \rho_i \, \mathbf{u_i} \, \mathbf{u_i}) = -\alpha_i \nabla p + \alpha_i \, \rho_i \, \mathbf{g} + \nabla \cdot \left(\alpha_i \left(\mu_i D(\mathbf{u_i}) - \frac{2}{3} \mu_i \nabla \cdot \mathbf{u_i} I \right) \right) + \mathbf{S}_{u_i} + \mathbf{S}_{sms,\mathbf{u_i}} \quad (3.3)$$

where μ_I is the viscosity of phase i and the rate of strain (deformation) tensor $D(\mathbf{u_i})$ is defined as $D(\mathbf{u_i}) = \frac{1}{2}(\nabla \mathbf{u_i} + (\nabla \mathbf{u_i})^T)$. $\boldsymbol{S_{sms,u_i}}$ is an added source term modelling the melting/solidification of phase i, it is discussed in subsection 3.3.1.4. $\mathbf{S}_{u_i}$ is the inter-phase momentum transfer with the convention of $\left(\mathbf{S}_{u_g} + \mathbf{S}_{u_l} = 0\right)$. The two phases exchange momentum in form of drag and virtual mass $\left(\mathbf{S}_{u,i} = \mathbf{S}_{drag,i} + \mathbf{S}_{vm,i}\right)$. The drag and virtual mass forces are due, respectively, to the velocity difference and the acceleration difference between the two phases. In the following equations, quantities difference presented by the symbol Δ are defined as: $\Delta\chi = \chi_{other\ phase} - \chi_{phase_i}$.

For cells with dispersed phase (Kolev, 2012):

$$\mathbf{S}_{drag,i} = \frac{3}{4} \alpha_{disp} \cdot \frac{\rho_{cont} \nu_{cont}}{D_{disp}^2} \cdot C_{drag} \cdot Re \cdot \Delta \mathbf{u}$$
$$\mathbf{S}_{vm,i} = C_{vm} \cdot \alpha_{disp} \cdot \rho_{cont} \cdot \frac{D}{Dt}(\Delta \mathbf{u}) \quad (3.4)$$

For interface (Marschall, 2011):

$$\mathbf{S}_{drag,i} = K_{drag} \cdot \Delta \mathbf{u}$$
$$\mathbf{S}_{vm} = 0 \quad (3.5)$$

with C_{drag} and K_{drag} the drag coefficients and A_{disp} the dispersed phase surface. The drag coefficient models implemented in OpenFOAM are presented on Table A1 in (Ernez & Morency, 2021a). Since droplets are supposed to have a spherical shape, the virtual mass coefficient is fixed to 0.5 (Kolev, 2012).

3.3.1.3 Energy conservation

Two energy equations are solved for gaseous and liquid phase (Manni, 2014), as shown by Equation (3.6).

$$\frac{\partial \alpha_i \, \rho_i \, (h_i + k_i)}{\partial t} + \nabla . (\alpha_i \, \rho_i \, (h_i + k_i)\mathbf{u_i}) = \alpha_i \frac{\partial p}{\partial t} + \alpha_i \, \rho_i \, \mathbf{g} \cdot \mathbf{u_i} \; + \nabla \cdot (\alpha_i \, \alpha_{eff} \, \nabla h_i) + K_{ht} \cdot \Delta T \; + S_{sms,h_i} \tag{3.6}$$

with h, k and α_{eff} are, respectively, the enthalpy, the kinetic energy and the effective thermal diffusivity. $S_{sms,h}$ is a sink term modelling phase change. K_{ht} is the heat transfer coefficient between the two phases. Two models are already implemented in OpenFOAM. The first is an analytical model for a perfect sphere and the second is a correlation for turbulent heat transfer also for a sphere. The heat transfer coefficients are presented in Table A2 in (Ernez & Morency, 2021a).

3.3.1.4 Solidification/Melting Source terms

The source terms $\boldsymbol{S}_{sms,u_i}$ and S_{sms,h_i} model the solid phase presence effect. They are calculated following the enthalpy-porosity technique. In this technique, the solid-liquid free boundary is not tracked explicitly. Instead, a phase fraction indicator field δ (0 for solid and 1 for liquid) is updated at each iteration based on an enthalpy balance. Originally, the enthalpy-porosity technique was developed and used for single phase flows, in this paper a modified version of the technique is proposed.

The momentum sink $\boldsymbol{S}_{sms,\boldsymbol{u_i}}$, introduced in equation (3.3), classically models the buoyancy effect $\boldsymbol{S}_{\boldsymbol{buoy}}$ due to the thermal expansion of ice and a drag force $\boldsymbol{S}_{sd}$ exerted by ice on the liquid. However, for the gas phase the buoyancy term should be removed since the implicit solid phase belongs to the liquid phase. Additionally, in the proposed problem, the buoyancy effect for the liquid phase can be neglected since the flow is under forced convection (impinging spray).

$$\boldsymbol{S}_{sms,\boldsymbol{u}} = \boldsymbol{S}_{buoy} + \boldsymbol{S}_{sd} = \boldsymbol{S}_{sd} \tag{3.7}$$

In the original version of the enthalpy-porosity technique (Voller & Prakash, 1987), the solid phase is not designed to move. The present work focusses on the decontamination of a surface, and since no ice breakup is modelled, this characteristic will be preserved.

$$\boldsymbol{S}_{sms,\boldsymbol{u_i}} = \boldsymbol{S}_{sd,i} = S_{sd} \cdot (\boldsymbol{u}_{solid} - \boldsymbol{u}_i) = -\, S_{sd} \cdot \boldsymbol{u}_i \tag{3.8}$$

The Darcy law for flow through porous media is used. For isothermal solidification/melting, permeability has no physical significance; however, it is used classically as a numerical technique to estimate the velocity at the mushy region (Voller & Prakash, 1987).

$$\mathrm{S_{sd}} = \mathrm{Cu} \cdot \frac{\delta^2}{(1-\delta)^3 + \mathrm{q}} \tag{3.9}$$

where q and Cu are model coefficients, which are discussed in the numerical method paragraph.

$$\begin{aligned} \frac{D}{Dt}\left(\alpha_l\, \rho_l\, (h_l + k_l)\right) &= \frac{D}{Dt}\left(\alpha_l\, \rho_l\, \left(h_{l,s} + k_l\right)\right) + \frac{D}{Dt}\left(\alpha_l\, \rho_l\, h_{l,L}\right) \\ &= \alpha_\mathrm{i} \frac{\partial \mathrm{p}}{\partial \mathrm{t}} + \alpha_i\, \rho_\mathrm{i}\, \mathbf{g} \cdot \mathbf{u}_l\ + \nabla \cdot \left(\alpha_i\, \alpha_{eff}\, \nabla \mathrm{h_i}\right) + K_{ht} \cdot \Delta T \end{aligned} \tag{3.10}$$

where $h_l = h_{l,s} + h_{l,L}$, with $h_{l,s} = c_{p,l} \cdot T_l$ is the sensible enthalpy and $h_{l,L} = \delta L$ is the enthalpy of fusion (or latent heat of fusion).

Moving the $\frac{D}{Dt}\left(\alpha_l\, \rho_l\, h_{l,L}\right)$ on the right side of the energy equation and developing it, gives:

$$\begin{aligned} &\frac{D}{Dt}\left(\alpha_l\, \rho_l\, \left(h_{l,s} + k_l\right)\right) \\ &\qquad = \alpha_\mathrm{i} \frac{\partial \mathrm{p}}{\partial \mathrm{t}} + \alpha_i\, \rho_\mathrm{i}\, \mathbf{g} \cdot \mathbf{u}_l\ + \nabla \cdot \left(\alpha_i\, \alpha_{eff}\, \nabla \mathrm{h_i}\right) + K_{ht} \cdot \Delta T\ - L \frac{D}{Dt}(\alpha_l\, \rho_l\, \delta\,) \end{aligned} \tag{3.11}$$

which by identification with Equation (3.6), gives:

$$S_{sms,h_l} = -L\frac{D}{Dt}(\alpha_l\,\rho_l\,\delta\,) \tag{3.12}$$

where S_{sms,h_l} is the energy sink term due to phase change of the liquid phase (solid/liquid). It represents also the latent heat released during solidification. The gaseous phase does not undergo a phase change (the deposition/sublimation phenomenon is not modelled), thus the term S_{sms,h_g} is null.

3.3.2 Numerical methods

This section describes the numerical methods used in all the computations presented in this paper. It is divided into numerical treatment and solution control. The numerical treatment of the particulate two-phase flow solver is fully described in (Manni, 2014). The next paragraph discusses the numerical treatment of the solidification/melting source. It is followed by the numerical schemes and the algorithm controls details for reproducibility purpose.

Numerical treatment

Concerning the Darcy law coefficient presented at the Equation (3.9), q is a small number to prevent division by zero (default 10^{-3}). Cu is the mushy region sink coefficient which measures the amplitude of the damping. It is also known in the literature as the permeability coefficient (Ebrahimi, Kleijn, & Richardson, 2019). The higher this value, the steeper the transition of the velocity of the material to zero as it solidifies. Very large values may cause the solution to oscillate (OpenFOAM default value 10^5). In the liquid region ($\delta = 1$), S_{sd} is equal to zero and does not affect the momentum equation. In the solid region, ($\delta = 0$) S_{sd} is equal to $-Cu/q$ which is high enough to dominate all other terms in the momentum equation. Therefore, the momentum equation will be reduced to $S_d \cdot \boldsymbol{u} = 0$, and, consequently, $\boldsymbol{u} = \mathbf{0}$. Ebrahimi et al. (2019) investigated the sensitivity of numerical predictions to the permeability coefficient Cu. The study revealed that reducing the cell size at the mushy zone (free boundary at the ice vicinity) diminishes the influence of Cu on the

results. According to (Ebrahimi et al., 2019), values between 10^4 and 10^8 are often applied in the modelling of energy storage systems. The Cu value is often tuned for every set of boundary conditions and material properties.

In the case of AGD process, there is a remarkable lack of experiment data. Tuning the permeability coefficient to match numerical results with experimental ones is impossible for the moment. Therefore, the default value of 10^5 is used at first. Once the computation parameters are fixed after a grid convergence study, the sensibility to the permeability coefficient will be studied. If dependencies are revealed, the mesh should be refined. At that state, the permeability coefficient could be tuned for the first mesh selected through the mesh convergence study. Finally, the solid phase fraction is updated at each time step i in every cell n in two steps (Voller & Prakash, 1987):

$$\delta_n^{i+1} = \delta_n^i + r_s \cdot Cp_{l,n} \cdot \frac{T_{sol} - T_n}{L}$$
$$\delta_n^i = \max\left(0, \min\left(1, \delta_n^{i+1}\right)\right) \tag{3.13}$$

with T_{sol} and Cp_l the temperature of the phase change and the heat capacity of the liquid phase and r_s an under-relaxation factor.

Numerical schemes and algorithm controls

Conservation equations are solved using the PIMPLE algorithm of OpenFOAM (Holzmann, 2017); within one time-step, the algorithm searches a steady-state solution with under-relaxation and then go in time. Three outer correction loops are used to ensure that the explicit parts of the equations are converged. After reaching a defined tolerance criterion of $1e^{-6}$ within the steady-state calculation, the algorithm leaves the outer correction loop and moves on in time. Conservation equations are solved using a Gauss Siedel smooth solver, and the pressure is then solved using the geometric algebraic multi-grid (GAMG) solver (Greenshields, 2017) with a diagonal incomplete-Cholesky (DIC) smoother/preconditioner.

OpenFOAM's standard numerical schemes are used to solve the mathematical model. Time derivative terms are computed using an implicit, bounded first-order transient discretization scheme (Greenshields, 2017). Gradient terms are computed using a face-based third-order Gauss scheme, which is based on the Gaussian divergence theorem for the volume integral of a gradient field (Greenshields, 2015). The third order is used to improve the spatial accuracy by reducing the numerical diffusion especially for volume fractions α_i, Y_i and δ. Second-order tensors divergence terms such as divergence terms of the momentum equations are computed using a limited second-order Gauss scheme with a single limiter. The limiter is calculated based on the direction of most rapidly changing gradient. Divergence terms including energy, pressure and specie terms are computed using a limited second-order scheme that limits towards upwind in regions of rapidly changing gradient. Divergence terms including only phase fractions are discretized using the Van Leer divergence scheme. Finally, Laplacian terms are discretized using an uncorrected second-order Gauss scheme.

3.4 Verification, Validation and Calibration

In this section, three test cases are set for the V&V assessment of the mathematical model and the numerical method. The first test case is a simple diffusion test between two liquids. The results are compared to the ones computed with the native solver $laplacianFoam$. The second test case is for the validation of the computed temperature of a mixture. The results are compared to the experimental results published in (Rodríguez-Ocampo et al., 2020). The third test case is a validation of the convective heat transfer of an impinging hot spray on a flat plate (Stevens, 1988). At the end, the permeability coefficient is calibrated for an AGD test case.

3.4.1 Diffusion verification test

The goal of this test is to verify the code consistency. This is done by reducing the problem to a simple diffusion case. The results can then be validated against results from the $laplacianFoam$ solver. $laplacianFoam$ resolves a simple heat equation and was validated in several works (Hermosilla, 2016 ; Mironova, 2018 ; Noriega, 2016).

The problem is reduced to a simple diffusion case by setting adequate initial and boundary conditions. Initially, the computational domain is filled completely by a liquid phase with uniform temperature and pressure, and a zero velocity. The thermophysical properties of the two species composing the liquid are identical to avoid buoyancy effect due to density gradients or variation of the diffusion coefficient due to viscosity gradients. The solidification melting source is deactivated for this test.

The control volume, presented in Figure 3.2, is a 2D square of 1 m edge with wall boundaries on its four sides. Initially, the species compose a disc shape at the center of the control volume with an inner diameter of 0.3 m and an outer diameter of 0.6 m. This form is characteristic of what could be resulting from an impinging spray. Finally, the boundary field value for the ADF specie is set as a uniform constant equal to 1 to let the water species dissipate across the walls.

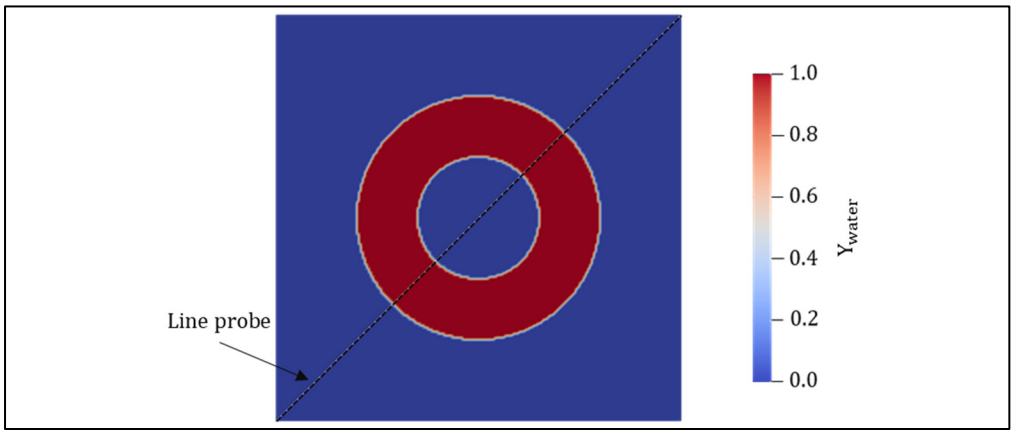

Figure 3.2 Species distribution at the initial time and probe emplacement

For the *laplacianFoam* case setup, the same mesh is used with similar initial and boundary conditions for the temperature field (conform to the water specie). All computations are done with a mutual diffusion coefficient $D_l = 2 \cdot 10^{-3}\ m^2 \cdot s^{-1}$ giving a Schmidt number $Sc_l = 5 \cdot 10^{-4}$ for a kinematic viscosity of $\nu_l = 1 \cdot 10^{-6}\ m^2 \cdot s^{-1}$. This setup permits to have a maximum volume fraction inferior to 0.1 after 50 s of time. It allows to evaluate the code precision for high and low volume fractions of the species. Twelve tests were performed involving three uniform meshes with different degree of refinement ($50 \times 50, 100 \times$

100 and 200×200 cells) and four different time steps ($10^0, 10^{-1}, 10^{-2}$ and 10^{-3} s). The computational domain is discretized into uniform square cells with constant edge length in both X and Y directions.

For better understanding of the test case, 5 spatial distributions of Y_{water} along the line probe are presented in Figure 3.3 with a dimensionless distance $\mathrm{X} = \mathrm{x}/\sqrt{2}\mathrm{m}$. The finest mesh and the smaller time step were used in this figure. Computations with the other meshes are used to demonstrate the grid convergence. The distribution keeps its symmetry. The integral encompassed by one curve and the x axis decreases over time. At the final time (50 s), the field's gradient $\partial \mathrm{Y_{water}}/\partial \mathrm{X}$ is attenuated, meaning the mixture is more homogeneous. A maximum value less than 0.1 is present at the center of the computational domain.

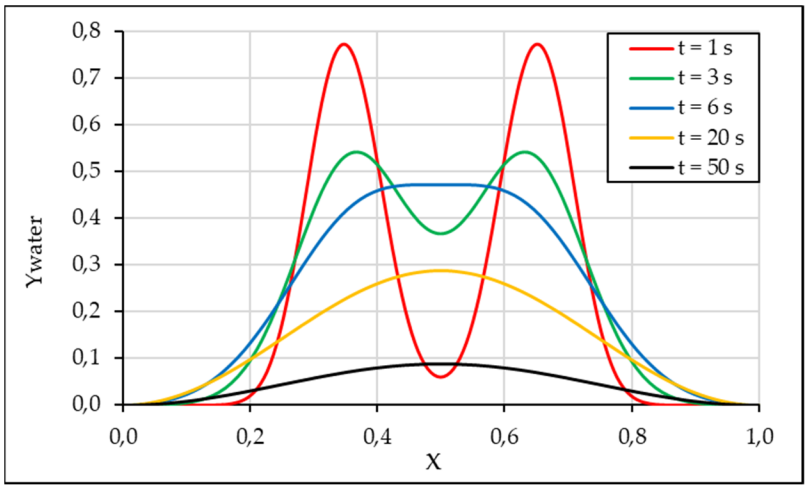

Figure 3.3 Spatial distribution of $\mathrm{Y_{water}}$ at five different times

The verifications are made in two steps. The first step is to generate the reference data. It consists of a time-convergence study followed by a grid-convergence study of the *laplacianFoam* case. For each mesh, the time step induced error is evaluated for each 1s of time following Equation (3.14).

$$\mathrm{E}_{mesh}(\mathrm{dt_i}, \mathrm{t}) = 100 \times \int_{\mathrm{lineProbe}} |\mathrm{Y}_{mesh}(\mathrm{dt_i}, \mathrm{t}) - \mathrm{Y}_{mesh}(\mathrm{dt_{i+1}}, \mathrm{t})| \tag{3.14}$$

where dt designates the time step and t the time. The time step induced error distribution function through time is presented on the Figure 3.4 for the three meshes. For all the computations, the error has the same time evolution. It decreases for the first 10 s then stabilize at a constant value. The time convergences are also quite similar for the three meshes. The constant value of the error decreases from 0.18% for a time step of $1s$ to 0.002% for a time step of $0.01s$.

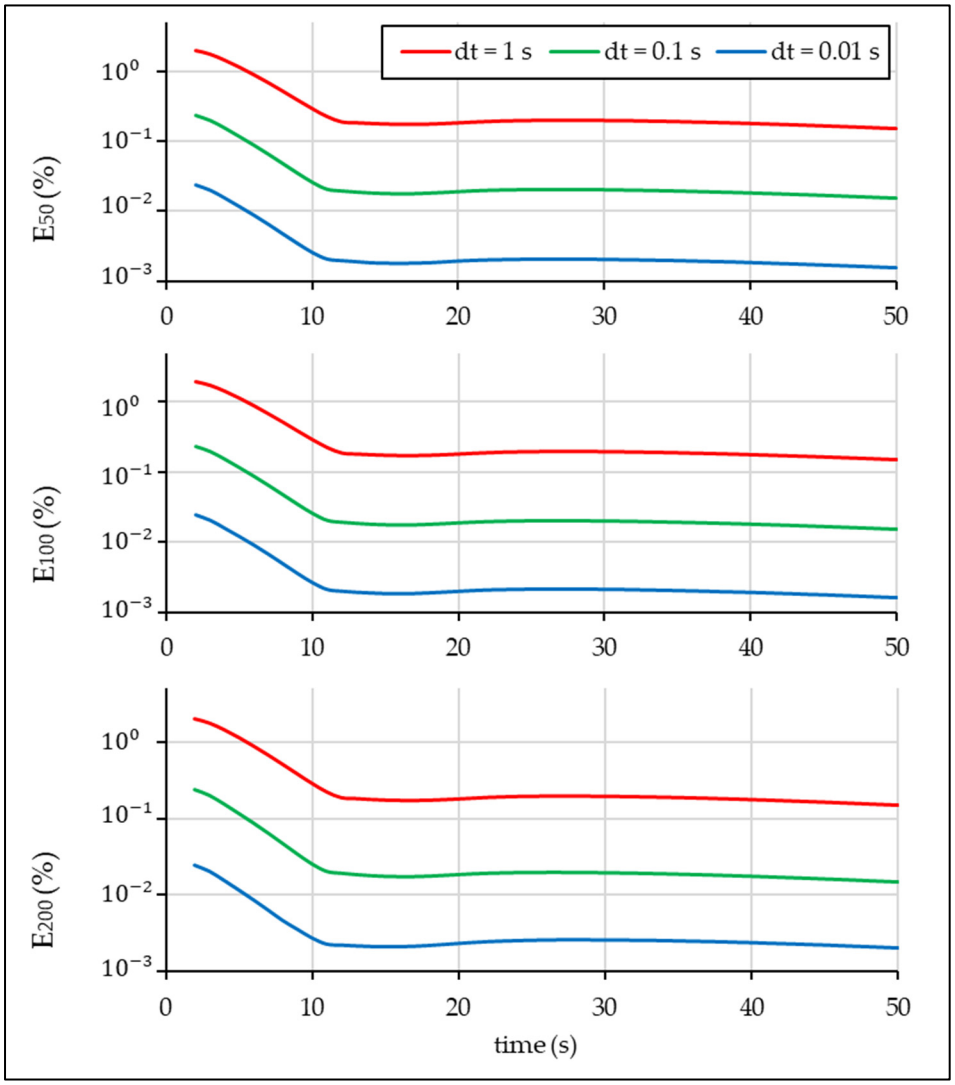

Figure 3.4 Time step induced error distribution for the three meshes

For the grid convergence study, the results for the smallest time steps are used. The grid induced error is evaluated following Equations (3.15) and (3.16).

$$E_{Coarse}(t) = 100 \times \int_{lineProbe} |Y_{Coarse}(t) - Y_{Medium}(t)| \quad (3.15)$$

$$E_{Medium}(t) = 100 \times \int_{lineProbe} |Y_{Medium}(t) - Y_{Fine}(t)| \quad (3.16)$$

Figure 3.5 presents the grid induced error evolution through time. The two errors are similar during the first 8 s. They start at 2% and attain 0.75% after 8 s of time. After 8 s, the relative error between the Coarse mesh and the Medium mesh keeps decreasing progressively until the end of the simulation. The relative error between the Medium mesh and the Fine mesh decreases faster to reach 0.1% at 13 s and stay constant until the end of the simulation. The mean values of the relative errors are 0.61% and 0.34%, respectively, for Coarse-Medium and Medium-Fine meshes.

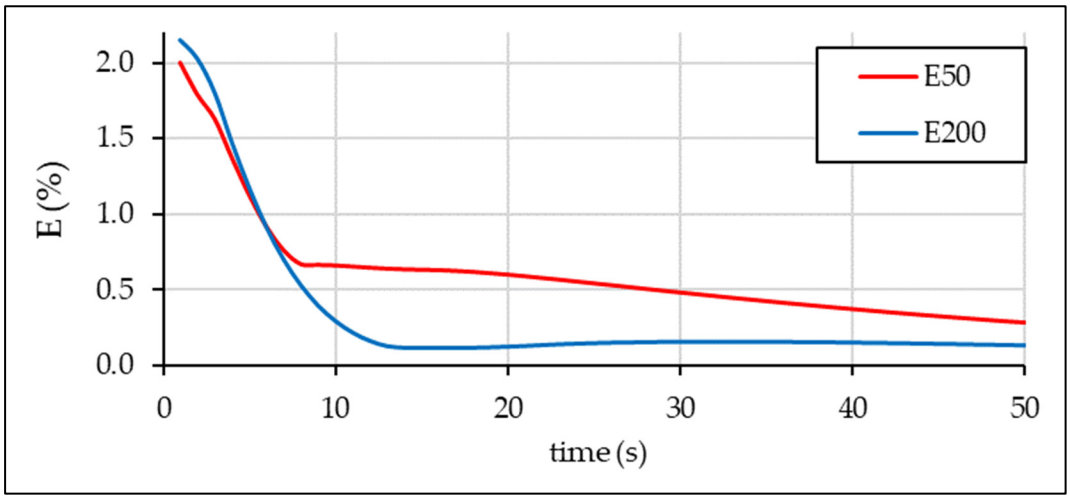

Figure 3.5 Grid induced error evolution

The same calculations are done with the $AGDEulerFoam$. The results' precision is assessed using a relative and an absolute error presented, respectively, by Equations (3.17) and (3.18).

$$E_A(dt, dx, t) = 100 \times \int_{lineProbe} \left|Y_A(dt, dx, t) - Y_{laplacian}(dt, dx, t)\right| \quad (3.17)$$

$$\mathrm{E_{abs}}(\mathrm{dt},\mathrm{dx},\mathrm{t}) = 100 \times \int_{\mathrm{lineProbe}} |\mathrm{Y}_A(\mathrm{dt},\mathrm{dx},\mathrm{t}) - \mathrm{Y_{abs}}(\mathrm{t})| \tag{3.18}$$

with Y_A and $\mathrm{Y_{laplacian}}$, the results of the $AGDEulerFoam$ and the $laplacianFoam$ solvers. $\mathrm{Y_{abs}}$ stands for the results of the $laplacianFoam$ solver with the finest mesh and smallest time step. The maximum and mean values of the errors are presented in Table 3.2.

For all tests, the mean relative error is of the order of $10^{-4}\%$, which shows that the configured solver gives practically the same results as the $laplacianFoam$ solver. The relative error is independent from the time step. Refining the mesh reduces the relative error as seen on the maximum value of the relative error. The analysis of the absolute error leads to the same conclusion as the time step and grid convergence studies of the $laplacianFoam$ solver.

Table 3.2 Maximum and mean values of the absolute and relative errors for the diffusion test

Time Step	$\boldsymbol{E_{abs}}$**(Coarse)**		$\boldsymbol{E_{abs}}$**(Medium)**		$\boldsymbol{E_{abs}}$**(Fine)**	
	Mean (%)	**Max** (%)	**Mean** (%)	**Max** (%)	**Mean** (%)	**Max** (%)
$10^{-0}\ s$	0.61	7.96	0.39	9.19	0.41	8.59
$10^{-1}\ s$	0.33	2.01	0.06	1.59	0.04	0.98
$10^{-2}\ s$	0.32	1.53	0.06	0.73	0.004	0.90
$10^{-3}\ s$	0.32	1.54	0.06	0.64	$2.2\cdot 10^{-5}$	$1.2\cdot 10^{-3}$
Time Step	$\boldsymbol{E_r}$**(Coarse)**		$\boldsymbol{E_r}$**(Medium)**		$\boldsymbol{E_r}$**(Fine)**	
	Mean $(\boldsymbol{10^{-4}}\ \%)$	**Max** $(\boldsymbol{10^{-2}}\ \%)$	**Mean** $(\boldsymbol{10^{-5}}\ \%)$	**Max** $(\boldsymbol{10^{-3}}\ \%)$	**Mean** $(\boldsymbol{10^{-5}}\ \%)$	**Max** $(\boldsymbol{10^{-3}}\ \%)$
$10^{-0}\ s$	1.3	1.06	5.21	3.40	4.12	1.14
$10^{-1}\ s$	1.3	1.12	5.25	3.60	4.19	1.21
$10^{-2}\ s$	1.3	1.13	4.12	3.63	3.08	1.21
$10^{-3}\ s$	1.3	1.13	4.10	3.64	2.00	1.22

This test shows the validity of the diffusion module for the solver responsible for the miscibility water in the ADF without heat exchange. It also reassures about the code consistency. Indeed, by defining a computational domain containing a single phase, no additional phase was created through the iterations.

3.4.2 Miscibility-energy validation test

The second test case is for the validation of the computed temperature of a mixture. Results are compared to the experimental results published in (Rodríguez-Ocampo et al., 2020). The test case is a dam-break designed for the mixture of two species at different temperature. The temperature is monitored during 44.5 s with 10 thermistors placed at unique positions. Figure 3.6 presents the computational domain at the initial time and thermistors positions. The two species are presented by "L_1" and "L_2", thermistors positions are noted by "$S_{01}\ S_{02}\ \ldots S_{10}$". Initially L_1 is placed in the compartment C_1 at 291.95 K and L_2 is placed in the compartment C_2 at 325.35 K.

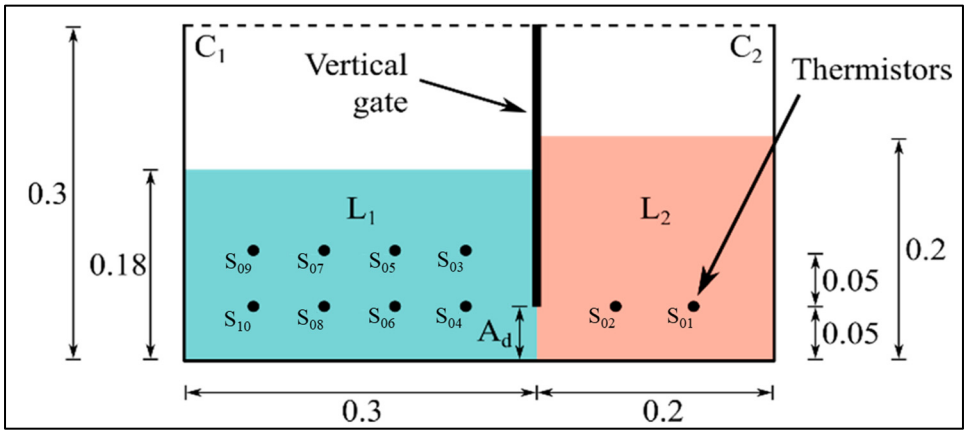

Figure 3.6 Computational domain and thermistors positions
Taken from Rodríguez-Ocampo et al. (2020, p. 5)

Four different uniform meshes, whose characteristics are presented in Table 3.3, with four different CFL numbers, were used for a grid and time-step convergence study. The results were treated with the same methodology used in (Rodríguez-Ocampo et al., 2020). The probes results were compared to the thermistors results presented in (Rodríguez-Ocampo et

al., 2020). Table 3.4 presents the maximum and means errors for the different computations. The presented error is the average error over the 10 probes. The best result is reported for the Fine mesh with the larger CFL number ($\mathrm{CFL} = 1$).

Table 3.3 Mesh Characteristics for the Energy-Diffusion Test

	Direction	**Cell Number**	**Cell Size (mm)**
Coarse Mesh	X	50	10/4
	Y	30	10/4
Medium Mesh	X	100	10/8
	Y	60	10/8
Fine Mesh	X	200	10/16
	Y	120	10/16
Extra-Fine Mesh	X	400	10/32
	Y	240	10/32

However, for the same CFL number, the Medium and Extra-Fine meshes present quite comparable errors. It is also to be mentioned that for the Fine mesh, the CFL dependency of the error is low.

Table 3.4 Maximum and Mean errors for the Energy-Diffusion Test

CFL	**Coarse Mesh**		**Medium Mesh**		**Fine Mesh**		**Extra-Fine Mesh**	
	Mean	**Max**	**Mean**	**Max**	**Mean**	**Max**	**Mean**	**Max**
1	4.68%	8.21%	3.49%	5.77%	3.30%	4.76%	3.34%	4.95%
1/2	4.80%	7.66%	3.47%	6.34%	3.56%	5.53%	3.75%	5.61%
1/4	5.21%	9.52%	3.86%	6.83%	3.56%	5.61%	4.67%	6.73%
1/8	6.89%	11.8%	3.54%	6.15%	3.56%	5.61%	3.97%	6.98%

In the current test case, the temperature is monitored on discrete points and the dam break creates eddies that may or may not pass by the probe locations. Initial perturbations because

of numerical errors may also affect the eddies positions and sizes which reflects on results. Figure 3.7 shows the eddy presence in the flow. It presents the liquid temperature field at $0.5\ \text{s}, 4\ \text{s}$ and $10\ \text{s}$ for the four meshes and a $\text{CFL} = 1$. The black dots reflect the probe locations. This figure reveals the formation of two eddies: (i) A hot eddy is created at 0.5 s caused by the propagation of L_2 in the compartment C_1 and (ii) A cold eddy is present at 4 s caused by the propagation of L_1 in the compartment C_2. For the Fine and extra Fine meshes, the cold eddy is divided in two eddies.

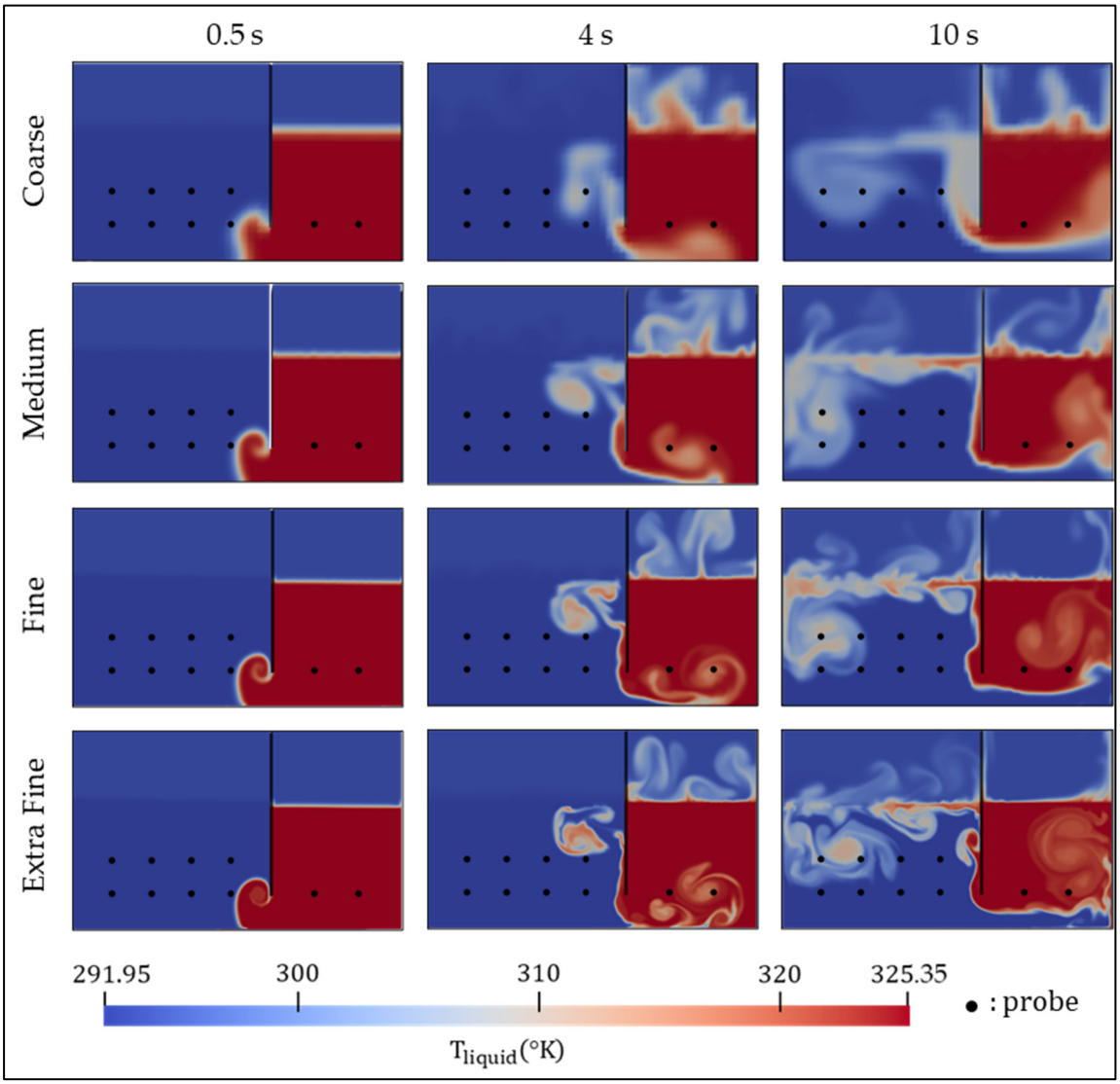

Figure 3.7 Temperature fields at different times for the four meshes (CFL = 1)

For comparison, Figure 3.8 presents the best result obtained with the $AGDEulerFoam$ solver versus the result of $IMTFoam$ validated in (Rodríguez-Ocampo et al., 2020). Initially, the two solvers present the same accuracy level. After approximately 7 s, the $AGDEulerFoam$ shows better results. The error does not exceed 5%. The maximum error for $IMTFoam$ is of the order of 7%. Overall, the $IMTFoam$ solver presents an average error of 4.85%, greater than the 3.30% error of the $AGDEulerFoam$. Again, the space-discrete data monitoring of an eddy characterized phenomenon prevents conclusions about which solver is more accurate.

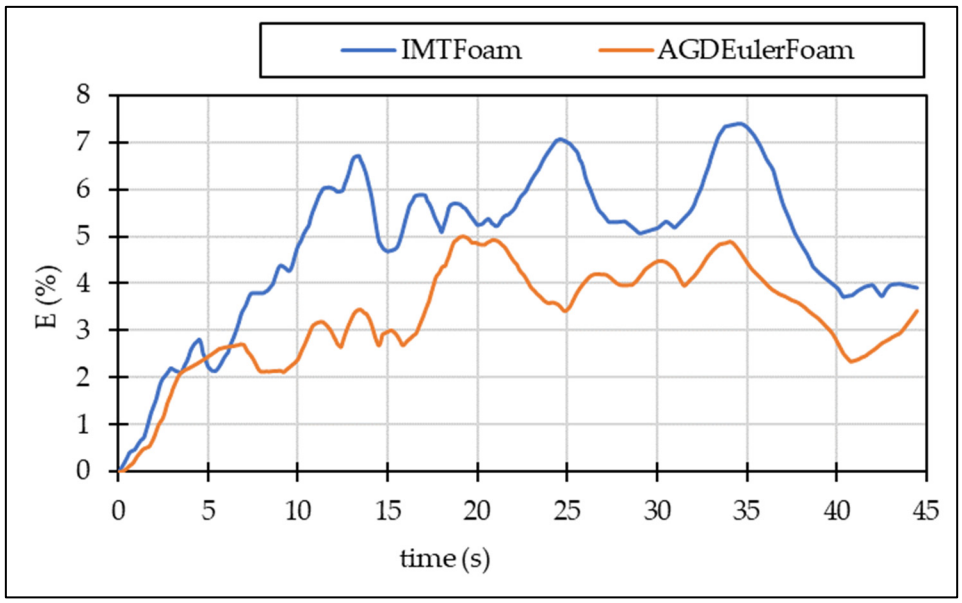

Figure 3.8 Errors' evolution of $IMTFoam$ versus $AGDEulerFoam$

However, the $AGDEulerFoam$ provides results comparable to the ones from the validated $IMTFoam$. Therefore, results are considered satisfying. It is also to be mentioned that (Rodríguez-Ocampo et al., 2020) is, to the best of the authors' knowledge, the only study presenting experimental results about energy transfer between miscible liquids in a two-phase flow.

3.4.3 Impinging jet validation

The AGD is carried out by a hot dispersed spray. For validation, the solver is tested on a less dispersed non-isothermal free-surface flow of a liquid jet impinging on a heated surface (Stevens, 1988). This test case serves to assess the accuracy of the predicted pressure distribution exerted by the jet on a flat plate. It also assesses the accuracy of the convective heat transfer between the liquid film resulting from the impingement on the heated surface. The pressure distribution is compared to Tong (2003) numerical results. The convesctive heat transfer is compared to Edin and Šefko's (2015) numerical results and Stevens's (1988) experimental results.

The computational domain of the test case is presented in Figure 3.9. It consists of an axis-symmetric (2D) domain. Initially, the domain contains only air at ambient temperature (20°C). The water is injected at the same temperature from the inlet with a velocity U_0. A constant heat flux q_{wall} is applied at the plate. The liquid jet impinges the surface, and the liquid is heated due to the constant heat flux applied to the wall. The results are monitored once the steady state is reached. The relevant test case parameters are presented in Table 5.

Table 3.5 Impinging jet test case parameters

Nozzle diameter	d	4.06 mm
Kinematic viscosity	ν	$10^{-6}\ ms^{-1}$
Reynolds number	Re	10600
Wall heat flux	q_{wall}	$1.49 \cdot 10^{5}\ Wm^{-2}$

The Reynolds number is defined as $Re = 4Q/\pi d\nu$ with Q the inlet volume flow rate.

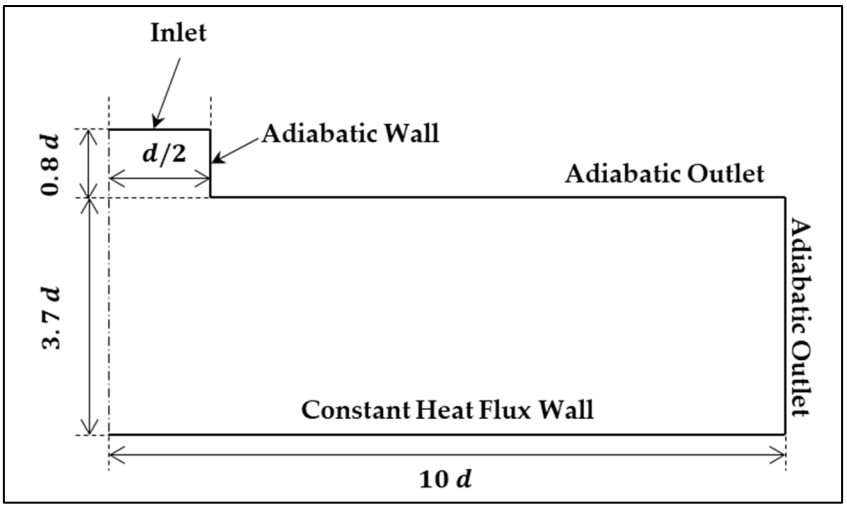

Figure 3.9 Computational domain of the impinging jet test case

The turbulent flow effects are neglected at the nozzle exit since the radial velocity of the thin liquid film spreading over the heated surface is relatively small. Therefore, it is assumed, as in (Edin & Šefko, 2015), that the flow relaminarizes and stays laminar after the impingement. A uniform velocity is set at the inlet with a slip condition at the nozzle wall to get a uniform velocity at the nozzle-tip (at 3.7d from the plate). The domain is discretized using uniform square cells with constant edge length in both X and Y directions. Four cell sizes, presented in Table 6, were tested for a grid dependency study. The four meshes predicted the same pressure distribution (less than 1% of maximal variation). Thus, the effect of the cell size is presented, in this paper, only for the Nusselt number defined in Equation (3.19) (Edin & Šefko, 2015).

Table 3.6 Mesh characteristics for the impinging jet test

Mesh	**Cell Edge Length**	**Cells Number**
Coarse	d/10	3740
Medium	d/20	14960
Fine	d/40	59840
Extra-Fine	d/80	239360

$$Nu = \frac{d \cdot \nabla T_{wall}|_{\perp}}{T_{inlet} - T_{wall}} \tag{3.19}$$

Figure 3.10 presents the Nusselt number distributions and variations for the four tested meshes. The horizontal axis presents the dimensionless distance (r/D) to the stagnation point. The four profiles have the same tendency, the heat transfer increases slightly outwards the stagnation point (r/D < 0.7) then decreases hyperbolically (r/D > 0.7). Refining the mesh increases globally the convective heat transfer. The variation between the meshes increases outwards the stagnation points presenting a local extremum at r/D=1.4 for the Coarse and Medium meshes. The variation between the Fine and Extra-Fine meshes increases slightly outwards from the stagnation point and remains under 3% and the local extremum is not present. Therefore, a cell size of D/40 suffices to reach a grid-independency for the prediction of the convective heat flux.

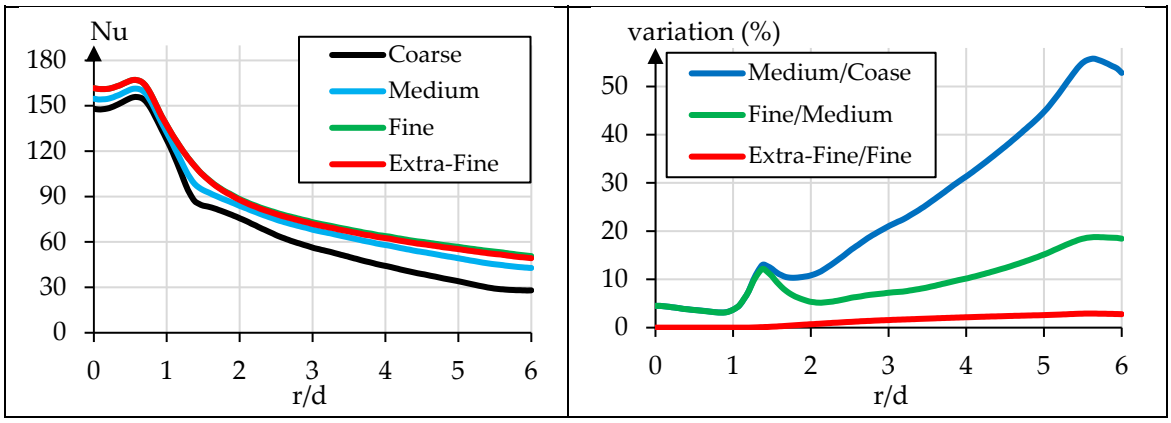

Figure 3.10 Nusselt number distribution for the four meshes (on the left) and Nusselt number variation (on the right)

In what follows the Extra-Fine mesh results are compared to the literature results. Figure 3.11 presents a comparison between the pressure distribution predicted by the present simulation versus Tong (Tong, 2003) numerical results. As seen, the pressure distributions show a very good agreement. A maximum difference of 2.28% is monitored at 0.54D from the stagnation point. The mean difference between the two data set is 0.77%.

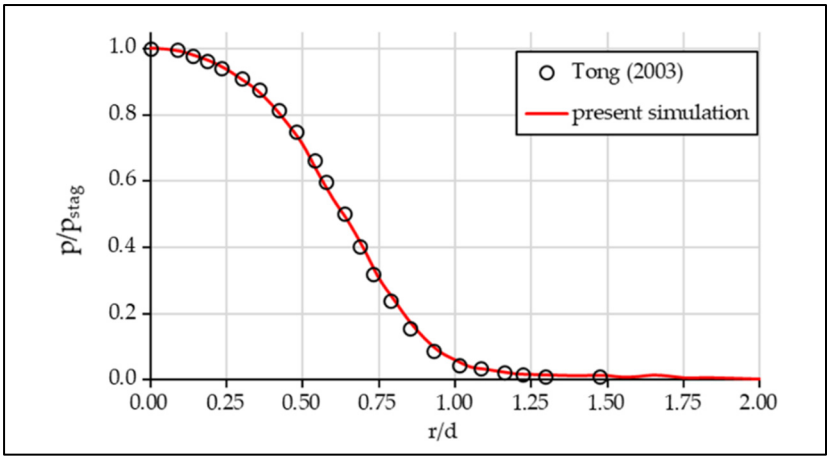

Figure 3.11 Dimensionless pressure distribution at the wall

Finally, Figure 3.12 compares the Nusselt number distribution of the present simulation versus Edin and Šefko's numerical results (Edin & Šefko, 2015) and Stevens's experimental results (Stevens, 1988). Edin and Šefko's OpenFOAM numerical results agreed well with the experimental results with a maximal error of 20% at approximately r/d = 0.6. The present simulation presents the same error profile with a maximal error of 12%. The solver is considered valid for the heat transfer prediction of an impinging jet. In the next paragraph, the same computational domain is used for a deicing simulation.

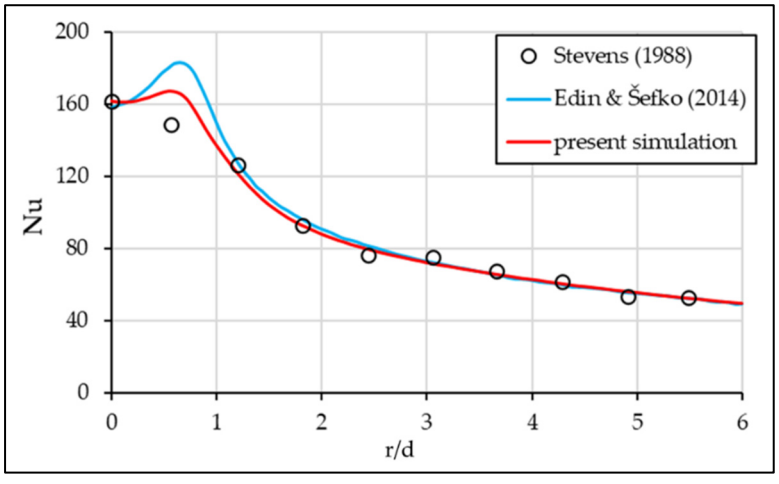

Figure 3.12 Nusselt number distribution comparison

3.4.4 Permeability coefficient calibration

In this section, an ice block is introduced to the computational domain of the impinging jet test case. Figure 3.13 presents the main modifications made to the initial conditions. The meshes are the ones used for impinging test case. The liquid is injected with the same Reynolds number as in Section 3.3 at 60 °C and it is composed by ADF instead of water. The internal field contains air at −5 °C. An ice block (9D × D/2) composed by water is set on the bottom-wall boundary at −5 °C. Finally, the constant heat flux boundary condition on the bottom-wall is replaced by a zero-gradient boundary condition.

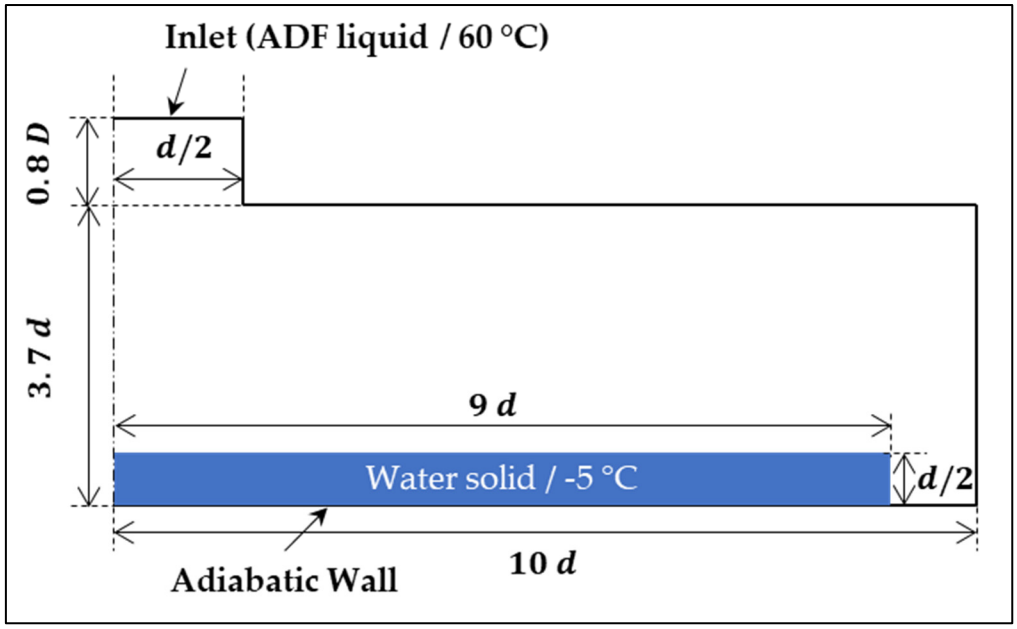

Figure 3.13 Initial conditions for the permeability coefficient calibration

The thermophysical properties of the 3 species (air, water and ADF) are presented in Table 3.7. At each iteration, the density field is updated following the phase equation of state. The gaseous phase is treated as an ideal gas and the liquid phase is treated as a perfect fluid. ADFs are mainly composed of ethylene glycol. They also contain corrosion inhibitor and other fluids to reduce their surface tension and increase their viscosity. Their composition varies also depending on the manufacturer.

As the aim of this section is to calibrate the permeability coefficient, then the ADF will be considered as pure ethylene glycol. First, the Fine mesh is used to run a first set of computations with four permeability coefficient values ($10^4, 10^5, 10^6$ and 10^7). Then, if a sensibility is detected, the mesh will be refined until the results become unsensitive to the permeability coefficients.

Table 3.7 Thermophysical properties

			Phases/ Species		
			Gas Phase	**Liquid Phase**	
Equation of state			$\rho = \frac{M}{RT}p$	$\rho = \frac{M}{RT}p + \rho_0$	
Properties	**Symbol**	**Unity**	**Air**	**ADF**	**Water**
Mol weight	M	g	28.96	62.07	18.02
Fluid constant	R	J/K/mol	8.31	$3.00 \cdot 10^3$	$3.00 \cdot 10^3$
Reference density	ρ_0	kg/m^3	–	$1.11 \cdot 10^3$	$9.98 \cdot 10^3$
heat capacity	Cp	$J/kg \cdot K$	$1.00 \cdot 10^3$	$2.40 \cdot 10^3$	$4.18 \cdot 10^3$
Dynamic viscosity	μ	$Pa \cdot s$	$1.85 \cdot 10^{-5}$	$1.60 \cdot 10^{-2}$	$8.53 \cdot 10^{-4}$
Prandtl number	Pr	–	0.70	2.61	6.99
Solidification temperature	T_s	K	–	260.15	273.15
Latent heat of fusion	L	J/kg	–	$1.81 \cdot 10^5$	$3.34 \cdot 10^5$
Schmidt number	Sc	–	–	720	

Figure 3.14 presents the ice volume evolution through time for the different permeability coefficients using the Fine mesh. The permeability coefficients $10^5, 10^6$ and 10^7 gave approximately the same results. The permeability coefficient of 10^4 provides, however, a different melting rate. A maximal difference of 13% was monitored between this computation and other results.

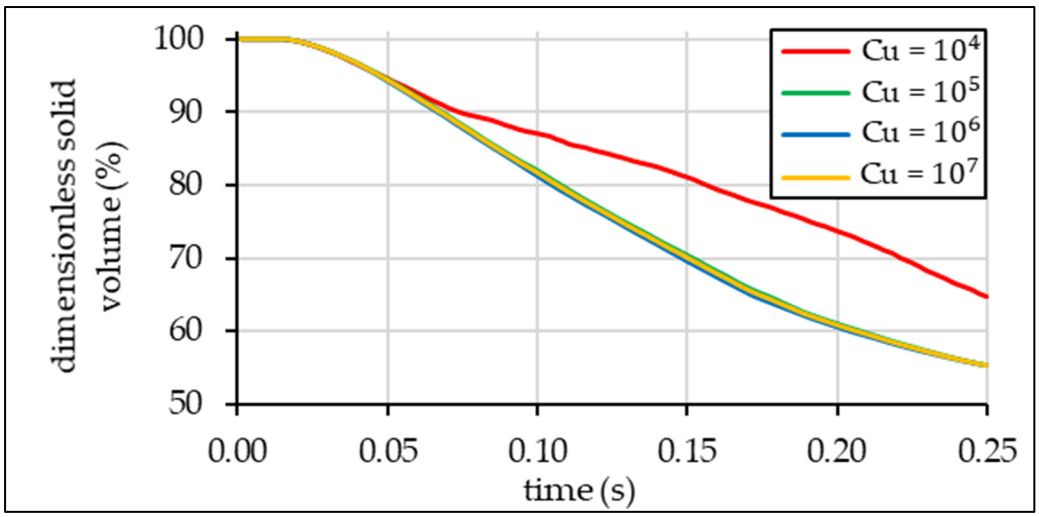

Figure 3.14 Dimensionless solid volume evolution through time (Fine mesh)

Figure 3.15 presents the same results using the Extra-Fine mesh. The same inference could be made for this mesh as for the Fine mesh with the exception that maximal difference was reduced to 4%. It can be concluded that the unsensitivity to the permeability coefficient is reached using the Extra-Fine mesh.

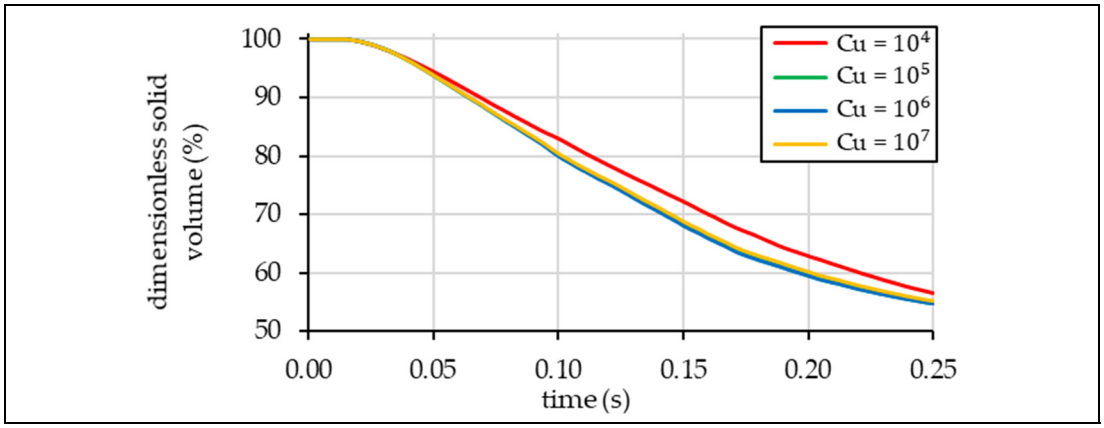

Figure 3.15 Dimensionless solid volume evolution through time (Extra Fine mesh)

With the Fine mesh, the results are unsensitive to permeability coefficient between 10^5 and 10^7. It is interesting for an engineering purpose to re-run the test-case using a Coarse mesh with a permeability coefficient of 10^6. Figure 3.16 presents on the same graph the melting rates for the three tested meshes using a permeability coefficient of 10^6.

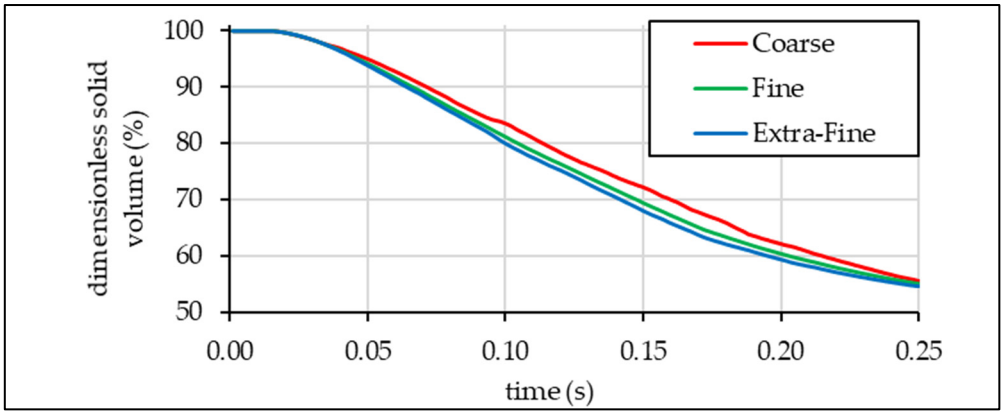

Figure 3.16 Dimensionless solid volume evolution through time for different meshes (Cu = 10^6)

The Coarse mesh provides a result similar to the Extra-Fine mesh with a maximal error of 4.19%. It is an interesting result giving that the Extra-Fine mesh contains 64 times more cells than the Coarse mesh. Ice melts slower using the Coarse mesh, which is consistent with the fact that the Nusselt number was also under-predicted for the impinging test-case using the Coarse mesh.

3.5 Discussion and Conclusions

A new OpenFOAM-V6 based solver ($AGDEulerFoam$) was developed for simulating a dispersed two-phase flow enabling the definition of the phases as a mixture of multiple species with different thermophysical properties. The enthalpy-porosity technique is extended to handle phase change in multiphase flows. It is coupled to the new solver to model the solidification (and melting) of a liquid phase (of a solid phase). The $AGDEulerFoam$ was developed by programming a species transport equation in the pre-existing OpenFOAM $twoPhaseEulerFoam$ native solver. The thermophysical properties of the multi-species phase are updated following the rule of mixtures at each iteration. The species miscibility module precision is assessed with a comparison versus the $laplacianFoam$ solver validated in (Hermosilla, 2016 ; Mironova, 2018 ; Noriega, 2016). A maximum difference of 0.01% was recorded between the two solvers. Developments

achieved in this study are part of a design methodology for a numerical bench test of the aircraft ground deicing process in order to improve its efficiency.

It is to be noted that no CFD method is defined in the literature to simulate the ice shape evolution in the aircraft ground deicing process. This paper presents a model first of its kind developed on an open-source CFD framework for the aircraft ground deicing simulation. This paper is a complementary effort to simulate the ice decontamination in the context of a numerical test bench. The main findings of the present paper are summarized into three points:

1. The developed solver predicts unsteady temperature evolution of a two-phase flow in which one phase is a mixture of two species with a precision of 95%. This precision is observed in a 2D dam-break simulation involving mixture.
2. The proposed solver predicts the convective heat transfer between liquid formed by an impinging jet and a heated wall with a maximal error of 12%. This result is comparable to the existing models.
3. The permeability coefficient of the extended enthalpy-porosity technique is calibrated through a sensitivity study proposed in (Ebrahimi et al., 2019). The results are insensitive to the permeability coefficient with an Extra-Fine mesh. The ice shape evolution can be well predicted with a Coarse mesh with a permeability coefficient of 10^6, which is within the interval stated by Ebrahimi et al. (2019).

In other words, the proposed CFD method is able to simulate a dispersed two-phase flow with the solidification/melting of one phase. Those characteristics make it able to simulate an AGD process. For better computations efficiency, the present model will be coupled to a Lagrangian model. The Lagrangian model will be used for simulating the majority of the spray far from the contaminated surface. The present model is used for the simulation of a relatively thin layer of the computational domain where the ice melting is modelled. The final solver will be used to simulate a 3D AGD test case and a parametric study of the process to determine the AGD process sensitivity to the ADF spray parameters.

CHAPITRE 4

A MULTI-REGION CFD MODEL FOR AIRCRAFT GROUND DEICING BY DISPERSED LIQUID SPRAY

Sami Ernez [a], François Morency [b]

[a,b] Department of mechanical engineering, École de Technologie Supérieure,
1100 Notre-Dame Ouest, Montréal, Québec, Canada H3C 1K3

Article published in « energies »,
August 2022

4.1 Abstract

The aircraft ground deicing (AGD) process is a mandatory step before taking off in a cold climate. The development of CFD (computational fluid dynamics) tools to simulate AGD could help the industry reduce its costs and limit pollution. Previous works have modelled some parts of the AGD process. Building on these previous works, this paper presents a three-dimensional (3D) CFD algorithm to simulate the process in full scale. The algorithm comprises a multi-region model where a Lagrangian method solves the spray particle equations, and an enthalpy–porosity approach with an Eulerian method simulates the ice melting. The multi-region approach is verified in this paper through a spray-tip penetration (STP) test. The STP predicted using the multi-region model had 99% agreement with the STP predicted using a Lagrangian method. Therefore, the multi-region technique correctly modeled the particle momentum between the two regions. This paper also presents a numerical calibration of the permeability coefficient for the extended enthalpy–porosity technique in the context of AGD. The numerical calibration of the permeability coefficient will enable future parametric studies of the AGD process.

Keywords: aircraft ground deicing (AGD); multi-region model; particulate two-phase flows; spraying parameters; spray tip penetration (STP); extended enthalpy–porosity technique

4.2 Introduction

Pilots decide to apply ground deicing or anti-icing treatments before take-off on any civil aircraft, if they expect to operate under suspected or known ground ice conditions (ICAO, 2018a). Figure 4.1 presents a scheme of the typical ground deicing process. An operator directs a preheated aircraft deicing fluid (ADF) spray to the contaminated surface. The ice melts and a liquid film, composed of ADF and water, flows over the surface and lands on the tarmac. This operation adds a noticeable cost to flights in winter. Recently, research efforts have focused on improving the deicing process. Process guidelines are suggested in (ACRP Fact Sheets, 2016) based on technical and manufacturer reports, guidance materials and standards, technological patents, and procedures. Most of the guidelines are empirical and not mandatory. However, an audit before take-off guarantees process quality. To improve the process, Chen et al. (2016) propose a numerical optimization through heat balance analysis. Their model links the ice thickness and the weather with the ADF flow rate and the process time, and offers a potential reduction of up to 20% of consumed ADF volumes.

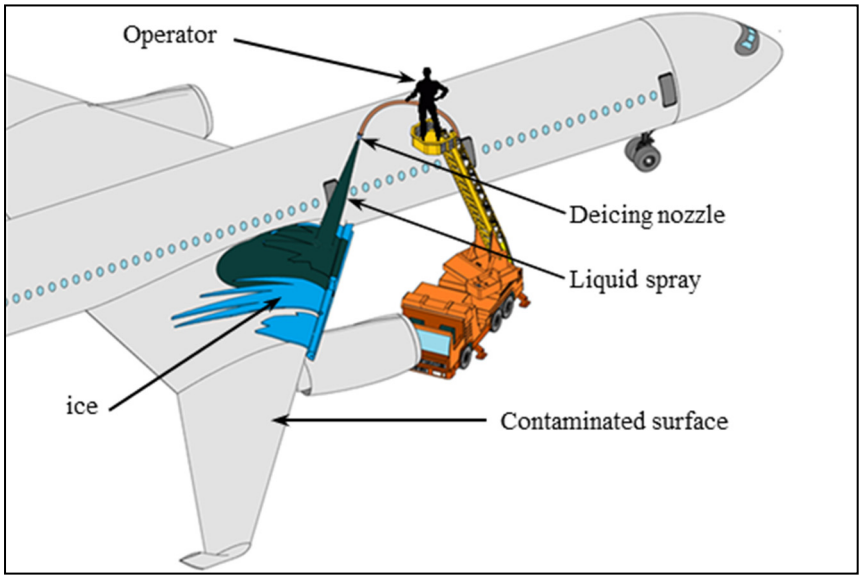

Figure 4.1 Representative scheme of the ground deicing process

A CFD-based test bench of the AGD process could also lead to process improvement. The test bench goal was to study the influence of different parameters, including the spray inclination angle and the flow rate, on the total process time and the required ADF volumes. The test bench involved modeling a dispersed multiphase flow with heat transfer and phase change. To develop the test bench, initial research efforts studied the convective heat transfer between an ADF spray and a surface using the volume-of-fluid (VOF) method (Yakhya et al., 2019). The spray dispersion was omitted in this study. Previous research (Ernez & Morency, 2019c) included replacing the VOF method with a Lagrangian drop in Eulerian fluid (LDEF) method, taking into account the dispersion of the droplets. The model demonstrated a comparable precision of 85% and a lower computation cost.

A previous CFD study (Ernez & Morency, 2021a) was the first to model ice melting with an ADF spray. The study coupled an Eulerian drop in an Eulerian fluid (EDEF) method with an extended version of the enthalpy–porosity technique to simulate the ice melting. Figure 4.2 presents a typical computational domain for the problem. In the first region, an Eulerian–Lagrangian approach models the multiphase flow of the liquid spray. An EDEF approach models the spray impingement on the ice in the relatively thin second region. Reference (Ernez & Morency, 2021a) validated only the Eulerian region and calibrated the enthalpy–porosity technique in two dimensions. The present work proposes a multi-region model solving simultaneously the two regions and verifies the momentum transfer between the two regions in 3D.

The EDEF and the LDEF approaches were compared by Durst et al. (1984); the authors found similar results for a pipe flow and a separated flow (sudden pipe expansions). Both approaches have their advantages. The LDEF approach is recommended for poly-dispersed distributions. It makes the best prediction for flows with high particle velocity gradients. It reduces particle discretization errors, even if the simulation uses a coarse grid for the fluid phase. These characteristics are associated with the AGD problem and an LDEF approach is favored. Additionally, in the AGD problem, the spray must interact with a liquid film. The addition of a film model to a Lagrangian spray solver requires a dynamic mesh to follow the ice interface. The EDEF approach avoids the need for a dynamic mesh in the ice's vicinity.

The literature review (Gouesbet & Berlemont, 1999) corroborates previous (Durst et al., 1984) results, adding that the LDEF is superior for mass transfer between phases, such as evaporation.

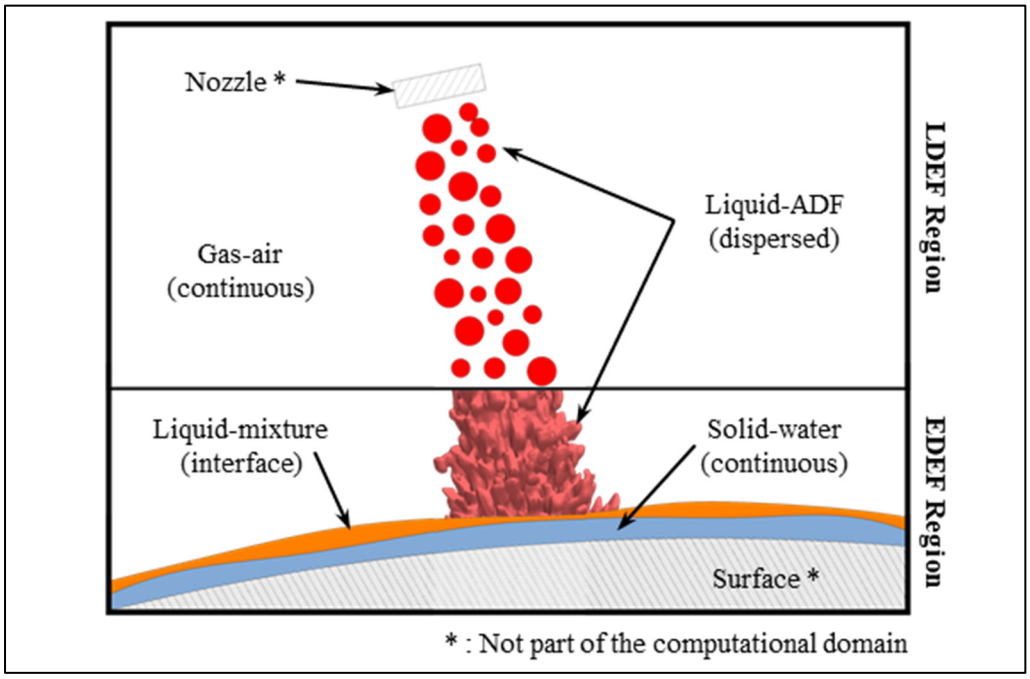

Figure 4.2 Typical computational domain for the proposed methodology

Another study (Nijdam, Guo, Fletcher, & Langrish, 2006) compared the two approaches for spray simulations, and confirmed the superiority of LDEF for the poly-dispersal feature of the spray topology. The literature review (Subramaniam, 2013) confirmed that LDEF is better than EDEF for poly-dispersed flows and for interphase quantity transfer. Reference (Saidi, Rismanian, Monjezi, Zendehbad, & Fatehiboroujeni, 2014) compared the two approaches for predicting the free diffusion motion. The LDEF approach demonstrated better results for dispersed particles with low volume fraction. Reference (Xu, Han, & Qu, 2020) compared the two approaches for prediction of particle deposition in turbulent flows. The two methods demonstrated comparable results for particles with a diameter greater than 16 μm. However, EDEF had less computational cost.

Based on those studies, the present work used the LDEF approach to compute the spray drops' travel from the nozzle to a near-ice vicinity. This ensured a reasonable computing cost. From this near-ice boundary, the Lagrangian drops were converted to Eulerian drops. The droplet paths from the near-ice to the ice boundary were computed with the EDEF approach. From the near-ice boundary, the impingement and the ice melting create a higher void fraction. This article presents a multi-region solver intended to simulate the AGD process. It develops and verifies a numerical method to combine the two solvers used in (Ernez & Morency, 2019c). The solvers are based on the open-source CFD toolbox OpenFOAM-V6.

The mathematical model and numerical method are presented in Sections 2 and 3. Section 4 shows the verification and a validation (V&V) of the momentum transfer between the LDEF and EDEF regions. The same section includes a technical review to determine the spray injection parameters. Finally, a 3D calibration of the permeability coefficient for the extended enthalpy–porosity technique is presented.

4.3 Mathematical Model

To achieve the AGD process model, a multi-region solver was built. Previous works (Ernez & Morency, 2019c) have demonstrated the mathematical models and numerical methods for the LDEF and EDEF regions. This section of the current paper attends to the mapped boundary between the two regions. Figure 4.3 summarizes the entire model. The LDEF region, presented in blue, is composed of Lagrangian and Eulerian fields. In this region, the two phases exchange momentum, energy, and species. These exchanges occur through drag, heat transfer, and evaporation. Eulerian fields are converted into a continuous phase at the mapped boundary, and Lagrangian fields are converted into a dispersed phase. This conversion is based on mass, momentum, and energy conservation.

In the LDEF region, droplets dispersed in a gaseous phase simulate the liquid spray. The liquid droplets are modeled by a Lagrangian cloud of particles. An Eulerian field models the

gaseous phase. The mapped boundary links the LDEF region to the EDEF region; the mapped boundary converts the Lagrangian particles into Eulerian particles.

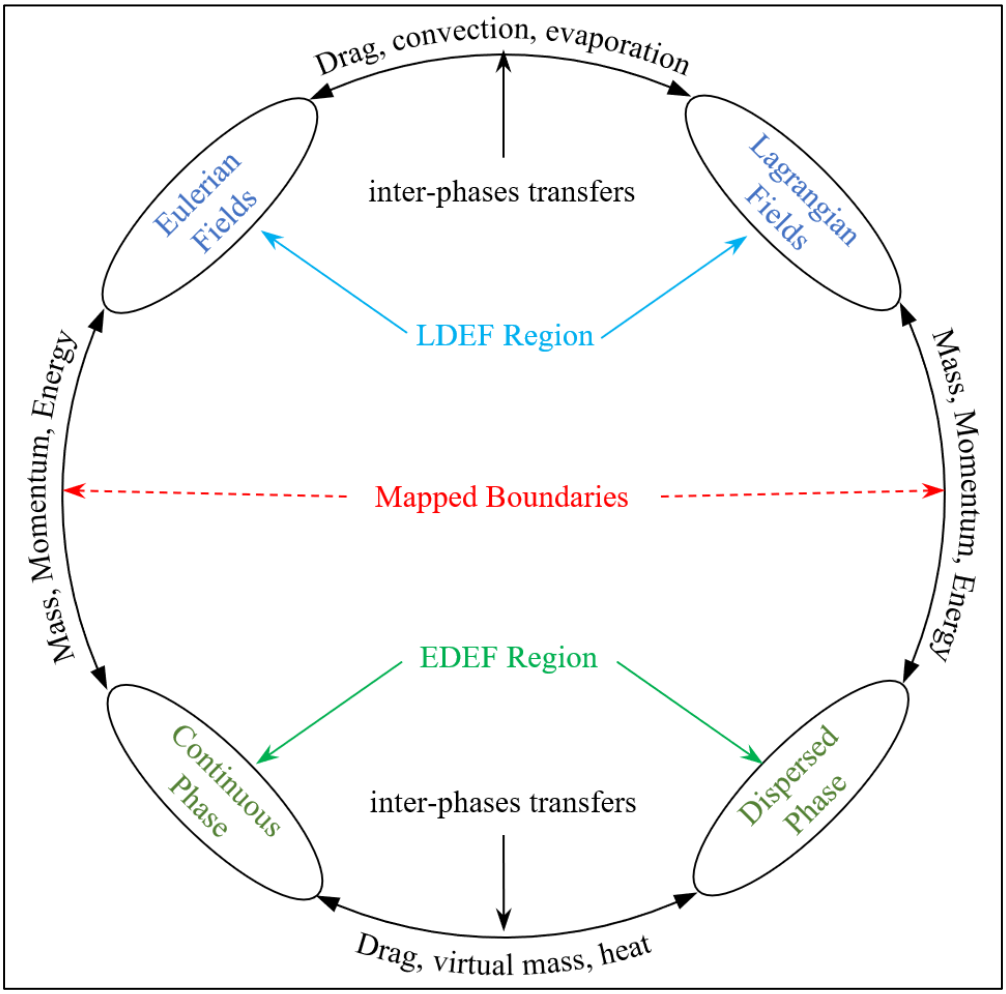

Figure 4.3 Physical phenomena linking the LDEF and EDEF region's objects

Figure 4.4 explains the conversion methodology. The LDEF boundary cell (on the left) may contain several Lagrangian particles at the same time. Those particles may travel the mapped boundary together at the same time step. Each particle is characterized by a different mass, velocity, and temperature. Traveling the boundary should result in the equivalent Eulerian field values assuring mass, momentum, and internal energy conservations. The total mass is simply the sum of all particle masses. The resulting mass is then converted to a void fraction

using the cell volume. For each cell, equation (4.1) converts the particle volumes into a void-fraction:

$$\alpha_{liquid} = \frac{\sum_{particles} V_{paticles}}{V_{cell}} \tag{4.1}$$

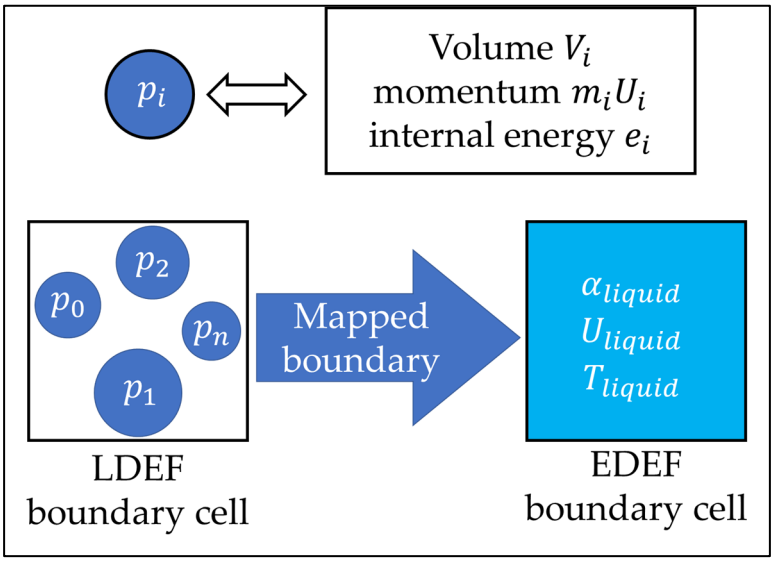

Figure 4.4 Lagrangian fields conversion methodology

where V and α designate volumes and void-fractions. As a cell in the LDEF region may contain multiple particles, particle volumes are clustered together.

The velocity is deduced using Equation (4.2) from the momentum conservation. The total momentum is the sum of all particle's momentum $m_{particle} \cdot U_{particle}$:

$$\mathrm{U_{liquid}} = \frac{\sum_{\mathrm{particles}} \mathrm{m_{particle}} \cdot \mathrm{U_{particle}}}{\sum_{\mathrm{particles}} \mathrm{m_{particle}}} \tag{4.2}$$

The temperature is deduced using equation (4.3) from the internal energy conservation. The total internal energy is the sum of all particle's internal energy $\mathrm{m_{particles}} \cdot \mathrm{C_p} \cdot \mathrm{T_{particle}}$:

$$\mathrm{T_{liquid}} = \frac{\sum_{\mathrm{particles}} \mathrm{C_p} \cdot \mathrm{m_{particles}} \cdot \mathrm{T_{particles}}}{\sum_{\mathrm{particles}} \mathrm{C_p} \cdot \mathrm{m_{particles}}} \tag{4.3}$$

where U, T, m, and C_p designate the velocity, the temperature, the mass, and the heat capacity. These two equations ensure the conservation of momentum and internal energies between the LDEF and EDEF regions.

In the EDEF region, presented in green, the two phases exchanged mass, momentum, and energy via virtual mass, drag, and heat transfer. Droplet evaporation was omitted in the EDEF region since this region was relatively thin compared to the LDEF. The flow decelerated due to the impingement, and the liquid cooled due to the heat transfer with ice.

4.4 Numerical Method

A new multi-region solver $AGDFoam$ was implemented in OpenFOAM-V6. The solver follows the same algorithm as the native solver $chtMultiRegionFoam$ (Li, 2016). The native solver simulates the heat transfer between a gaseous region and a solid region; this work maintained the overall structure of the solver. This structure handles the creation of a split-mesh morphology, enabling the definition of multiple regions linked by mapped boundaries. The algorithm section responsible for field definition and the governing equation was edited following the native solver ($sprayFoam$) for the LDEF region and the ($AGDEulerFoam$) solver developed in (Ernez & Morency, 2021a) for the EDEF region. The main contributions presented here consist of the following:

i. Implementing the LDEF and EDEF equations presented in (Ernez & Morency, 2019c) and (Ernez & Morency, 2021a) in a multi-region solver.
ii. Creating a source file to map the data between the two regions using equations (4.1)–(4.3).

Figure 4.5 summarizes the inner steps carried out at each time loop. At the beginning of the loop (blue blocks), the time steps for both regions are computed based on the maximum allowed CFL numbers $\left(\Delta t\, \Sigma u_{x_i}/\Delta x_i\right)$ set at the pre-processing phase. Next, the algorithm sets the smaller time step for both regions. The LDEF step (red blocks) comprises solving Lagrangian and Eulerian equations.

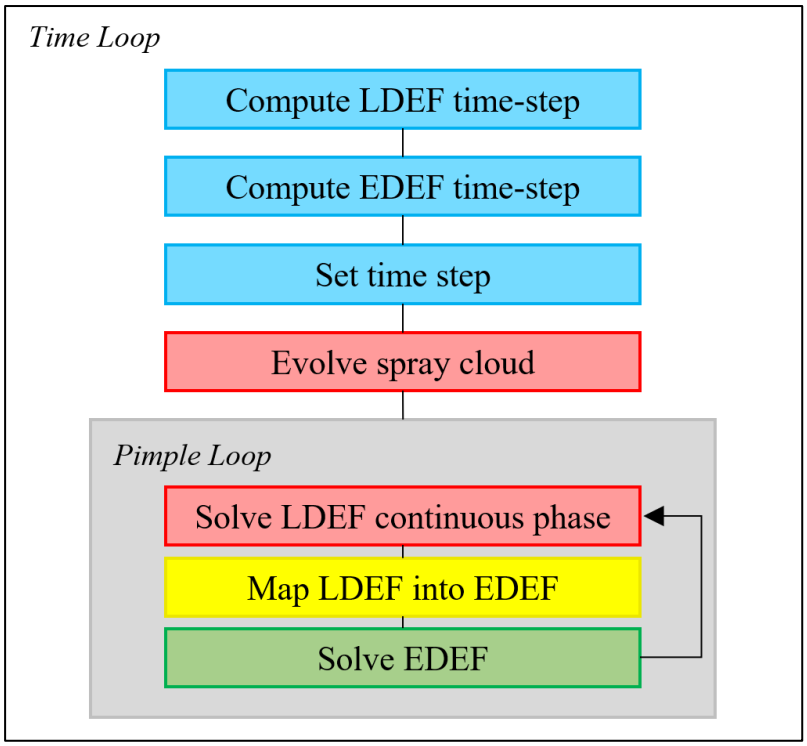

Figure 4.5 Global steps carried out at each time-step

The particle number is updated at each time step n, according to equation (4.1). The update adds to the old particle number the newly injected particles and subtracts the particles absorbed by the EDEF region and particles which exit the computational domain:

$$P_n = P_{n-1} + P_{inj,n} - P_{abs,n} - P_{esc} \tag{4.4}$$

The number of injected particles is computed following a pre-set flow rate and the particle diameter distribution. OpenFOAM provides several options for those two parameters. However, reference (Ernez & Morency, 2019c) validated the LDEF model for a constant flow-rate with a Rosin–Rammler distribution (Nasr et al., 2002).

The conservation equations are solved using the PIMPLE algorithm of OpenFOAM (Holzmann, 2017). Within one time-step, the algorithm searches for a steady-state solution with under-relaxation, then advances in time. The explicit parts of the equations are solved with three outer correction loops. After reaching a defined tolerance criterion of 10^{-6} within

the steady-state calculation, the algorithm leaves the outer correction loop and advances in time. The Lagrangian equations are analytically solved outside the pimple loop. Particles (or droplets) with identical properties, such as diameter and velocity, are associated in the same numerical parcels. Parcels are treated as point masses with no volume. Positions and velocities are updated at each time step, based on the momentum equation.

Refinement is achieved by increasing the spray parcel rates. An increase in spray parcel rate diminishes the particle number represented by a single parcel, and augments the variety of particles. Further information about the Lagrangian equations can be found in (Nobile, 2015). The pimple loop encompasses the Eulerian equations for the LDEF region, the mapping equations, and the EDEF equations for both phases. Finally, the numerical schemes and algorithm controls presented in (Ernez & Morency, 2019c) are used.

4.5 V & V & Calibration

The LDEF and EDEF equations have been validated in previous works (Ernez & Morency, 2019c). The verifications and calibration tests of the present article serve to:

i. Verify the grid- and the parcel-rate-induced errors for the Lagrangian model. This verification serves to set an adequate mesh and parcel rate for the LDEF region and to generate reference data to assess momentum conservation for the multi-region approach.
ii. Verify the STP predicted using the multi-region approach compared with the STP predicted using the Lagrangian approach. This test aims to verify the momentum transfer between the two regions.
iii. Calibrate the permeability coefficient of the extended enthalpy–porosity technique according to the methodology suggested in (Ebrahimi et al., 2019).

4.5.1 Spray Tip Penetration (STP) Test Case

Injection Parameters

OpenFOAM's Lagrangian framework injects particle spray without solving the flow inside the nozzle. The injected particle spray is characterized by a nozzle diameter, a flow rate, a particle size distribution, a spray pattern, a parcel rate, and an injection pressure. The inlet particle velocity is computed from the injection pressure and the ambient pressure. Previous work (Ernez & Morency, 2019c) validated spray-tip penetration for a fuel spray against the experimental results of (Mitroglou et al., 2006). Unfortunately, ADF sprays have not been experimentally investigated in the literature. Therefore, the validation of the OpenFOAM's Lagrangian framework in the context of ADF sprays is not yet possible. The main differences between the injection parameters for fuel and ADF sprays are summarized in Table 4.1.

Table 4.1 Difference between the injection parameters of fuel and ADF sprays

Parameters	**Fuel sprays** (Mitroglou et al., 2006)	**ADF sprays**
Injection pressure	120-200 bar	6 bar
Chamber pressure	1-12 bar	1 bar
Droplet mean diameter	15-25 μm	1-2 mm
Fluid viscosity	0.78 cSt	1 cSt
Fluid density	692 kg/m3	1113 kg/m3
Surface tension	0.0188 N/m	0.05 N/m

The principal difference comes from the higher injection pressure and the smaller droplets' diameter in the case of fuel sprays. This leads to greater dispersion of the fuel injection spray. The momentum conservation for the multi-region model was verified with realistic injection conditions. The SAE AS6285 (SAE, 2021) states that ADF injection pressure varies from one aircraft to another and from one aircraft part to another. However, the standardized international aircraft ground deicing program (SIAGDP) (FAA, 2010) suggests that

equipment with $50 - 275$ l/min flow rate at a pre-nozzle discharge pressure of 650 kPa is suitable for any deicing task. The nozzle BER-HT150 has a diameter of 38.1 mm (Task Force Tips, 2010) and is approved by the SAE G-12 committee. The SAE G-12 committee serves as the focal point for all ground de-icing related activities within SAE. The nozzle's manufacturer also specializes in designing firefighting nozzles; given the lack of experimental data for ADF spray, it is interesting to build an analogy between ADF sprays and firefighting sprays. Reference (Ponziani & Tinaburri, 2015) validated a Lagrangian model for firefighting sprays. The spray parameters are similar to ADF spray parameters; an injection pressure of 600 kPa with a nozzle diameter of 30 mm. However, the flow rate is higher (1251 l/min). Reference (Ponziani & Tinaburri, 2015) used same size distribution (Rosin–Rammler) with three mean diameters, 0.5 mm, 1 mm, and 2 mm, and a 12-degree spray pattern. The SIAGDP (FAA, 2010) suggest using the largest droplet size to retain maximum heat in the ADF. Hence, the highest mean diameter presented in (Ponziani & Tinaburri, 2015) was used. The computations were made using a Rosin–Rammler distribution of the droplet's diameter between 1 mm and 3 mm, with a mean value of 2 mm, see Figure 4.6. Data were acquired by post-processing 29,502 parcels. The imposed probability distribution function (PDF) was scaled and is presented (by a red curve) on the same figure.

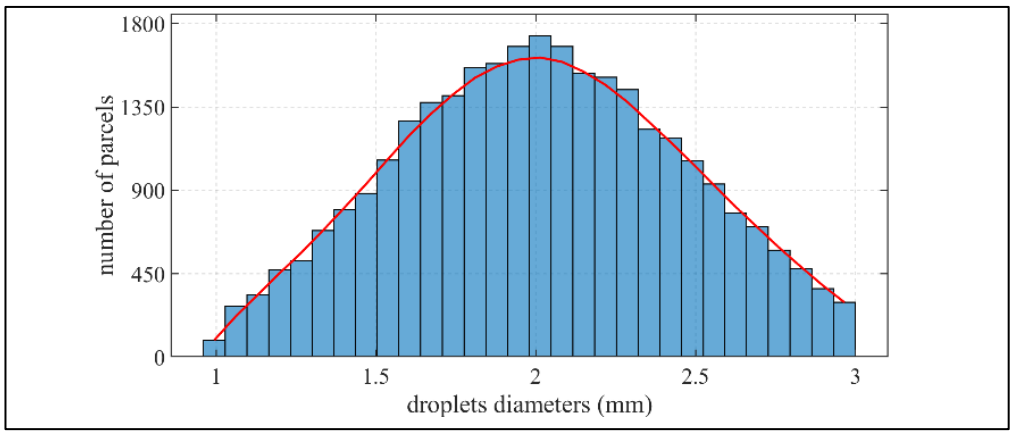

Figure 4.6 Histogram and scaled PDF of the Rosin-Rammler distribution

Table 4.2 summarizes the injection parameters used in this test. In the following, the reference data were generated by grid and parcel-rate sensibility tests. Then, the precision of the multi-region approach was assessed through comparison with the reference data.

Table 4.2 Injection parameters

Spray parameters	**Values**
Nozzle diameter (D)	38.1 mm
Injection pressure	600 kPa
Flow rate	200 l/min
Mean droplet diameter	2.0 mm
Spray pattern	12 °
Temperature	333.15 K

Computational Domain and Mesh

Figure 4.7 presents the computational domain for the STP test. The domain consisted of a cylinder with a length of 30 D. The space between the nozzle tip and the boundaries was 3.0 D to avoid particle interactions with the boundary conditions at the injection. The spray-tip penetration was tracked along 27 D, around 1.0 m.

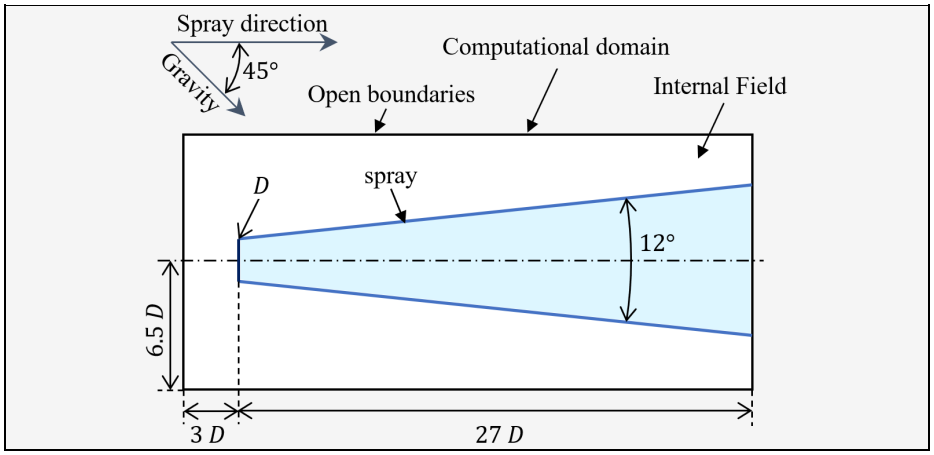

Figure 4.7 Computational domain of the Lagrangian test case

This spraying distance is typical of the AGD process (SAE, 2021). A domain diameter of 13 D ensured that spray droplets exited the cylindrical domain only through its base. The liquid spray evolved in the air (identified as “internal field” on the figure). The spray direction was at a 45° angle with gravity. To generate independent reference data from cell size and parcel size, twenty computations were performed using four meshes (presented in Table 4.3) and five parcel rates ($10^3, 10^4, 10^5, 10^6, 10^7$).

Table 4.3 Reference Data Grids

Meshes		n_R	n_θ	n_Z	Cells number
$Mesh_1$	Coarse	13	16	60	12 480
$Mesh_2$	Medium	20	24	90	43 200
$Mesh_3$	Fine	30	36	135	145 800
$Mesh_4$	Extra-Fine	45	60	200	540 000

Figure 4.8 presents a 25% grid section (axis length of 7.0 D). The grid was parametrized through three variables: the number of cells in the radius direction (n_R), the number of cells in the angular direction (n_θ), and the number of cells in the axis direction (n_Z).

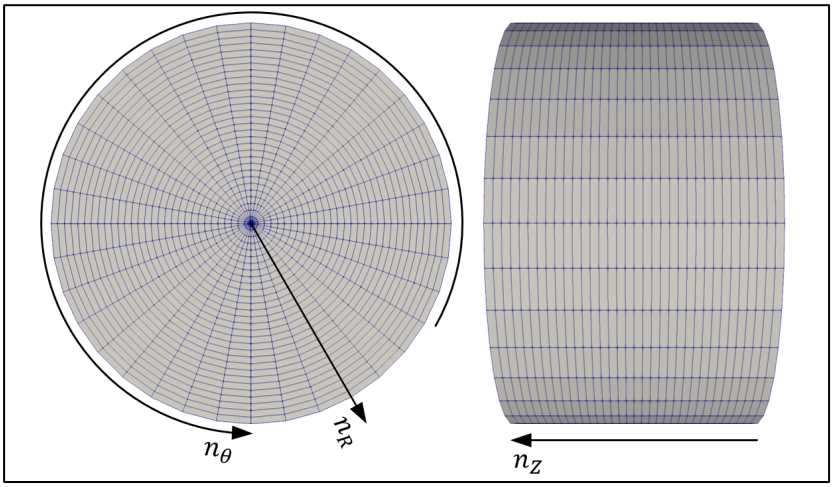

Figure 4.8 Characteristic mesh section

Thermophysical Model

ADFs are composed mainly of ethylene glycol. They also contain corrosion inhibitors and other fluids to reduce their surface tension and increase their viscosity. Their composition can vary depending on the manufacturer. For simplicity, ADFs in this paper are pure ethylene glycol. The internal field is composed of three species: dioxygen O_2, dinitrogen N_2, and ethylene glycol vapor $C_2H_6O_2$. These species are weighted by Y_{specie} and are a function of the temperature. The density is computed using the perfect gas law presented in equation (4.5):

$$\rho = \sum_{species} Y_{specie} \times \frac{M_{species}}{RT} p \tag{4.5}$$

where $M_{species}$, R, and p refer, respectively, to the species' molar weight, the fluid constant, and the pressure field.

The specific heat capacity of each species is computed in equation (4.6) as a function of the temperature following the NIST-JANAF thermochemical tables (NIST, 1998):

$$C_p = \sum \left(Y_{specie} (a_4 T^4 + a_3 T^3 + a_2 T^2 + a_1 T + a_0) \right) \tag{4.6}$$

Finally, the dynamic viscosity follows the Sutherland law presented in equation (4.7).

$$\mu = \frac{A_s \sqrt{T}}{1 + T_s/T} \tag{4.7}$$

The parameter values used in equations (4.5) and (4.7) are presented in Table 4.4

Table 4.4 Internal field thermophysical parameters

	N_2	O_2	$C_2H_6O_2$
$\mathrm{M(kg\ m^{-3}\ )}$	28.01	32.00	62.07
$\mathrm{A_s(10^{-6}kg\ m^{-1}\ s^{-1}\ K^{-1}\ )}$	1.67	1.67	1.67
$\mathrm{T_s\ (K)}$	171	171	171
$\mathrm{a_0\ (10^0)}$	3.30	3.21	1.97
$\mathrm{a_1\ (10^{-3})}$	1.41	1.13	2.02
$\mathrm{a_2\ (10^{-6})}$	−3.96	−5.76	−3.70
$\mathrm{a_3\ (10^{-9})}$	5.64	1.31	4.05
$\mathrm{a_4\ (10^{-12})}$	−2.44	−0.88	−1.46

Parcel Rate Sensitivity

The STP is defined as the height of a cylinder coaxial with the spray axis. The cylinder encompassed 95% of the spray's total mass. To assess STP sensitivity to the spray parcel rate (PR), a parcel-rate-induced error (E_{PR}) is defined. Equation (4.8) expresses the PR-induced error for a mesh "m_i" and a PR "PR_j":

$$E_{PR}(m_i, PR_j) = \frac{1}{M_{ij}} \int_{t_0}^{t_f} \left| STP(m_i, PR_{j+1}) - STP(m_i, PR_j) \right| \tag{4.8}$$

where $M_{ij} = (t_f - t_0) \cdot \max_{\text{time}} \left(STP(m_i, PR_j) \right)$ with t_0 and t_f respectively the initial and final time of the simulation.

Figure 4.9 presents the PR-induced error for the four meshes. Increasing the PR decreased the error for the four meshes. The STP sensitivity to the PR increased when the mesh was refined. The coarse mesh presented a sensitivity under 20% for a PR of 10^4 parcel/s,

whereas the extra-fine mesh continued to present a sensitivity above 20% for a PR 10 times greater. For a PR of 10^6 parcel/s, all the four meshes presented almost the same PR-induced errors of 1%, except the extra-fine mesh which presented an error of 3%. Therefore, the PR of 10^6 parcel/s was retained for the spray configuration. The next subsection analyzes the grid induced error for selection of the appropriate mesh.

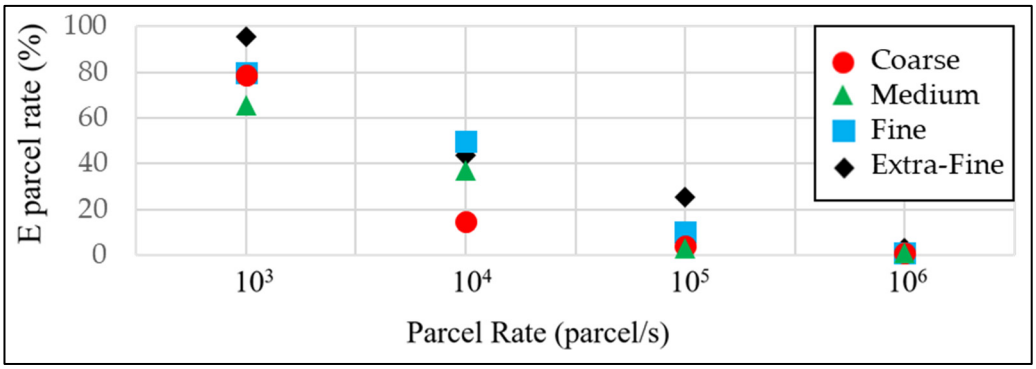

Figure 4.9 STP sensitivity to the parcel rate for the four tested meshes

Grid sensitivity

To assess the spray tip penetration (STP) sensitivity to the mesh, a grid-induced error (E_m) was defined. Equation (4.9) expresses the grid-induced error for a PR "PR_i", and a mesh "m_j":

$$E_m(PR_i, m_j) = \frac{1}{M_{ij}} \int_{time} \left| STP(PR_i, m_{j+1}) - STP(PR_i, m_j) \right| \tag{4.9}$$

Figure 4.10 presents the grid-induced error for the five tested PRs. For the "low" PRs of 10^3 and 10^4, the grid-induced errors were higher than for other PRs. The mesh refinement also increased the grid-induced error. The "high" PRs of the 10^6 and 10^7 STP predictions were almost independent of the mesh quality, both presenting a grid-induced error around 2%. Using a PR of 10^6 parcel/s allowed use of any of the studied meshes. The medium mesh was retained for the subsequent tests.

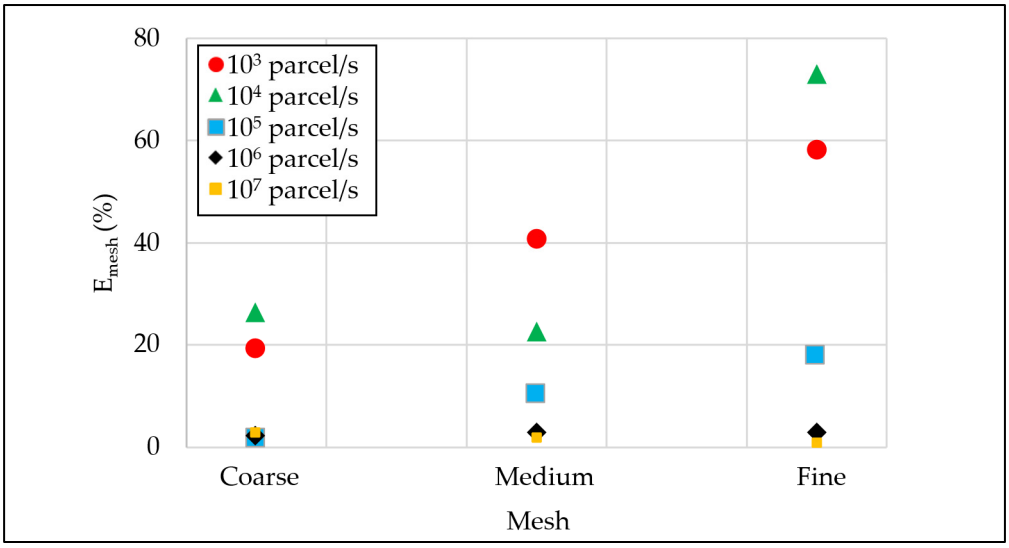

Figure 4.10 STP sensitivity to the mesh quality for the five tested spray rates

In the next subsection, the multi-region approach is verified against the retained configuration of the Lagrangian approach i.e., a medium mesh with a parcel rate of 10^6 parcel/s.

Multi-Region Validation

This paragraph compares the STP predicted using the multi-region approach to the STP predicted using the Lagrangian approach. Figure 4.11 presents the computational domain for the multi-region test case. The computational domain in Figure 4.7 is divided into two regions. The mapped boundary is located at the middle of the domain axis. The computation used the same boundary conditions, initial conditions, and injection parameters. The medium mesh was used first. Then, the EDEF region's mesh was refined until reaching STP grid insensitivity.

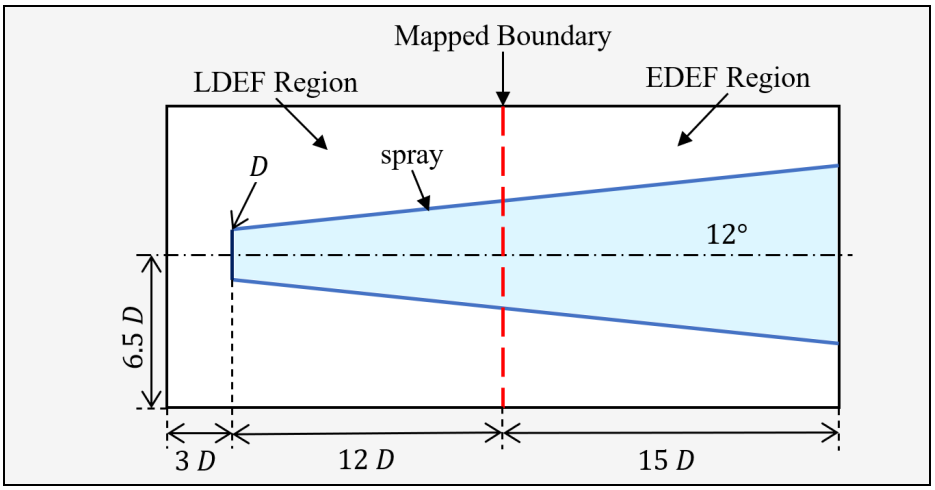

Figure 4.11 Computational domain of the multi-region test case

Figure 4.12 presents a crinkle clip of the mesh refinement architecture at three levels of refinement. The LDEF region's mesh and the first cell layer after the mapped boundary are unedited. The second cell layer of the EDEF region is a transition layer where each cell was divided into four according to the radial and angular directions. In the third layer, each cell was divided into two according to the axis direction. The mesh in this layer kept the topology of the original mesh with eight times more cells. The same refinement strategy was repeated for the second and third meshes. The three meshes presented in Table 4.5 were used to study STP sensitivity to the meshes in this multi-region approach.

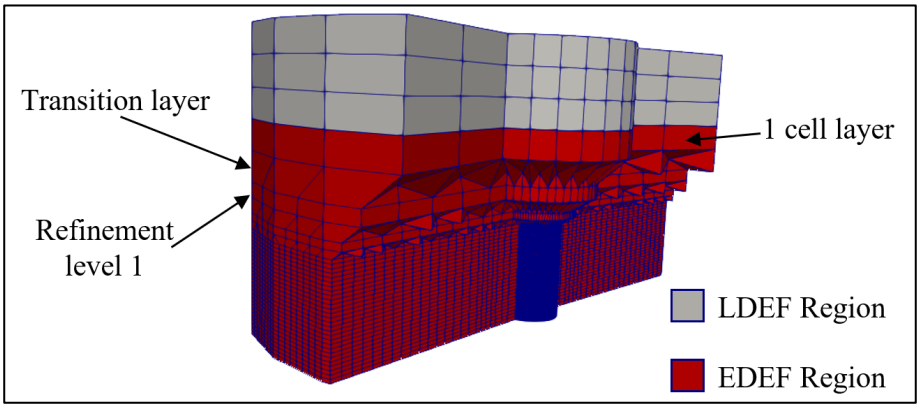

Figure 4.12: Mesh refinement architecture

Table 4.5 Multi -Region Grids

Mesh No.	Number of refinements	Cells number
Mesh 1	0 (medium mesh)	43 200
Mesh 2	1	184 320
Mesh 3	2	1 316 640

Equation (4.10) defines an error function, based on the STP reference values of the pure Lagrangian case (STP_{ref}).

$$error(m_i, t) = \frac{1}{\max\limits_{\text{time}}(STP_{ref}(t))} \left| STP(m_i, t) - STP_{ref}(t) \right| \tag{4.10}$$

Figure 4.13 presents the computed error for the three tested meshes. The error was null until 0.016 s because the spray was evolving only in the LDEF region.

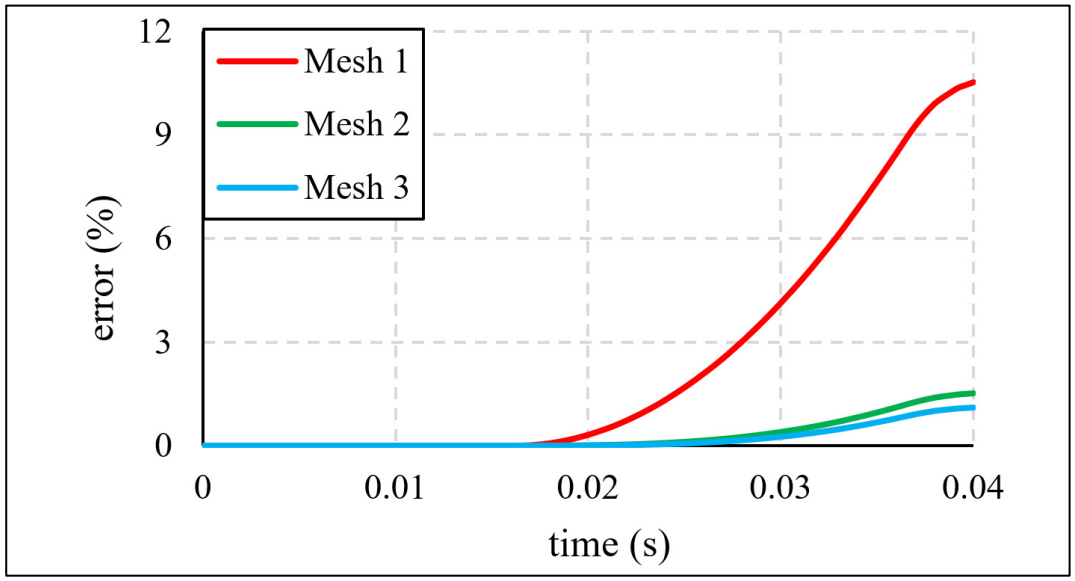

Figure 4.13 Muti-region model STP prediction error for the three tested meshes

After the spray reached the mapped boundary, the error function increased. For the mesh without refinement (Mesh 1), the error was remarkably higher than that for the other meshes.

The maximal errors for the three meshes were 10.4%, 1.50%, and 1.10%. The EDEF approach was more sensitive to the mesh than the LDEF approach.

Figure 4.14 presents three snapshots of the computed spray at three different times: 0.02 s, 0.03 s, and 0.04 s. The multi-region-computed spray (with two levels of refinement) is presented versus the Lagrangian spray (with a medium mesh and 10^6 parcel/s). The blue cells are in the EDEF region; the grey spheres are parcels in the LDEF region. The figure illustrates the agreement between the two computations for both the STP and the spreading angle.

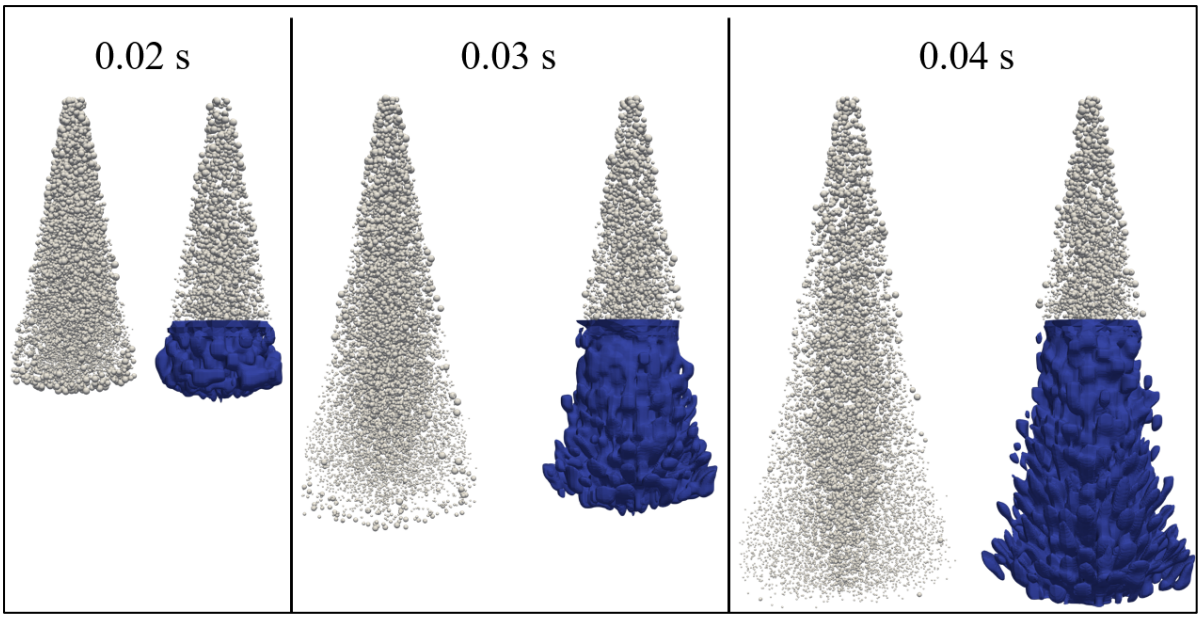

Figure 4.14 Spray evolution (Lagrangian versus multi-region)

4.5.2 Permeability Coefficient Calibration

The extended enthalpy–porosity technique was used to model the ice melting (Ernez & Morency, 2021a). The Darcy law defines a permeability coefficient to approximate the velocity damping in the mushy region. The predicted thermal field depends on the permeability coefficient values (Prakash & Voller, 1989).

The permeability coefficient (Cu) appears in the momentum equation as a source term $\left(\boldsymbol{S} = -Cu \cdot \frac{\delta^2}{(1-\delta)^3+q}\,\boldsymbol{u}\right)$, where δ is the solid fraction. If $\delta = 0$, the source term vanishes. If $\delta = 1$, the source term is equal to $\left(\frac{-Cu}{q}\boldsymbol{u}\right)$, where $q = 10^{-3}$ is a model coefficient to avoid division by 0, but small enough for the source term to dominate other terms in the momentum equation, giving ($\boldsymbol{u} = \boldsymbol{0}$). In the mushy region ($0 < \delta < 1$), the permeability coefficient directly affects the velocity's predicted value.

The methodology suggested in (Ebrahimi et al., 2019) for the original enthalpy–porosity technique was used to calibrate the permeability coefficient, requiring adjustment of the permeability coefficient for every set of boundary conditions. This methodology had been used to calibrate the permeability coefficient of the extended enthalpy–porosity technique in 2D (Ernez & Morency, 2021a). Because the present paper deals with 3D computations and a new set of boundary conditions, a recalibration was needed.

4.5.2.1 Test Case Setup and Meshes

The test case was a flat plate decontamination based on the spray parameters presented in subsection 0 The computational domain consisted of a square cuboid ($45\mathrm{D} \times 45\mathrm{D} \times 38\mathrm{D}$). The upper and lateral patches were set to be atmospheric outlets, and the lower patch was a wall. The nozzle outlet was placed at $27\mathrm{D}$ (approximately 1 m) from the wall. Figure 4.15 presents a crinkle clip of the coarse mesh. The domain was meshed using cubic cells of $4/3\mathrm{D}$ edges. The mesh was then refined twice to obtain a cell size of $\mathrm{D}/3$ surrounding the liquid flow. The lateral boundaries were located at 8.5D, far enough from the contaminated area to avoid the reflective effects of boundary conditions. The mapped boundary was set at 4D from the wall. The LDEF cells are shown in red and the EDEF cells in grey. An ice cylinder, with a diameter of $28\mathrm{D}$ and a height (thickness) of $2/3\mathrm{D}$ (Figure 4.16), was located at the wall center at the start of the calculations.

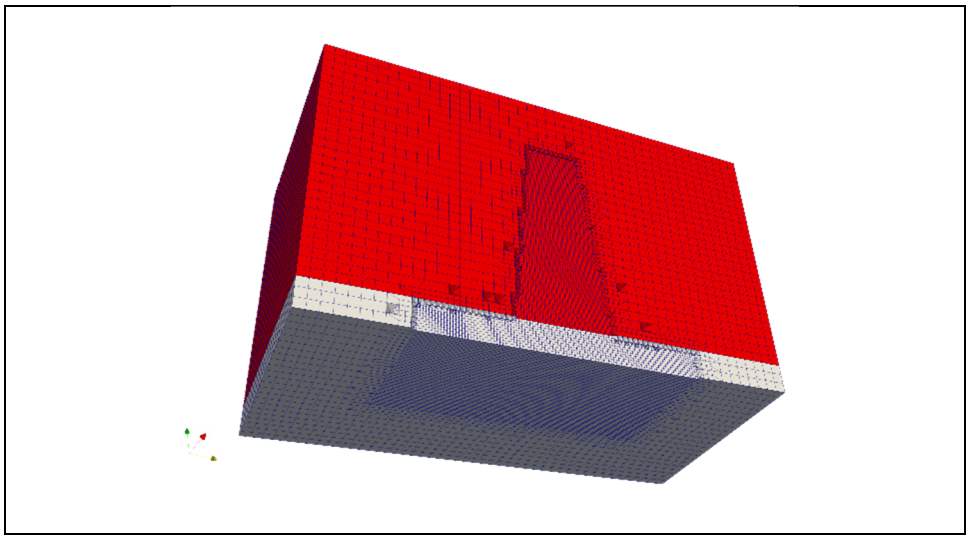

Figure 4.15 Coarse mesh clip of the flat plate decontamination test case

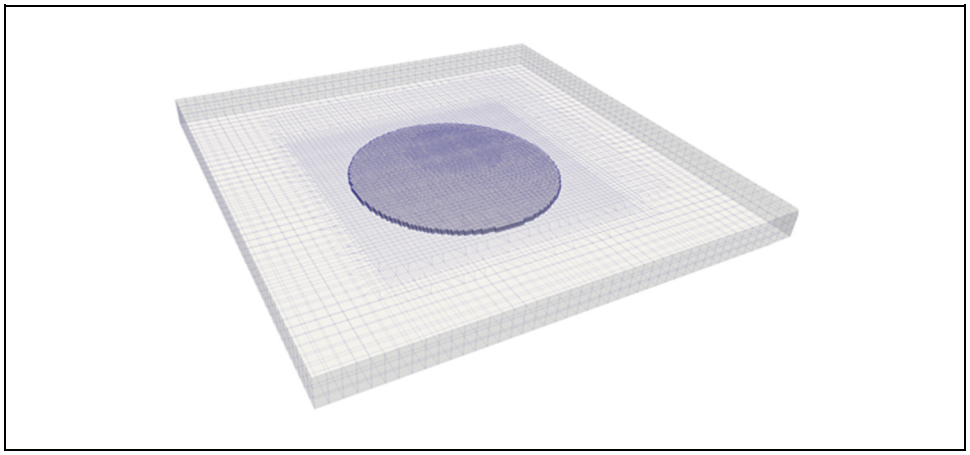

Figure 4.16 Ice zone in the EDEF region

From the calibration, the result of interest is the ice volume's change over time. Four meshes and four permeability coefficient values were tested for the calibration. The different meshes were obtained by refinement around the icy zone cells. The cell edges were divided by two, such that the cell edges were D/3, D/6, D/12, and D/24 for the coarse, medium, fine, and extra-fine meshes, respectively. For the permeability coefficient, values in the literature range between 10^3 and 10^{15} kg s^{-1} m^{-3}. However, values between 10^4 and 10^8 are often applied (Ebrahimi et al., 2019). In this study, four values ($10^4, 10^5, 10^6,$ and 10^7) were tested.

4.5.2.2 Results and Analysis

The effects of the mesh and the permeability coefficient on the ice volume evolution are presented. The ice volume $V_{ice}(t)$ is defined in Equation (4.11) as the summation of the ice volume over the computational domain:

$$V_{ice}(t) = \sum_{cells} V_{cell} \cdot \delta_{cell}(t) \tag{4.11}$$

where V_{cell} is a cell volume and $\delta_{cell}(t)$ is the ice volume fraction in a cell at time t.
The normalized ice volume is computed with equation (4.12).

$$\bar{V}_{ice}(t) = 100 \cdot \frac{V_{ice}(t)}{V_{ice}(0)} \tag{4.12}$$

All the computations were performed for 4 s (physical time). This duration is fixed based on the computations on the coarse mesh and a permeability coefficient of 10^6 kg s^{-1} m^{-3}, which is the calibrated value for the 2D computations (Ernez & Morency, 2021a). Figure 4.17 presents the ice volume evolution for the reference case. The flat plate was fully decontaminated after 3.32 s of injection time.

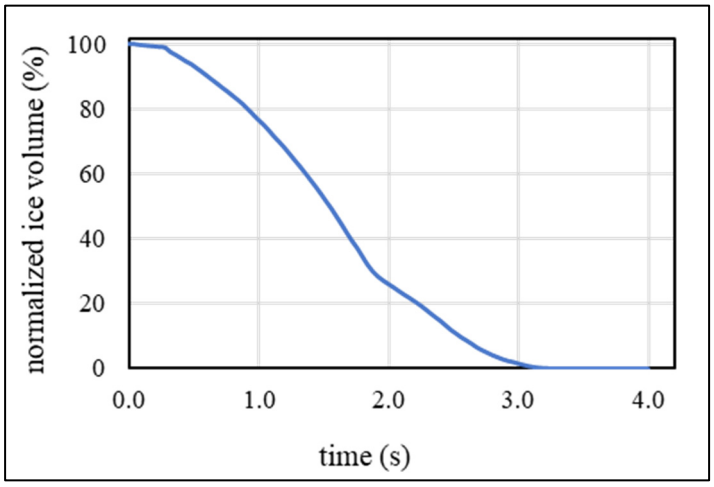

Figure 4.17 Ice volume evolution (reference case)

4.5.2.3 Grid sensitivity

For the grid sensitivity study, a grid-induced error (E_m) is defined as a function of the permeability coefficient (Cu_i) and the mesh (m_j) in equation (4.13).

$$E_m(Cu_i, m_j) = \frac{1}{\text{total time}} \int_{time} \left| \bar{V}_{ice}(Cu_i, m_{j+1}) - \bar{V}_{ice}(Cu_i, m_j) \right| \tag{4.13}$$

Figure 4.18 presents the grid-induced error for the four tested permeability coefficients. The computation results were more sensitive to the mesh for the higher permeability coefficients. Except for the permeability coefficient of 10^7, the grid-induced error was lower than 3% for the medium mesh. For the fine mesh, the permeability coefficients of 10^5 and 10^6 gave errors of 0.26% and 0.34%, respectively. The permeability coefficients of 10^4 and 10^7 generated errors of 1.23% and 1.29%, respectively.

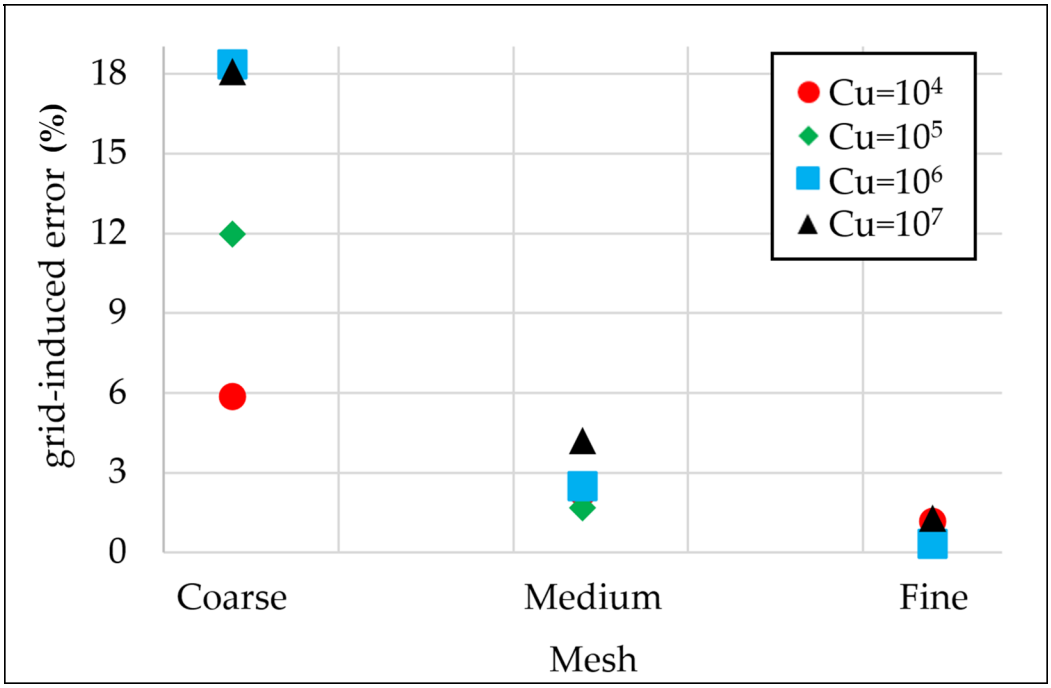

Figure 4.18 Ice volume evolution sensitivity to the mesh quality for the four tested permeability coefficients

In the engineering context, a grid-induced error of 3% is acceptable. For the fine mesh, the grid induced error for the four tested permeability coefficients was acceptable. The fine mesh is mandatory to ensure a grid-induced error below 3% for a permeability coefficient of 10^7. The best compromise between accuracy and computation cost could be found in the medium mesh and a permeability coefficient of 10^5. This setup had a grid-induced error of only 1.66%. Furthermore, for faster computations and model simplicity, the evaporation in the LDEF region could be neglected since only 0.27% of the injected mass evaporated.

4.5.2.4 Permeability coefficient sensitivity

The instantaneous variance of the normalized ice volume, computed with equation (4.14), assesses the permeability coefficient sensitivity. The distance to the mean value, $d(Cu_i, m_j, t)$, is computed with equation (4.15).

$$\sigma^2(m_j, t) = \frac{\sum_{i=1}^{4} d^2(Cu_i, m_j, t)}{3} \tag{4.14}$$

$$d(Cu_i, m_j, t) = \bar{V}_{ice}(Cu_i, m_j, t) - \sum_{k=1}^{4} \left(\frac{\bar{V}_{ice}(Cu_k, m_j, t)}{4} \right) \tag{4.15}$$

Figure 4.19 presents the normalized ice volume variance for the four meshes. The overall variance $\left(\int_t \sigma^2(m_j, t)\, dt \right)$ decreased with mesh refinement. The ice volume was less sensitive to the permeability coefficient for the finer meshes, as presented in (Ebrahimi et al., 2019). The maximum variances for the fine and extra-fine meshes were 3.32% and 0.02%, respectively. Results for the extra-fine mesh were almost insensitive to the permeability coefficient.

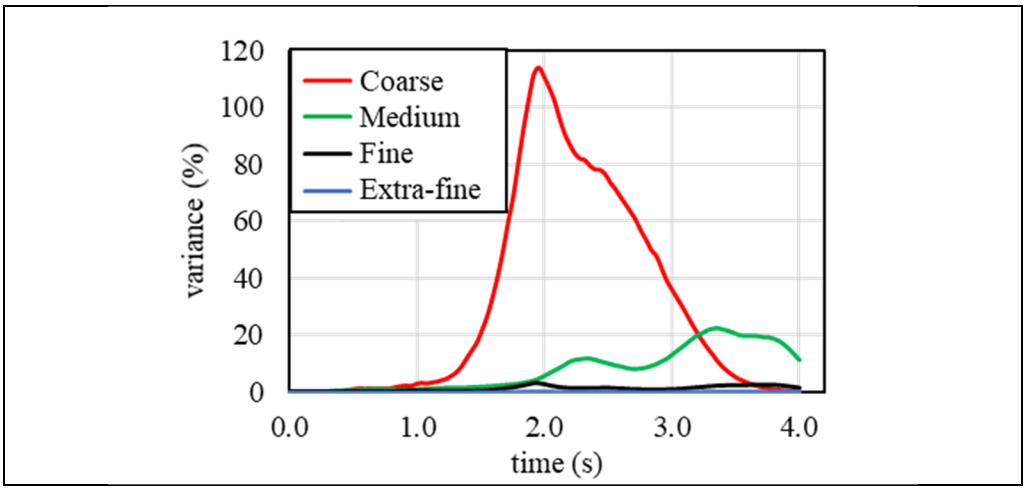

Figure 4.19 Normalized ice volume variance for the different meshes

Table 4.6 summarizes the average distance to the mean value and helps selecting a case setup. This average distance is defined as the temporal average of the distance defined by equation (4.15).

Table 4.6 Average distance to the mean values for different meshes

	$Cu = 10^4$	$Cu = 10^5$	$Cu = 10^6$	$Cu = 10^7$
Coarse	12.68	3.23	5.73	29.69
Medium	5.27	0.10	1.52	7.60
Fine	0.40	0.14	0.41	1.13
Extra-fine	0.08	0.11	0.40	0.76

For all meshes, a permeability coefficient of 10^5 represented the smallest distance. For a medium mesh with a permeability coefficient of 10^5, the grid-induced error was 1.66%. A suitable compromise between computer time and accuracy was reached with a permeability coefficient of 10^5 using a medium mesh.

4.6 Conclusion

A new OpenFOAM-V6 based solver ($AGDFoam$) has been developed and verified to simulate the AGD process. The new solver is a combination of the native solver ($sprayFoam$) and the ($AGDEulerFoam$) solver developed in (Ernez & Morency, 2021a). The new solver has been designed for simulating the AGD process in 3D. In this paper, a set of injection parameters is proposed on the basis of a technical review. A computational domain divided into two regions enabled the simulations. The first region was designed for the spray evolution far from the wall, and the spray evolution was solved using a Lagrangian approach. The flow in the second region was modelled with the Eulerian approach. The second region was designed to model the ice decontamination. For the multi-region approach, the momentum conservation was verified through a spray-tip penetration (STP) test case. The STP sensitivity to the PR and the mesh was studied. The permeability coefficient of the extended enthalpy–porosity technique was then calibrated. For the proposed injection parameters, it was concluded that:

- Using a PR superior to 10^6 parcel/s brings the computations to independency from the mesh density in the Lagrangian region.
- Computations in the Eulerian region are more sensitive to the mesh density. The grid is acceptable for a mesh eight times finer than the medium mesh.
- A permeability coefficient of 10^5 $\mathrm{kg\,s^{-1}\,m^{-3}}$ gives a good prediction (2%) using a medium mesh. For enhanced accuracy, it is advised to multiply the number of mesh elements by eight to reach results that are almost insensitive to the permeability coefficient.

This paper is part of a research effort to design a CFD test bench for the AGD process. For the first time, this study used realistic injection parameters for the AGD spray. The multi-region approach conserved the STP evolution profile predicted using the Lagrangian solver, which verified the momentum transfer methodology applied between the two regions. Future works will focus on studying the influence of the spray parameters on the ice decontamination rate.

CONCLUSION

Les développements des méthodes numériques réalisés dans cette étude ont permis de simuler le processus de dégivrage au sol des aéronefs. Ces méthodes numériques ont été vérifiées via un solveur OpenFOAM développé durant cette thèse. Il est à noter qu'à notre connaissance, aucune méthode CFD n'est définie dans la littérature ouverte pour simuler l'évolution de la forme de la glace dans le processus de dégivrage au sol des aéronefs. Cette thèse présente de nouveaux modèles mathématiques et des méthodes numériques développés dans un cadre CFD open-source pour la simulation de dégivrage au sol des aéronefs.

Le procédé de dégivrage au sol des aéronefs par jet liquide est caractérisé par une dispersion d'échelle. Cette dispersion augmente significativement les coûts de calculs. Le premier article, présenté au CHAPITRE 2 s'est concentré sur cette problématique. Il propose un modèle eulérien-lagrangien qui réduit les coûts de calculs permettant ainsi l'investigation de l'influence des paramètres d'injection du liquide sur le transfert de chaleur au niveau de la surface à décontaminer. Le modèle repose sur une approche multi-région où deux régions sont définies. (i) la première région où le jet liquide (phase liquide) est défini par un nuage de particules lagrangiennes qui interagissent avec une seconde phase Eulérienne (phase gazeuse). (ii) la deuxième région est dédiée à l'évolution d'un film liquide. Le film liquide est alimenté par les particules lagrangiennes de la première région. Un maillage d'un volume de contrôle caractéristique du procédé de dégivrage au sol des aéronefs est vérifié. Le modèle est ensuite validé en deux étapes. La première est une validation des équations régnantes sur la première région avec une étude expérimentale de pénétration de la pointe de pulvérisation de (Mitroglou et al. 2006). Faute de disponibilité d'études expérimentales de jet liquide de dégivrage, le cas test consiste en une injection de carburant isooctane dans une chambre de combustion. Quatre séries de mesures sont générées avec deux pressions d'injection (120 bar et 200 bar) et deux pression de chambre (1 bar et 12 bar). Les écarts avec les résultats expérimentaux sont plus élevés avec la pression de chambre de 12 bar. Les écarts enregistrés pour la chambre à 12 bar sont de 17% et 20% pour, respectivement, les pressions d'injection de 120 bar et 200 bar. Les écarts enregistrés pour la chambre à 1 bar sont de 10% pour les

deux pressions d'injection. Les résultats avec la pression de chambre de 1 bar sont caractéristiques du jet de dégivrage puisque ce dernier évolue dans l'air ambiant. Une deuxième validation est élaborée évaluant l'exactitude du transfert de chaleur entre le film liquide et une surface plane. Les résultats numérique ont été comparés aux résultats expérimentaux de Stevens & Webb (1991) pour un nombre de Reynolds de 40800. Un écart maximal de 14% a été enregistré. Les effets du nombre de Reynolds, de la taille de gouttelettes, du débit massique et de l'angle d'inclinaison du jet sur le coefficient de transfert de chaleur convectif avec une surface plane ont été étudiés. Quatre nombres de Reynolds ont été testés $10^4, 2 \cdot 10^4, 6 \cdot 10^4$ et 10^5. En gardant la taille de particules fixe, le nombre de Reynolds n'influe pas sur le transfert de chaleur pour une valeur inférieure ou égale à $6 \cdot 10^4$. Cependant, une augmentation significative du transfert de chaleur convectif a été enregistré pour le nombre de Nusselt de 10^5. Le transfert de chaleur augmente avec l'augmentation du débit massique ou avec la réduction des tailles de gouttelettes. Finalement, incliner le jet par rapport à la normale de la surface augmente significativement le transfert de chaleur au niveau de la zone de stagnation.

Un nouveau solveur développé sous OpenFOAM-V6 est proposé dans le deuxième article décrit dans le CHAPITRE 3. Le solveur résout des problèmes caractérisés par deux phases (liquide/gaz) dispersées l'une dans l'autre. Deux contributions majeures à la modélisation numérique du procédé de dégivrage au sol sont présentées dans cet article. (i) La modélisation de la phase liquide comme étant un mélange homogène de deux liquides différents. Cette caractéristique est propre au procédé de dégivrage au sol des aéronefs, où les liquides de dégivrage sont mélangés à l'eau issue de la fusion du givre. La modélisation du mélange permet de mettre à jour les propriétés thermo-physiques de la phase liquide. (ii) Le couplage du modèle de la phase liquide à un modèle de changement de phase (fusion / solidification). Ce couplage permet de définir implicitement une troisième phase solide qui est transférée à la phase liquide sous des conditions définies. Le nouveau solveur est basé sur un solveur natif à OpenFOAM-V6. Pour la modélisation de la miscibilité (liquide de dégivrage / eau), une équation de transport d'espèces a été implémentée. Les propriétés thermo-physiques de la phase liquide sont mises à jour suivant la règle des mélanges à chaque itération. Concernant le modèle de changement de phase, la technique d'enthalpie-

porosité, originalement proposée pour les problème liquide-solide, est étendue pour gérer le changement de phase dans les écoulements gaz-liquide-solide. Les résultats principaux présentés dans cet article sont résumés ci-dessous :

1- Le solveur développé prédit l'évolution instationnaire de la température d'un écoulement diphasique dans lequel une phase est un mélange de deux espèces avec une exactitude de 95%. Cette exactitude est observée dans une simulation 2D de rupture de barrage impliquant un mélange.
2- Le solveur proposé prédit le transfert de chaleur convectif entre le liquide formé par un jet incident et une paroi chauffée avec une erreur maximale de 12 % pour un nombre de Reynolds de 10 600. Ce résultat est comparable aux modèles CFD existants.
3- Le coefficient de perméabilité de la technique d'enthalpie-porosité étendue est calibré par une étude de sensibilité proposée dans (Ebrahimi et al., 2019). Les résultats sont insensibles au coefficient de perméabilité avec un maillage extra-fin. L'évolution de la forme de la glace peut être bien prédite avec un maillage grossier avec un coefficient de perméabilité de 10^6, qui se situe dans l'intervalle indiqué par (Ebrahimi et al., 2019).

Le troisième article présenté dans le CHAPITRE 4 est le fruit de la combinaison des méthodes des deux premiers articles. Un nouveau solveur multi-région est développé combinant le modèle de jet lagrangien étudié dans premier article et le modèle d'écoulement multiphasique dispersé développé dans le deuxième article. Le domaine de calcul est divisé en deux régions, (i) une première région conçue pour l'évolution du spray loin de la surface à décontaminer où l'évolution du spray est résolue par une méthode lagrangienne présentée dans le premier article et (ii) une deuxième région qui modélise la contamination du givre moyennant la méthode eulérienne présentée dans le deuxième article. Le nouveau solveur est conçu pour la simulation du procédé de dégivrage au sol des aéronefs. Une revue technique a été établie dans cet article visant à définir un domaine de calcul ainsi que des conditions d'injection du jet de dégivrage. La sensibilité de la pénétration de la pointe du jet au débit de

particules est étudiée. Le coefficient de perméabilité de la technique d'enthalpie-porosité étendue est calibré. Les résultats majeurs de cet article se résument en trois points :

- Un débit de particule supérieur à 10^6 particule/seconde assure une indépendance de la densité du maillage dans la région lagrangienne.
- Les calculs dans la région eulérienne sont plus sensibles à la densité du maillage. L'insensibilité au maillage n'est atteinte que pour un maillage 8 fois plus fin que le maillage moyen, utilisé dans la région lagrangienne.
- Un coefficient de perméabilité de 10^5 $kg \cdot s^{-1} m^{-3}$ assure une prédiction à 2% près de la vitesse de décontamination tout en utilisant un maillage moyen. Multiplier 8 fois le nombre d'éléments du maillage assure des résultats insensibles au coefficient de perméabilité.

Cet article est le premier en son genre à présenter une méthode CFD spécialement conçue pour étudier le procédé de dégivrage au sol des aéronefs avec des paramètres d'injection réalistes (voir tableau 4.2).

Cette thèse répond aux questions de la problématique de recherche posées à la section 0.3,

(i) Un modèle multiphasique particulaire (Lagrangien) est plus adéquat à modéliser le liquide de dégivrage.

(ii) Pour modéliser dans le même volume de contrôle la fusion du givre en eau qui est soluble dans la solution d'ADF, une extension de la technique enthalpie-porosité a été développée permettant à simuler la fonte dans un volume de contrôle contenant trois phases (solide/liquide/gaz). Cette technique est alliée à un modèle multiphasique particulaire (eulérien) où une équation de diffusion modélisant la miscibilité entre l'eau et l'ADF est implémentée.

(iii) La propagation du jet et l'évolution de la forme de givre à la suite du transfert de chaleur sont couplées dans le même volume de contrôle grâce à un modèle à deux régions. À l'interface qui lie les deux régions, les champs Lagrangiens sont convertis en champs Eulérien.

Le premier article a servi à démontrer l'aptitude de l'approche Eulérienne-Lagrangienne à simuler un jet dispersé caractéristique du procédé de dégivrage au sol des aéronefs. Le deuxième article a comblé un manque dans la littérature en présentant un modèle de changement de phase où le givre fond dans un volume de contrôle contenant de l'air et un liquide miscible avec l'eau. Au départ le liquide est dispersé dans la phase gazeuse. Le troisième article, quant à lui, combine les deux premiers dans un solveur multi-régions permettant ainsi de simuler le procédé liant l'évolution de la forme du givre au paramètre du jet liquide. Le code développé est validé seulement en partie à cause d'un manque remarquable des données expérimentales. Cependant, ce travaille souligne un intérêt d'investissement dans ce domaine d'application. Une des retombées directes prévus de ce travail de recherche est de solliciter des études expérimentales du procédé. Ces études auront des effets directs sur la méthode d'application de l'ADF dans les aéroports. Aussi, ils augmenteront la fiabilité des codes de calculs dans l'optique d'explorer de nouveaux scénarios de dégivrage jusqu'à permettre la robotisation du procédé.

ANNEXE I

TEMPS DE CALCULS DES DIFFERENTES SIMULATIONS

Cette annexe rassemble les temps de calculs des différentes simulations donnant au lecteur une idée sur l'ordre de grandeur des différente simulations présentées dans le présent manuscrit. Le tableau ci-dessous présente les cas test avec leurs configurations valides (maillage, débit de particule et coefficient de perméabilité).

Tableau A.1 Temps de calculs

Simulation	Chapitre	Ressources*	Temps simulée	Temps de calcul
Jet impactant	2	8 cœurs	1s	2h
Jet libre	2	1 cœur	0.5ms	15min
Test diffusion	3	1 cœur	50s	20s
Test énergie	3	1 cœur	45s	5min
Jet impactant	3	1 cœur	40ms	40min
Calibration	3	1 cœur	0.25s	5h30min
Jet libre lagrangien	4	1 cœur	40ms	20min
Jet libre multi-région	4	1 cœur	40ms	1h30min
Calibration	4	8 cœurs	4s	4jours

* Processeur : Intel Core i9-9900KF, 8 cœurs, 16 threads, 3.6 GHz (Turbo 5GHz), cache 16 MB L3, LGA1151, 95W.

LISTE DE RÉFÉRENCES BIBLIOGRAPHIQUES

ACRP Fact Sheets. (2016). *De/Anti-Icing Optimization*. Transportation Research Board of the National Academies, sponsored by the FAA. Repéré à http://onlinepubs.trb.org/onlinepubs/acrp/acrp_rpt_045factsheets.pdf

Al-Khalil, K., & Potapczuk, M. (1993). Numerical modeling of anti-icing systems and comparison to test results on a NACA 0012 airfoil. Dans *31st Aerospace Sciences Meeting, Aerospace Sciences Meetings*. Reno,NV,U.S.A. https://doi.org/10.2514/6.1993-170

Beaugendre, H., Morency, F., & Habashi, W. G. (2006). Development of a second generation in-flight icing simulation code. *Journal of Fluids Engineering, Transactions of the ASME*, *128*(2), 378-387. https://doi.org/10.1115/1.2169807

Bertrand, O., Binet, B., Combeau, H., Couturier, S., Delannoy, Y., Gobin, D., Vieira, G. (1999). Melting driven by natural convection a comparison exercise: First result. *International Journal of Thermal Sciences*, *38*(1), 5-26. https://doi.org/10.1016/S0035-3159(99)80013-0

Bilodeau, D. R., Habashi, W. G., Baruzzi, G. S., & Fossati, M. (2016). Numerical Modeling of First and Second Order SLD Effects on 3D Geometries. Dans *8th AIAA Atmospheric and Space Environments Conference* (pp. 1-23). Reston, Virginia : American Institute of Aeronautics and Astronautics. https://doi.org/10.2514/6.2016-3280

Bourgault, Y., Habashi, W. G., Dompierre, J., & Baruzzi, G. S. (1999). A finite element method study of Eulerian droplets impingement models. *International Journal for Numerical Methods in Fluids*, *29*(4), 429-449. https://doi.org/10.1002/(SICI)1097-0363(19990228)29:4<429::AID-FLD795>3.0.CO;2-F

Cantin, S., Morency, F., & Garnier, F. (2018). Numerical simulation of contrail ice particle growth in the near field of an aircraft engine. Dans *Global Power and Propulsion Society* (Vol. 18, pp. 1-8). https://doi.org/10.5281/zenodo.1344610

Chen, B., Wang, L., Gong, R., & Wang, S. (2016). Numerical simulation and experimental validation of aircraft ground deicing model. *Advances in Mechanical Engineering*, *8*(5), 1-15. https://doi.org/10.1177/1687814016646976

Chigier, N., & Reitz, D. R. (1996). Regimes of Jet Breakup and Breakup Mechanisms (Physical Aspects). Dans *Recent Advances in Spray Combustion: Spray Atomization and Drop Burning Phenomena* (pp. 109-135). Washington DC : American Institute of Aeronautics and Astronautics. https://doi.org/10.2514/5.9781600866418.0109.0135

Desjardins, O., Moureau, V., & Pitsch, H. (2008). An accurate conservative level set/ghost fluid method for simulating turbulent atomization. *Journal of Computational Physics*, *227*(18), 8395-8416. https://doi.org/10.1016/j.jcp.2008.05.027

Dianat, M., Skarysz, M., & Garmory, A. (2017). International Journal of Multiphase Flow A Coupled Level Set and Volume of Fluid method for automotive exterior water management applications, *91*, 19-38. https://doi.org/10.1016/j.ijmultiphaseflow.2017.01.008

Dukowicz, J. K. (1980). A Particle-Fluid Numerical Model for Liquid Sprays. *Journal of Computational Physics*, *35*, 229-253. https://doi.org/https://doi.org/10.1016/0021-9991(80)90087-X

Durst, F., Milojevic, D., & Schönung, B. (1984). Eulerian and Lagrangian predictions of particulate two- phase flows : a numerical study. *Applied Mathematical Modelling*, *8*(2), 101-115. https://doi.org/10.1016/0307-904X(84)90062-3

Ebrahimi, A., Kleijn, C. R., & Richardson, I. M. (2019). Sensitivity of numerical predictions to the permeability coefficient in simulations of melting and solidification using the enthalpy-porosity method. *Energies*, *12*(22). https://doi.org/10.3390/en12224360

Edelbauer, W., Zhang, D., Kopun, R., & Stauder, B. (2016). Numerical and experimental investigation of the spray quenching process with an Euler-Eulerian multi-fluid model. *Applied Thermal Engineering*, *100*, 1259-1273. https://doi.org/10.1016/j.applthermaleng.2016.02.131

Edin, B., & Šefko, Š. (2015). Computational Modeling and Simulation of Nonisothermal Free-surface Flow of a Liquid Jet Impinging on a Heated Surface. *Procedia Engineering*, *100*, 115-124. https://doi.org/10.1016/j.proeng.2015.01.349

Ernez, S., & Morency, F. (2018). Heat Transfer Study in Aircraft Ground Deicing by Liquid Jets with a Eulerian-Lagrangian CFD Model. Dans *CFD2018-The 26th Annual Conference of the Computational Fluid Dynamics Society of Canada* (p. 8). Montréal.

Ernez, S., & Morency, F. (2019a). A Multi-region CFD Model for Aircraft Ground Deicing by Liquid Sprays. Dans *The 27th Annual Conference of the Computational Fluid Dynamics Society of Canada.* Western University, London, ON.

Ernez, S., & Morency, F. (2019b). Eulerian-Lagrangian CFD Model for Aircraft Ground Deicing by Liquid Sprays. Dans *The 64th Aeronautics Conference of the Canadian Aeronautics and Space Institute.* Sheraton Laval, Montréal, Québec.

Ernez, S., & Morency, F. (2019c). Eulerian-Lagrangian CFD Model for Prediction of Heat Transfer Between Aircraft Deicing Liquid Sprays and a Surface. *International Journal of Numerical Methods for Heat & Fluid Flow*, *29*(7), 2450-2475. https://doi.org/10.1108/HFF-09-2018-0534

Ernez, S., & Morency, F. (2021a). CFD Model for Aircraft Ground Deicing: Verification and Validation of an Extended Enthalpy-Porosity Technique in Particulate Two Phase Flows. *Fluids*, *6*(6), 210. https://doi.org/10.3390/fluids6060210

Ernez, S., & Morency, F. (2021b). Multi-region CFD Method for Simulating Aircraft Ground Deicing by Dispersed Liquid Sprays. Dans *The 29th Annual Conference of the Computational Fluid Dynamics Society of Canada.* Memorial University, Zoom Webinar.

Ernez, S., & Morency, F. (2022). A Multi-Region CFD Model for Aircraft Ground Deicing by Dispersed Liquid Spray. *Energies*, *15*(17). https://doi.org/10.3390/en15176220

FAA. (2010). *Standardized International Aircraft Ground Deice Program (SIAGDP)*. Repéré à https://www.faa.gov/other_visit/aviation_industry/airline_operators/airline_safety/deicing/media/standardized_international_ground_deice_program.pdf

Ferziger, J. H., Perić, M., & Street, R. L. (2020). *Computational Methods for Fluid Dynamics* (4e éd.). Gewerbestrasse, Cham, Switzerland : Springer, Cham. https://doi.org/10.1007/978-3-319-99693-6

Fotovat, F., Bi, X. T., & Grace, J. R. (2017). Electrostatics in gas-solid fluidized beds: A review. *Chemical Engineering Science*, *173*(August), 303-334. https://doi.org/10.1016/j.ces.2017.08.001

Gibou, F., Fedkiw, R., & Osher, S. (2018). A review of level-set methods and some recent applications. *Journal of Computational Physics*, *353*, 82-109. https://doi.org/10.1016/j.jcp.2017.10.006

Gopala, V. R., & van Wachem, B. G. M. (2008). Volume of fluid methods for immiscible-fluid and free-surface flows. *Chemical Engineering Journal*, *141*(1-3), 204-221. https://doi.org/10.1016/j.cej.2007.12.035

Gouesbet, G., & Berlemont, A. (1999). Eulerian and Lagrangian approaches for predicting the behaviour of discrete particles in turbulent flows. *Progress in Energy and Combustion Science*, *25*(2), 133-159. https://doi.org/10.1016/S0360-1285(98)00018-5

Greenshields, C. J. (2015). OpenFOAM programmer's guide v3.0.1. *OpenFOAM Foundation Ltd.*, (December), 100. Repéré à http://foam.sourceforge.net/docs/Guides-a4/ProgrammersGuide.pdf

Greenshields, C. J. (2017). *OpenFOAM User Guide V5*. *OpenFOAM Foundation Ltd*. England : OpenFOAM Foundation Ltd. Repéré à http://foam.sourceforge.net/docs/Guides-a4/OpenFOAMUserGuide-A4.pdf

Groulx, D., & Lacroix, M. (2006). Study of close contact melting of ice from a sliding heated flat plate, *49*, 4407-4416. https://doi.org/10.1016/j.ijheatmasstransfer.2006.05.007

Habchi, C., Foucart, H., & Baritaud, T. (1999). Influence of the wall temperature on the mixture preparation in DI gasoline engines. *Oil and Gas Science and Technology*, *54*(2), 211-222. https://doi.org/10.2516/ogst:1999017

Haider, A., & Levenspiel, O. (1989). Drag coefficient and terminal velocity of spherical and nonspherical particles. *Powder Technology*, *58*(1), 63-70. https://doi.org/10.1016/0032-5910(89)80008-7

Hermosilla, M. B. (2016). *Study of heat and mass transfer applications in the field of engineering by using OpenFOAM*. Universitat Politècnica de Catalunya. Repéré à https://upcommons.upc.edu/bitstream/handle/2117/98893/REPORT_260.pdf?sequence=2&isAllowed=y

Hirt, C. W., & Nichols, B. D. (1981). Volume of fluid (VOF) method for the dynamics of free boundaries. *Journal of Computational Physics*, *39*(1), 201-225. https://doi.org/10.1016/0021-9991(81)90145-5

Holzmann, T. (2017). *Mathematics, Numerics, Derivations and OpenFOAM®*. Leoben, Austria : Tobias Holzmann. https://doi.org/10.13140/RG.2.2.27193.36960

ICAO. (2018a). *International Standards and Recommended Practices : Annex 6 - Operation Of Aircraft - Part 1 - International Commercial Air Transport - Aeroplanes : paragraph 4.3.5.4*. Repéré à https://store.icao.int/en/annex-6-operation-of-aircraft-part-i-international-commercial-air-transport-aeroplanes

ICAO. (2018b). *Manual of Aircraft Ground De-Icing / Anti-Icing Operations*. Repéré à https://store.icao.int/en/manual-of-aircraft-ground-de-icing-anti-icing-operations-doc-9640

Ignatowicz, K., & Morency, F. (2017). Numerical Study of Ice Particle Shedding: Interpolation Methods and 2D Trajectories. Dans *CASI: 63rd Aeronautics Conference*. Toronto. Repéré à https://www.researchgate.net/publication/321718824_Numerical_Study_Of_Ice_Particle_Shedding_Interpolation_Methods_And_2D_Trajectories

Incropera, F. P., DeWitt, D. P., Bergman, T. L., & Lavine, A. S. (2006). *Fundamentals of Heat and Mass Transfer*. *John Wiley & Sons, Inc.* (6^{e} éd.). Jefferson City : Wiley. Repéré à https://books.google.com.sa/books?id=Xup3PgAACAAJ

Kampili, M. (2017). Implementation of decay heat model as a submodel in lagrangian library for reactingParcelFoam solver. Dans *Proceedings of CFD with OpenSource Software, 2017*. https://doi.org/http://dx.doi.org/10.17196/OS_CFD#YEAR_2017 CFD

Kolev, N. I. (2012). *Multiphase Flow Dynamics 2*. *Mechanical Interactions* (4e éd.). Berlin, Heidelberg : Springer-Verlag Berlin Heidelberg. https://doi.org/10.1007/978-3-642-20598-9

Li, Y. (2016). Implementation of multiple time steps for the multi-physics solver based on chtMultiRegionFoam. Dans *CFD with OpenSource Software, Edited by Nilsson. H.* Repéré à http://www.tfd.chalmers.se/~hani/kurser/OS_CFD_2016

Lin, S. P., & Reitz, R. D. (1998). Drop and Spray Formation From A Liquid Jet. *Annu. Rev. Fluid Mech*, *30*, 85-105. https://doi.org/10.1146/annurev.fluid.30.1.85

Ling, K., Li, Z., Sun, D., He, Y., & Tao, W. (2015). Computers & Fluids A three-dimensional volume of fluid & level set (VOSET) method for incompressible two-phase flow. *COMPUTERS AND FLUIDS*, *118*, 293-304. https://doi.org/10.1016/j.compfluid.2015.06.018

Liu, A., Mather, D., & Reitz, R. D. (1993). Modeling the Effects of Drop Drag and Breakup on Fuel Sprays. Dans *International Congress and Exposition*. Detroit, Michigan : SAE TECHNICAL PAPER SERIES 930072. https://doi.org/10.4271/930072

Liu, H.-T., & Hua, J. (2004). Three-Dimensional Integrated Thermodynamic Simulation for Wing Anti-Icing System. *Journal of Aircraft*, *41*(6). https://doi.org/10.2514/1.5594

Liu, X., Gabour, L. A., & Lienhard, J. H. (1993). Stagnation-Point Heat Transfer During Impingement of Laminar Liquid Jets: Analysis Including Surface Tension. *Journal of Heat Transfer*, *115*(1), 99. https://doi.org/10.1115/1.2910677

Ma, Z. W., Zhang, P., Wang, R. Z., Furui, S., & Xi, G. N. (2010). Forced flow and convective melting heat transfer of clathrate hydrate slurry in tubes. *International Journal of Heat and Mass Transfer*, *53*(19-20), 3745-3757. https://doi.org/10.1016/j.ijheatmasstransfer.2010.04.025

Manni, A. (2014). An introduction to twoPhaseEulerFoam with addition of an heat exchange model. Dans *CFD with OpenSource Software*. Gothenburg, Sweden. Repéré à http://www.tfd.chalmers.se/~hani/kurser/OS_CFD_2014/Alessandro Manni/ReportAM.pdf

Marquis, P. (2007). *Sécurité aérienne — nouvelles*. Ottawa : Transport Canada. Repéré à https://www.tc.gc.ca/media/documents/ac-publications/tp185f_4_2007.pdf

Marschall, H. (2011). *Towards the Numerical Simulation of Multi-Scale Two-Phase Flows*. Technische Universität München. Repéré à https://mediatum.ub.tum.de/doc/1080878/1080878.pdf

Meredith, K. (2010). *Thin Liquid Film Modeling in OpenFOAM*. *5th OpenFOAM Workshop*. Gothenburg, Sweden. Repéré à http://web.student.chalmers.se/groups/ofw5/Abstracts/KarlMeredithAbstractOFW5.pdf

Mironova, M. (2018). *Numerical Study of Steady State and Transient Heat Conduction using OpenFOAM*. Montanuniversität Leoben. Repéré à https://pure.unileoben.ac.at/portal/files/3161767/AC15203764n01.pdf

Mitroglou, N., Nouri, J. M., Gavaises, M., & Arcoumanis, C. (2006). Spray characteristics of a multi-hole injector for direct-injection gasoline engines. *International Journal of Engine Research*, *7*(3), 255-270. https://doi.org/10.1243/146808705X62922

Morency, F., Tezok, F., & Parashivoiu, I. (2000). Heat and Mass Transfer in the Case of Anti-Icing System Simulation. *Journal of Aircraft*, *37*(2), 245-252. https://doi.org/10.2514/2.2613

Moshansky, P. (1992). *Commission of inquiry into the Air Ontario crash at Dryden, Ontario: Final Report: Technical Appendices*. *Canadian Cataloguing in Publication Data*. Ottawa. Repéré à https://publications.gc.ca/collections/collection_2014/bcp-pco/CP32-55-1-1992-1-eng.pdf

Nasr, G. G., Yule, A. J., & Bendig, L. (2002). *Industrial Sprays and Atomization*. London : Springer London. https://doi.org/10.1007/978-1-4471-3816-7

National Transportation Safety Board. (1993). *Aircraft Accident Report Washington, D.C. 20594 AIRCRAFT, Takeoff stall in icing Conditions USAIR flight 405 FOKKER F-28, New York March 22,1992*. Washington DC : National Transportation Safety Board. Repéré à http://www.ntsb.gov/investigations/AccidentReports/Reports/AAR0003.pdf

NEXTfoam. (2017). *Boundary Conditions - OpenFOAM-4.1*. Geumcheon-gu, Seoul : Open Source CFD Consulting. Repéré à http://www.nextfoam.co.kr/lib/download.php?idx=135228&sid=235c1d3fc28364657dbb43ccfe025b25

Nijdam, J. J., Guo, B., Fletcher, D. F., & Langrish, T. A. G. (2006). Lagrangian and Eulerian models for simulating turbulent dispersion and coalescence of droplets within a spray. *Applied Mathematical Modelling*, *30*(11), 1196-1211. https://doi.org/10.1016/j.apm.2006.02.001

NIST. (1998). JANAF Thermochemical Tables. *NIST Standard Reference Database 13*. https://doi.org/10.18434/T42S31

Nobile, M. (2015). *Improvement of Lagrangian approach for multiphase flow*. Göteborg, Suède. Repéré à http://www.tfd.chalmers.se/~hani/kurser/OS_CFD_2014/Matteo Nobile/RevisedReport_MatteoNobile.pdf

Noriega, H. (2016). *Une étude de cas de vérification pour un code à source ouvert de simulation numérique*. Université de Montréal. Repéré à https://publications.polymtl.ca/2407/

Osher, S., & Sethian, J. A. (1988). Fronts Propagating with Dependent Speed: Algorithms Based on Hamilton-Jacobi Formulations. *Journal of Computational Physics*, *79*(1988), 12-49.

Owkes, M., & Desjardins, O. (2013). A discontinuous Galerkin conservative level set scheme for interface capturing in multiphase flows. *Journal of Computational Physics*, *249*, 275-302. https://doi.org/10.1016/j.jcp.2013.04.036

Ponziani, F. A., & Tinaburri, A. (2015). Water jet streams modeling for firefighting activities with the aid of CDF. Dans *Safety and Security Engineering VI* (Vol. 1, pp. 323-334). https://doi.org/10.2495/SAFE150281

Pourbagian, M., & Habashi, W. G. (2015). Aero-thermal optimization of in-flight electro-thermal ice protection systems in transient de-icing mode. *International Journal of Heat and Fluid Flow*, *54*, 167-182. https://doi.org/10.1016/j.ijheatfluidflow.2015.05.012

Prakash, C., & Voller, V. (1989). On the Numerical Solution of Continuum Mixture Model Equations Describing Binary Solid-Liquid Phase Change. *Numerical Heat Transfer, Part B: Fundamentals: An International Journal of Computation and Methodology*, *15*(2), 171-189. https://doi.org/10.1080/10407798908944899

Privatefly. (2017). Exonoration des frais de dégivrage pour un vol privé. privatefly. Repéré à https://www.privatefly.fr/location-jet-prive/degivrage-d-un-jet-prive

Reid, T., Baruzzi, G., Aliaga, C., Aubé, M., & Habashi, W. (2010). FENSAP-ICE: Application of Unsteady CHT to De-Icing Simulations on a Wing with Inter-Cycle Ice Formation. Dans *AIAA Atmospheric and Space Environments Conference* (pp. 1-11). Reston, Virigina : American Institute of Aeronautics and Astronautics. https://doi.org/10.2514/6.2010-7835

Reitz, R. D. (1978). *Atomization and other breakup regimes of a liquid jet*. Princeton, NJ: Princeton University. Repéré à https://uwmadison.app.box.com/s/38y5hz57xzzphkux7p4t

Rodríguez-Ocampo, P. E., Ring, M., Hernández-Fontes, J. V., Alcérreca-Huerta, J. C., Mendoza, E., & Silva, R. (2020). CFD simulations of multiphase flows: Interaction of miscible liquids with different temperatures. *Water (Switzerland)*, *12*(9). https://doi.org/10.3390/W12092581

Rusche, H. (2002). *Computational Fluid Dynamics of Dispersed Two-Phase Flows at High Phase Fractions*. Imperial College of Science, Technology & Medicine. Repéré à http://hdl.handle.net/10044/1/8110

S.Paquet, C., J.Lawrence, L., & C.R.Shelley, C. (2008). *Droit au but: Givrage au sol*. Ottawa : Direction de la Sécurité des vols. Repéré à http://publications.gc.ca/collections/collection_2008/forces/D12-14-2008F.pdf

SAE. (2021). Aircraft Ground Deicing/Anti-Icing Processes AS6285D. *AEROSPACE STANDARD*. https://doi.org/https://doi.org/10.4271/AS6285D

Saidi, M. S., Rismanian, M., Monjezi, M., Zendehbad, M., & Fatehiboroujeni, S. (2014). Comparison between Lagrangian and Eulerian approaches in predicting motion of micron-sized particles in laminar flows. *Atmospheric Environment*, *89*, 199-206. https://doi.org/10.1016/j.atmosenv.2014.01.069

Shinjo, J., & Umemura, A. (2010). Simulation of liquid jet primary breakup: Dynamics of ligament and droplet formation. *International Journal of Multiphase Flow*, *36*(7), 513-532. https://doi.org/10.1016/j.ijmultiphaseflow.2010.03.008

Sparrow, E. M., Patankar, S. V, & Ramadhyani, S. (1977). Analysis of Melting in the Presence of Natural Convection in the Melt Region. *Journal of Heat Transfer*, *99*(4), 520-526. https://doi.org/10.1115/1.3450736

Stanton, D. W., & Rutland, C. J. (1998). Multi-dimensional modeling of thin liquid films and spray-wall interactions resulting from impinging sprays. *International Journal of Heat and Mass Transfer*, *41*(20), 3037-3054. https://doi.org/10.1016/S0017-9310(98)00054-4

Stefan, J. (1891). Ueber die Theorie der Eisbildung, insbesondere über die Eisbildung im Polarmeere. *Annalen der Physik*, *278*(2), 269-286. https://doi.org/10.1002/andp.18912780206

Stevens, J. (1988). *Measurements of Local Heat Transfer Coefficients: Results for an Axisymmetric, Single-Phase Water Jet Impinging Normally on a Flat Plate with Uniform Heat Flux*. Master's thesis, Brigham Young University, Provo, Utah.

Stevens, J., & Webb, B. W. (1991). Local Heat Transfer Coefficients Under an Axisymmetric, Single-Phase Liquid Jet. *Journal of Heat Transfer*, *113*(1), 71. https://doi.org/10.1115/1.2910554

Stiesch, G. (2003). *Modeling Engine Spray and Combustion Processes*. *Springer-Verlag Berlin Heidelberg* (Vol. 42). Berlin, Heidelberg : Springer Berlin Heidelberg. https://doi.org/10.1007/978-3-662-08790-9

Subramaniam, S. (2013). Lagrangian–Eulerian methods for multiphase flows. *Progress in Energy and Combustion Science*, *39*(2-3), 215-245. https://doi.org/10.1016/j.pecs.2012.10.003

Sussman, M., & Puckett, E. G. (2000). A Coupled Level Set and Volume-of-Fluid Method for Computing 3D and Axisymmetric Incompressible Two-Phase Flows. *Journal of Computational Physics*, *162*(2), 301-337. https://doi.org/10.1006/jcph.2000.6537

Tan, Z., Lim, K. M., & Khoo, B. C. (2007). An adaptive mesh redistribution method for the incompressible mixture flows using phase-field model. *Journal of Computational Physics*, *225*(1), 1137-1158. https://doi.org/10.1016/j.jcp.2007.01.019

Task Force Tips, I. (2010). *Ice-Control Anti-Icing & Deicing Nozzles*. Valparaiso, IN, USA : Task Force Tips, Inc. Repéré à https://manualzz.com/download/8207244

Thomas, S. K., Cassoni, R. P., & MacArthur, C. D. (1996). Aircraft anti-icing and de-icing techniques and modeling. *Journal of Aircraft*, *33*(5), 841-854. https://doi.org/10.2514/3.47027

Tong, A. Y. (2003). A Numerical Study on The Hydrodynamics and Heat Transfer of a Circular Liquid Jet Impinging Onto a Substrate. *Numerical Heat Transfer, Part A: Applications*, *44*(1), 1-19. https://doi.org/10.1080/713838171

Transport Canada. (2005). *Guidelines for Aircraft Ground Icing Operations (Chapter 13)*. Ottawa. Repéré à http://www.tc.gc.ca/publications/en/tp14052/pdf/hr/tp14052e.pdf

United states Environmental protection Agency. (2012). *Technical Development Document for the Final Effluent Limitations Guidelines and New Source Performance Standards for the Airport Deicing Category*. Washington, DC.

Velraj, R., Seeniraj, R. V, Hafner, B., Faber, C., & Schwarzer, K. (1999). Heat transfer enhancement in a latent heat storage system. *Solar Energy*, *65*(3), 171-180. https://doi.org/10.1016/S0038-092X(98)00128-5

Visaria, M., & Mudawar, I. (2008). Theoretical and experimental study of the effects of spray inclination on two-phase spray cooling and critical heat flux. *International Journal of Heat and Mass Transfer*, *51*(9-10), 2398-2410. https://doi.org/10.1016/j.ijheatmasstransfer.2007.08.010

Voller, V. R., & Prakash, C. (1987). A fixed grid numerical modelling methodology for convection-diffusion mushy region phase-change problems. *International Journal of Heat and Mass Transfer*, *30*(8), 1709-1719. https://doi.org/10.1016/0017-9310(87)90317-6

Wang, Yaqing, Liu, M., Liu, D., Xu, K., & Chen, Y. (2010). Experimental study on the effects of spray inclination on water spray cooling performance in non-boiling regime. *Experimental Thermal and Fluid Science*, *34*(7), 933-942. https://doi.org/10.1016/j.expthermflusci.2010.02.010

Wang, Yue, Ge, H.-W., & Reitz, R. D. (2010). Validation of Mesh- and Timestep-Independent Spray Models for Multi-Dimensional Engine CFD Simulation. *SAE International Journal of Fuels and Lubricants*, *3*(1), 277-302. https://doi.org/10.4271/2010-01-0626

Webb, B. W., & Ma, C. F. (1995). Single-Phase Liquid Jet Impingement Heat Transfer. Dans J. P. Hartnett (Éd.), *Advances in Heat Transfer* (1re éd., Vol. 26, pp. 105-217). United States : Elsevier Science Publishing Co Inc. https://doi.org/10.1016/S0065-2717(08)70296-X

Wong, J., Papadakis, M., & Wong, J. (2013). CFD Analysis of a Wing with a Bleed Air Ice Protection System. Dans *5th AIAA Atmospheric and Space Environments Conference* (pp. 1-26). Reston, Virginia : American Institute of Aeronautics and Astronautics. https://doi.org/10.2514/6.2013-2935

Xu, Z., Han, Z., & Qu, H. (2020). Comparison between Lagrangian and Eulerian approaches for prediction of particle deposition in turbulent flows. *Powder Technology*, *360*, 141-150. https://doi.org/10.1016/j.powtec.2019.09.084

Yakhya, S., Ernez, S., & Morency, F. (2019). Computational Fluid Dynamics Investigation of Transient Effects of Aircraft Ground Deicing Jets. *Journal of Thermophysics and Heat Transfer*, *33*(1), 117-127. https://doi.org/10.2514/1.T5428

Yakhya, S., & Morency, F. (2017). Numerical Study of Momentum and Heat Transfer in Propylene Glycol Jets used for Aircraft Ground Deicing. *23rd AIAA Computational Fluid Dynamics Conference*, (June), 1-20. https://doi.org/10.2514/6.2017-4504

Yan, Z. B., Duan, F., Wong, T. N., Toh, K. C., Choo, K. F., Chan, P. K., … Lee, L. W. (2013). Large area impingement spray cooling from multiple normal and inclined spray nozzles. *Heat and Mass Transfer*, *49*(7), 985-990. https://doi.org/10.1007/s00231-013-1131-1

Yoon, S. S., Hewson, J. C., Desjardin, P. E., Glaze, D. J., Black, A. R., & Skaggs, R. R. (2004). Numerical modeling and experimental measurements of a high speed solid-cone water spray for use in fire suppression applications. *International Journal of Multiphase*

Flow, *30*(11), 1369-1388. https://doi.org/10.1016/j.ijmultiphaseflow.2004.07.006

Zeneli, M., Nikolopoulos, A., Karellas, S., & Nikolopoulos, N. (2021). Numerical methods for solid-liquid phase-change problems. Dans *Ultra-High Temperature Thermal Energy Storage, Transfer and Conversion* (pp. 165-199). Cambridge : Elsevier. https://doi.org/10.1016/B978-0-12-819955-8.00007-7

Zhang, Z., & Chen, Q. (2007). Comparison of the Eulerian and Lagrangian methods for predicting particle transport in enclosed spaces. *Atmospheric Environment*, *41*(25), 5236-5248. https://doi.org/10.1016/j.atmosenv.2006.05.086

Zhao, L., Torelli, R., Zhu, X., Naber, J., Lee, S.-Y., Som, S., … Raessi, M. (2018). Evaluation of Diesel Spray-Wall Interaction and Morphology around Impingement Location. Dans *SAE Technical Paper Series*. https://doi.org/10.4271/2018-01-0276

Zhao, L., Torelli, R., Zhu, X., Scarcelli, R., Som, S., Schmidt, H., … Lee, S.-Y. (2017). An Experimental and Numerical Study of Diesel Spray Impingement on a Flat Plate. *SAE International Journal of Fuels and Lubricants*, *10*, 16. https://doi.org/10.4271/2017-01-0854